UNIVERSITÀ DEGLI STUDI DI PADOVA

DIPARTIMENTO DI INGEGNERIA CIVILE, EDILE E AMBIENTALE

Department of Civil, Environmental and Architectural Engineering

Corso di Laurea Magistrale in Environmental Engineering

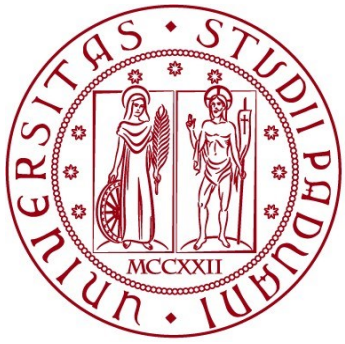

MASTER THESIS

APPLICATION OF HYDRUS-3D TO MODEL MOISTURE CONTENTAND CAPILLARY PRESSURE AT FIVE MONITORING SITES IN THE VENICE-FARMLAND

Supervisor:
Prof. PIETRO TEATINI

Co-Supervisor:
ESTER ZANCANARO

Student: TITASH SINHA
2014425

ACADEMIC YEAR 2023-2024

INDEX

INDEX OF FIGURES

1. ABSTRACT

The accurate simulation of soil moisture content and capillary pressure can have significant implications for decision-making in various fields. For example, in agriculture, it can help in determining the appropriate irrigation scheduling, which can improve crop yield and water use efficiency. In hydrology, it can aid in predicting groundwater recharge and aquifer storage, while in environmental engineering, it can assist in assessing the impact of land use and land management practices on soil moisture content and capillary pressure.

This study assesses the performance of the HYDRUS-3D computer model in simulating soil-moisture content and capillary pressure in an experimental field located within the southern part of Venice Lagoon under different field condition. The model was calibrated and validated using field data from five monitoring locations over a period of five months from June to October in the year 2021. Soil moisture content and matric potential at different depths were measured using soil sensors connected to datalogger for continuous monitoring. The experimental site was also characterized for soil properties such as soil texture and hydraulic properties. The results suggest that the laboratory methods used to measure soil moisture and classify soil texture can provide reliable data for validating and calibrating computer models. The integration of field data and computer models can lead to a better understanding of the soil-water-plant-atmosphere system, which is essential for sustainable land management practices. However, further research is needed to determine the model's accuracy in different field conditions, soil types, and land management practices. Also, more extensively field data collection can provide a better understanding of the spatial and temporal variability of soil moisture content and capillary pressure, which can improve model performance.

The study concludes that the HYDRUS 3D computer model can be used to simulate soil moisture content and capillary pressure under different field conditions in the Venice farmland. The model accurately predicts the soil moisture content at different depths, which can be useful in managing irrigation, groundwater recharge, and other agricultural practices. The result of this study can be used to further refine the model parameters and improve the accuracy of soil moisture predictions for effective agricultural management and groundwater recharge.

2. INTRODUCTION

Water resource management has become a crucial worldwide, due to climate change, rising global population and increasing demand for water in various sectors, such as agriculture, industry, and urban water supply. As a result, accurate modelling tools are necessary to predict the behaviour of water and solutes in soil systems, which is vital for effective water resource management. HYDRUS-3D is a model that has gained widespread in hydrological and environmental research. The software can simulate waterflow, solute transport, and heat transfer in variably saturated porous media. HYDRUS-3D ability to model complex 3D geometries and incorporate detailed soil properties and boundary conditions makes it a powerful tool to investigate a wide range of hydrological problems.

This master thesis aims to investigate the practical application of HYDRUS 3D in modelling the soil moisture content and capillary pressure in a farmland located at the southern margin of the Venice Lagoon. In 2021 a freshwater recharge test was performed where all the sensors were placed and measurement was done, the installation of drains were done to inject fresh water into agricultural land, (Tossi et al., 2021). The study objective is to evaluate the effectiveness of HYDRUS 3D in modelling the soil moisture content and capillary pressure under different scenarios and soil properties in which the following VGM parameters were optimized θr , $\propto$, n and Ks. Also, to explore some agreement and discrepancies between the observed and simulated data points, whether it exhibit similar trends and patterns or else it fails to mimic the observed data. All the information related to soil properties such as the textural class, textural distribution and bulk densities was initially provided for four different depth intervals (0-20 cm), (20-40 cm), (40-60 cm), (60-80 cm) respectively. The prediction of VGM parameters was performed by using (Rosetta, 2001).

In this thesis the methodology is elaborated in the fifth section with all the possible steps for the numerical simulation indicating almost four months (8^{th} June to 28^{th} October) of meteorological data and finally in the result comparison of two dataset (observed and simulated data) as well as temporal behaviour were analyzed which made easy to predict the software's compatibility.

3. SITE DESCRIPTION

The experimental site, is a 21-ha agricultural field located at Ca'Bianca, (Chioggia9, North-East of Italy (45 10'57'' N, 12 13'55'' E,UTM, WGS84) along the southern margin of the Venice Lagoon. The hydrogeological characteristics of the soil were already characterised by (Teatini et al., 2022), which makes possible to take advantage of considerable amount of existing data. The study area is bounded by the Venice Lagoon, Morto Channel, Brenta, and Bacchiglione rivers. In the past, the area was occupied by swamps until it was reclaimed for the agricultural purposes between the years of 1892 and 1967. The land is entirely flat and lies below the mean sea level (msl), with the elevation ranging from -1m to -3.3m msl. The groundwater level is maintained at a suitable depth for agricultural practices by the "Casetta" pumping station a lot of open channels and ditches the depth of the groundwater table, is maintained at a shallower depth during summer to promote sub-irrigation and ranges from 0.5 to 1.8m below the soil surface, with small vertical fluctuation during the year. The site is affected by seawater intrusion. Saltwater contamination possesses a critical issue in this region, primarily due to its low elevation, almost at -2.5m above sea level and the occurrence of subsidence phenomena resulting from the oxidation of surface organic soils. Additionally, during periods of drought, the dispersion of tidal water from the riverbeds of the Brenta and Bacchiglione rivers exacerbates subsurface salt contamination. These rivers act as a barrier between the Venice Lagoon and the study area and have previously experienced the intrusion of seawater, with its influence extending up to 20km from the river estuary.

The soil is heterogeneous, mainly silty and clay (UNESCO, n.d.), with acidic peat deposits formed from the reedbeds and swamps in place before the reclamation and sandy drifts derived from past fluvial ridges and coastal strips. The dataset used in the present test was collected during the year 2011. The field was cultivated with rainfed maize (seeding 25th March and harvesting 10th September). Soil tillage was an autumn ploughing to the 0.3m depth, followed by standard seedbed preparation operations.

The study area is characterized by the presence of numerous deep aquifers that can reach up to 100 m in depth. However, within the first 20-30 m, the soil is highly different due to the presence of different geological deposits such as alluvial, lagoonal, littoral and deltaic sediments. Phreatic, semi-confined, and locally confined aquifers are also present, as reported ([Rizzetto et al., Teatini et al., & Scudiero et al., 2012). Despite being relatively far from the

sea, agricultural production is impacted by the salinity of the groundwater which is located close to the surface level. This is due to the intrusion of a salt plume that extends up to 10-15 km inland and 100 meters deep in the southern region, as stated by (Elia Scudiero et al., 2014). Moreover, the land level in the area is approximately three meters below the mean sea level which effectively favours the salinisation process ([Teatini et al., 2009)

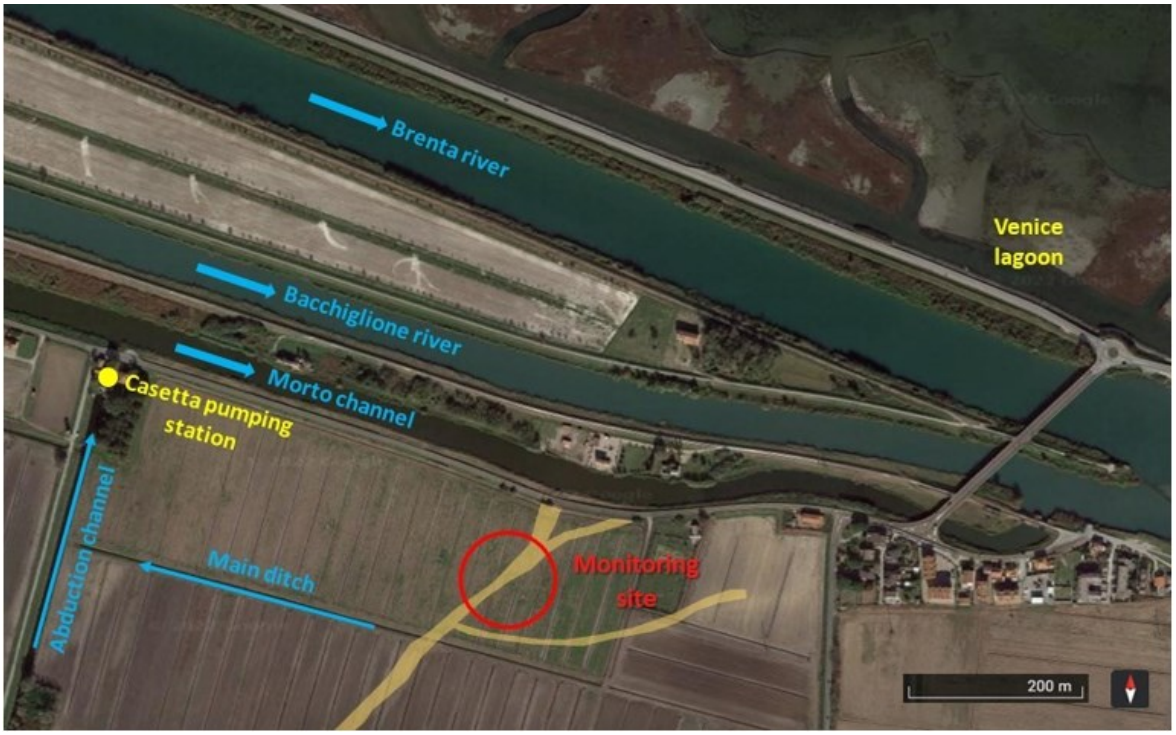

Figure 3.1: Satellite view of the site with paleo channels, the main watercourses, ditches, and the pumping station location.

The impact of this occurrence can be observed directly on the current crops, displaying uneven yields distributed in a sporadic manner throughout the location. Evidence from the satellite images highlights how these zones tend to be arranged in one-dimensional shapes of variable width, indicating a correlation with the existence of older river channels that consists of high percentage of sand.

Through a comparison of information obtained from electrical tomography matched with historical maps and images from satellites, it was proven that the theory of prior river valleys, are characterized according to the flood sequence. As time progressed, the carried solids within the waterway caused the sedimentation of various substances at the base, forming a complex stratified structure that becomes more challenging to distinguish and analyse as the layers get thinner. The existence of sandy soil in the older channels increases the

permeability, creating channels for groundwater movement that can be either fresh or saline in this circumstance. ([Teatini et al., 2009)

The main paleo channel that runs from southwest to northeast across the field was chosen for the installation of a recharge drain, to inject fresh water into the soil and reduce the saltwater contamination. The drain was placed 1.5 meters deep and is supplied with the fresh water from the Morto channel, which is characterized by a higher water level than the phreatic surface and therefore does not require pumps to maintain water flow.

The drainage system is made of a 160 mm outer diameter and 120 mm inner diameter polyethylene pipe that spans 220 meter in length. It was covered with a geotextile during installation to prevent blockage from surrounding soil. The main objective is to take advantage of the permeability of the paleo-channel to amplify the benefits of the recharge drain in a larger area.

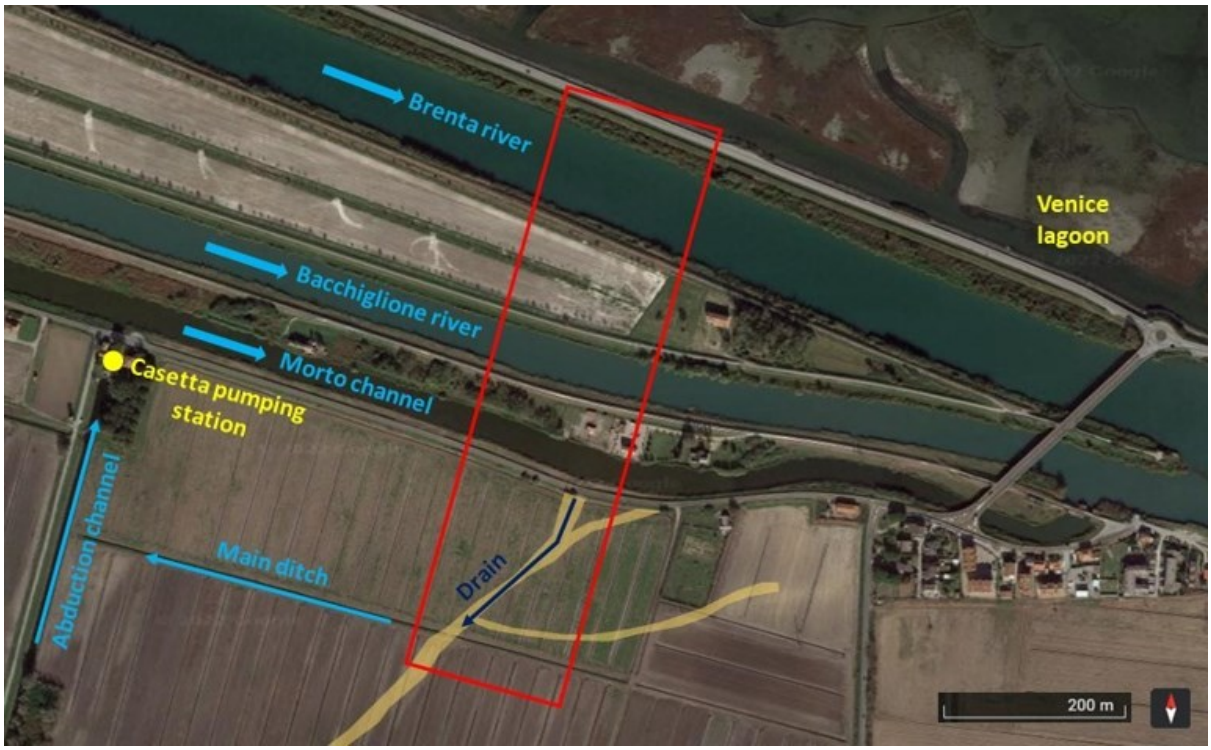

Figure 3.2: The domain of the study area with the recharge drain (line in blue) along the main paleochannel (in yellow).

4. DATASET

There were several measurements that were conducted in the study area for the characterization of the morphology, the surface water bodies, the stratigraphy, soil properties and the underground hydrology.

4.1 Surface water bodies

Several studies were conducted to stablish the lowest and highest point of the specific water bodies of interest, in addition monitoring of the groundwater levels were used to develop Figure4.1 that showcases the findings of the CORILA research team's study titled "Flows of groundwater in the Venetian lagoon system" (2003-2006). The information gathered relates to the minimum and maximum levels recorded in the surface water bodies and the monitored piezometers located within a north-south sector at the boundary of the lagoon.

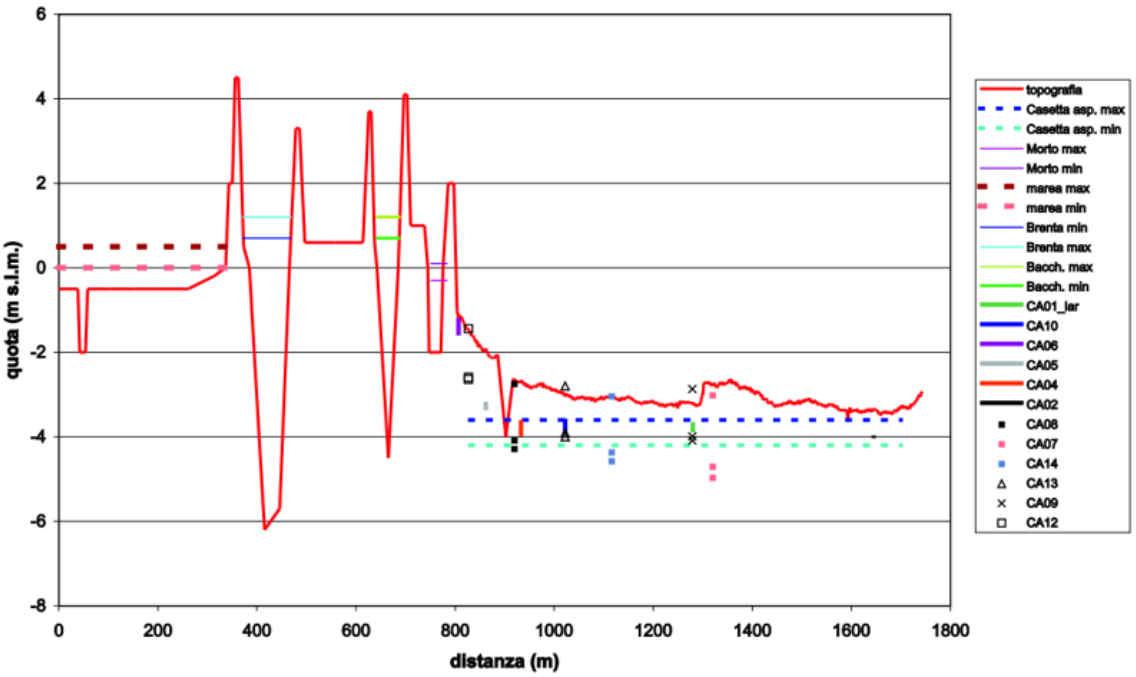

Figure 4.1: Maximum and minimum values of levels recorded on the surface water bodies and piezometers at Casetta pumping station.

On average the water table level is around -3.8 m below msl and 1-1.5 m below ground level with fluctuations determined by the season and the Casetta pumping station. To drain precipitation water, the level is lowered in winter, while it is raised in summer to aid crop growth through capillary rise.

Seasonal conditions can also affect water level oscillations in the Bacchiglione and the Brenta rivers, which play a primary role in the occurrence of saltwater intrusion (Cunico, 2019). Meanwhile, the Morto channel has displayed a constant water level at around 0 m above a.s.l. with minimal fluctuations.

4.2 Morphology and stratigraphy

The upper 20 m of subsoil consists of a sequence of alluvial, transitional, and marine late Pleistocene and Holocene deposits. The final layer is a palaeosol called caranto, (Mozzi et al., 2003). The top of this layer represents an erosional surface that is a regional unconformity marking the boundary between Pleistocene and Holocene deposits [(Zecchin et al., 2009)].

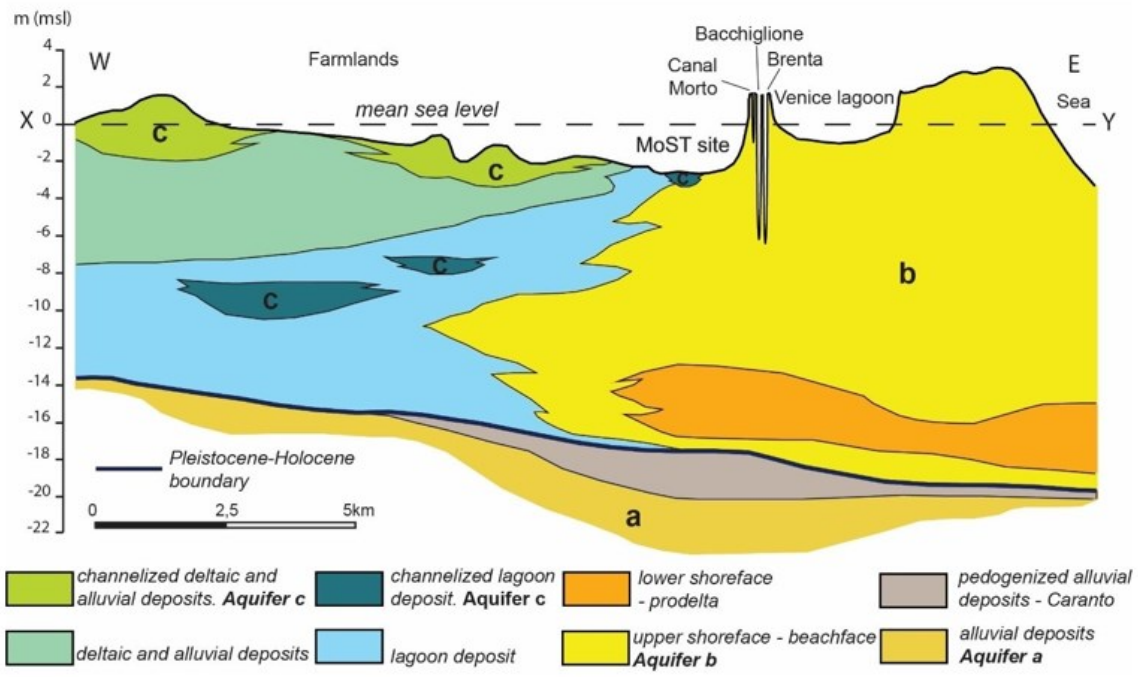

Figure 4.2 :Stratigraphic description of the study area.

The area under investigation is a coastal plain with low elevation, consisting mainly of farmlands. These lands were created through the process of clamming swamps and lagoons using hydraulic methods at the beginning of the last century. Due to the ancient land morphology, combined with high land subsidence rates [(Rizzetto et al., Gambolati et al., Carbogin et al., & Tosi et al.)], the farms are mostly situated below the mean sea level, down to 4m.

Given the context of the region which comprises of littoral, deltaic, lagoon and alluvial deposits, a complex hydrogeological system has developed that consists of confined, semi-confined, and unconfined aquifers. The confined aquifers can be found in the Pleistocene alluvial deposit and is bounded by the Caranto paleosol. The unconfined and locally confined aquifers are located in Holocene sandy deposits. The upper aquifers can be found in small sandy lenses nested in channelized morpho-sedimentary bodies, resulting from the inheritance of lagoon and fluvio-deltaic channels or remnants of littoral ridges.

All varieties of aquifers can be found in the research area, and there is a layering of local aquifers on the top of the nearby shoreline aquifer according to [(Cavallina et al., 2022)]. Detailed knowledge of the underground stratigraphy has been obtained through the recent drilling of numerous boreholes. Four of these boreholes were previously drilled by UNIPD (S1, S2, S3 and S5), and soil samples from these have been analyzed alongside samples from five newly drilled boreholes (Most1, MoST2, MoST3, MoST4 and MoST5)

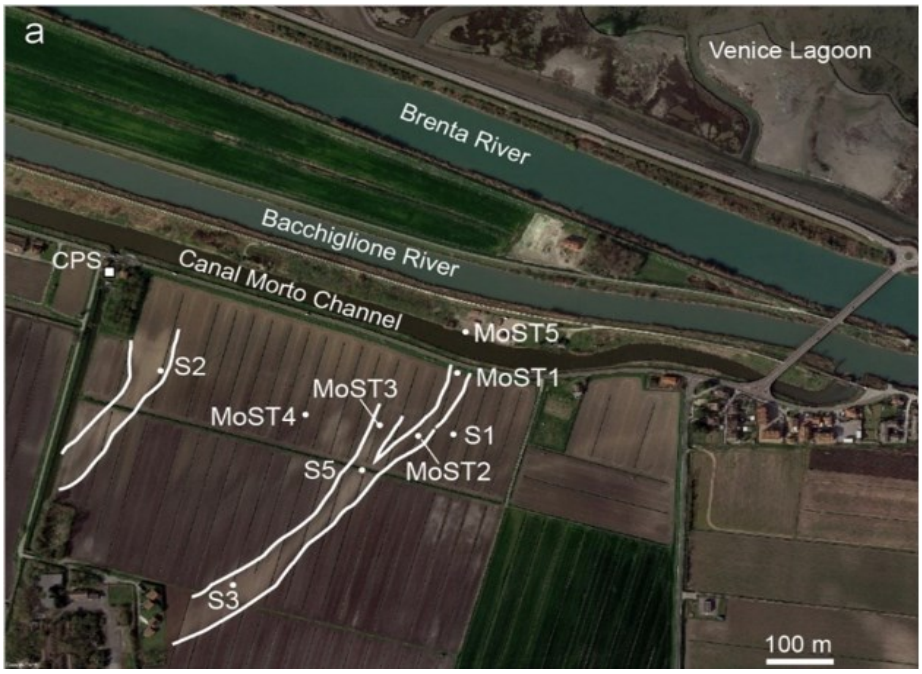

Figure 4.3: Position of piezometric wells and cores (S1, S2, S3, S5, MoST1, MoST2, MoST3, Most4, MoST5)

Drilled by sedimentological analyses enable the identification of the traits of the subterranean soil. The soil is categorized into seven hydrostratigraphic units (HU) and described below, beginning from the base as depicted in the Figure 4.4 [(Cavallina et al., 2022)]:

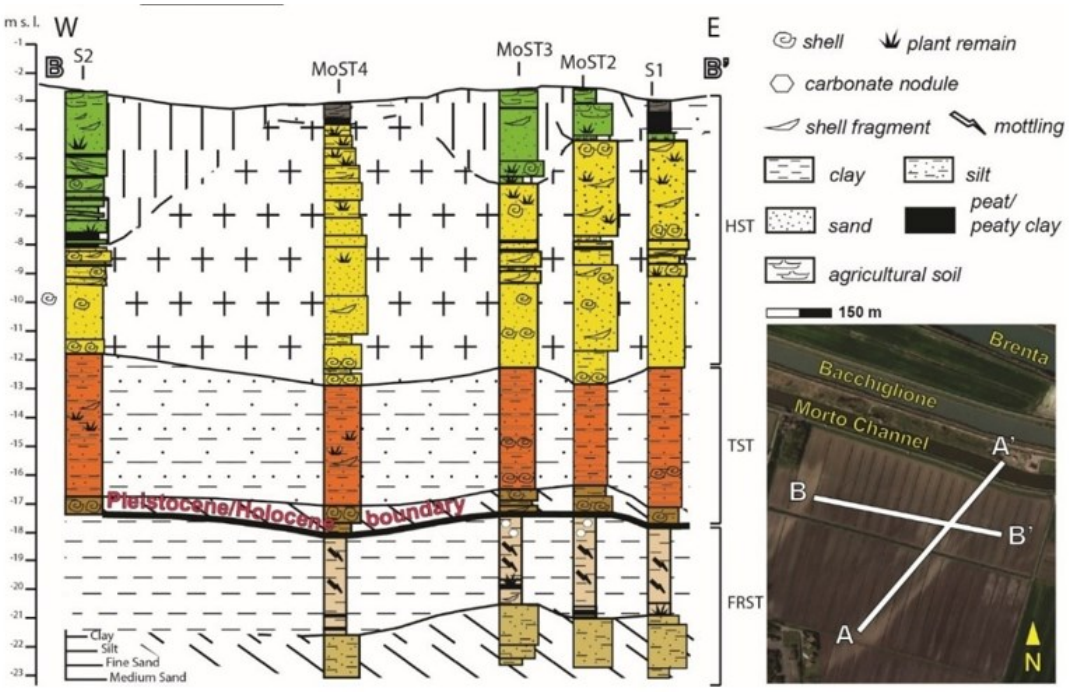

Figure 4.4: Hydrostratigraphic sections of the study area

- HU1: A restricted underground water source measuring approximately 3-4 m thick made up of brown-greyish sandy silt to sand with layers of silty clay and clayey silt, which is moderately sorted [(Tosi et al. & Fabbri et al.)].
- HU2: An impermeable underground layer measuring 3-4 meters thick composed of light brown clay to silent clay layers. It has a bioturbated erosional surface at the top and dark brown spread organic matter at the bottom.
- HU3: A narrow section of the underground water table measuring approximately 1 meter thick composed of grey silt to silty sand deposit, without any distinct structure and poorly sorted.
- HU4: An aquitard, 3.5-5 meters thick with medium to low permeability composed of grey silt and sandy silt sediments.
- HU5: The main phreatic aquifer in the area, 8-10 m thick, primarily made up of permeable sandy deposits.
- HU6: A local and relatively thin aquifer, 0.5-5 m thick, containing moderately sorted medium to fine sand in sand bodies, alternating with sub-horizontal layers of sandy, silty clay and clayey silt.
- HU7: Discontinuous deposits of the topsoil layer located beneath the arable land and with a maximum thickness of 4 meters. It contains peat, peaty clay or clay layers, and is prone to geochemical land subsidence due to oxidation of the organic matter in the soil. It is considered an impervious layer due to its low permeability.

4.3 Subsurface hydrology

To investigate the properties of groundwater in areas affected by palaeoalvements and nearby regions, monitoring stations with appropriate equipment were set up. The positioning of these stations with appropriate equipment is explained in the next paragraph.

With reference to Figure4.5 one monitoring stations S5 station was established a few tens of meters to the east of the easternmost branch of the paleochannel. Inside the paleochannel, three stations S1, S2, and S3were installed at varying distances from the Morto channel,

while a last one was placed outside to the west (S4). This pattern formed a cross-shape structure and enabled a better understanding of the movements of groundwater. Recently in 2021, six additional piezometers were added at distances of 5, 10 and 20 meters from station S2, situated near the drain on both sides, Figure (4.5).

Figure 4.5: Monitoring stations and piezometers position.

At all the five stations, there were equipped by:

- four sensors of water content, temperature, and electrical conductivity (TEROS 12, METER Group) were installed at depths of 10, 30, 50 and 70 cm respectively.
- two tensiometers at depth of 30 cm and 50 cm (T4e, METER Group)
- one piezometer with a depth of 2 m was also included.

In 2020, S2 and S4 were equipped by two additional tensiometers installed at a depth of 70 cm. In 2021, all stations had the same setup with two tensiometers at a depth of 70 cm.

The the instrumentation was installed on June 8th and data was recorded daily until October 28th, 2021.Graphs of water content and matric potential measured at a depth of 30 cm were collected from all the station (Figures 4.6 and 4.7, respectively).

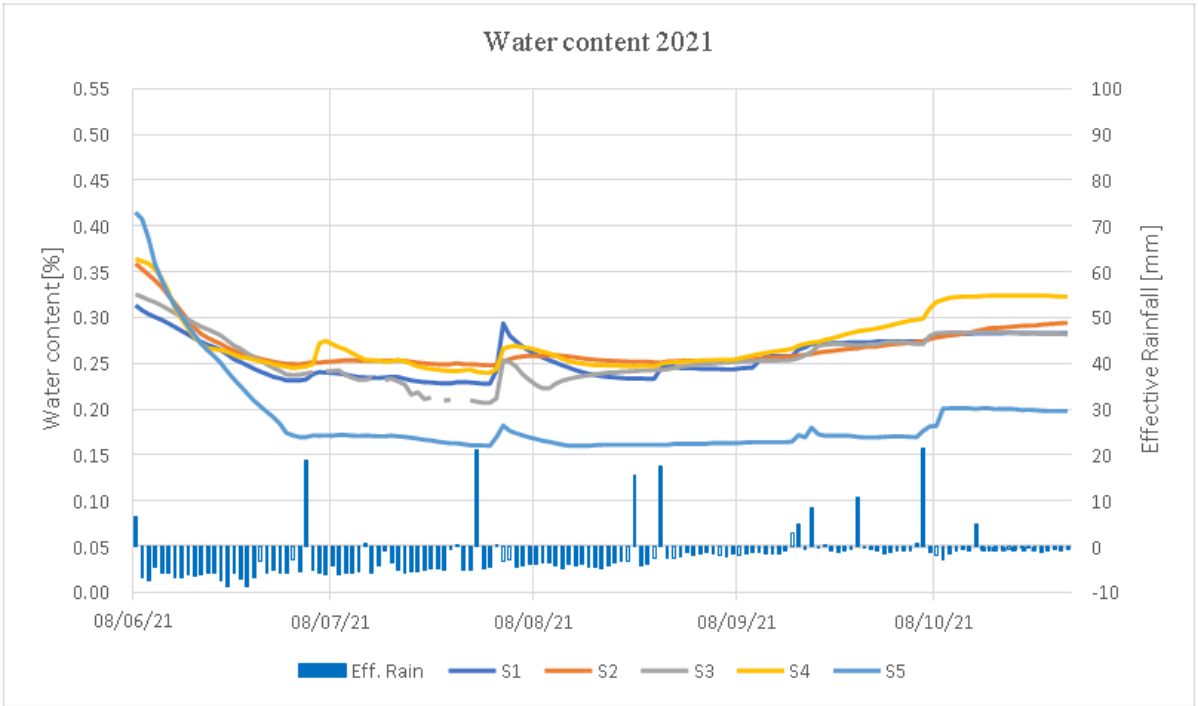

Figure 4.6: Moisture content at a depth of 30cm measured in the five monitoring stations and effective rainfall.

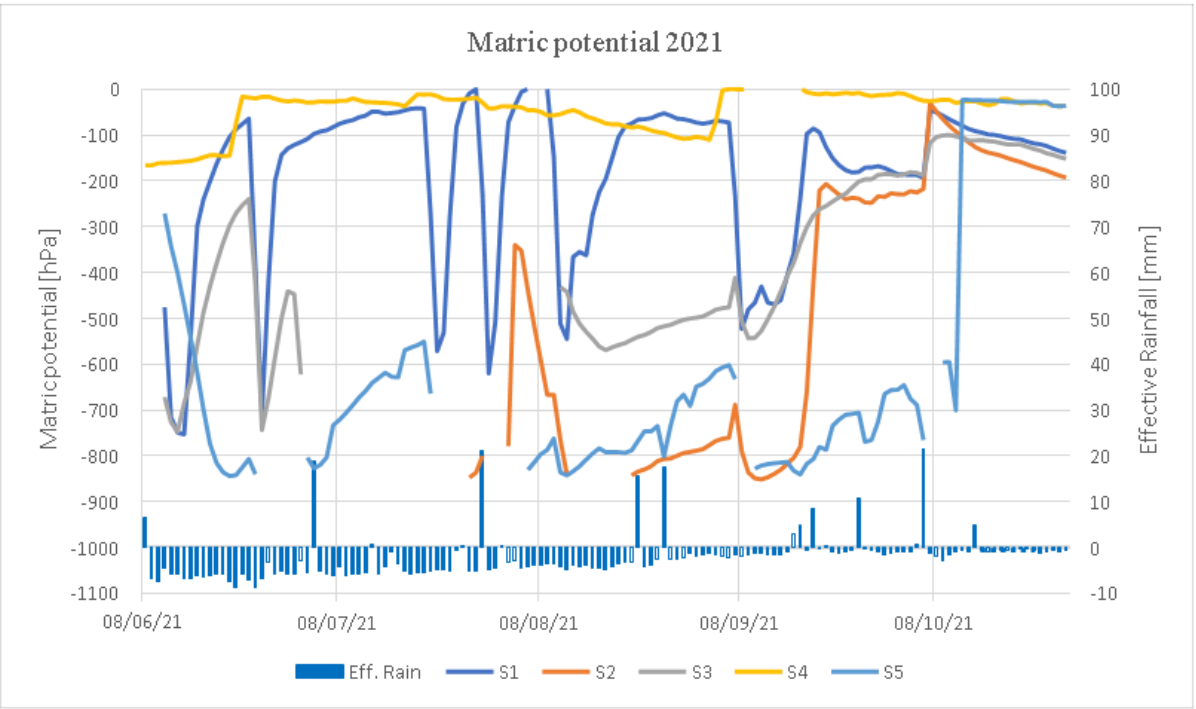

Figure 4.7: Matric potential at a depth of 30 cm measured in the five monitoring stations and effective rainfall.

The measurements of groundwater level were performed by the piezometers in all the stations weekly during the observation periods.

Basically, during the year 2021 the groundwater level was likely to have a similar trend in the various stations as shown in Figure 4.8. The difference between the various sensors mainly reflects the different elevation of the farmland surface at the monitoring stations.

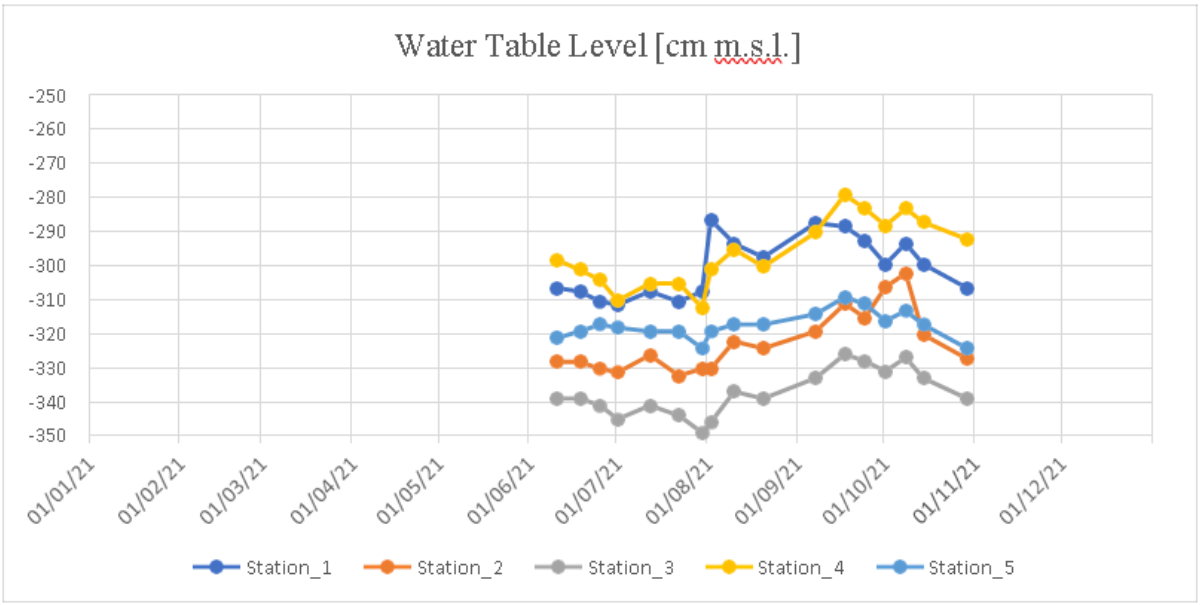

Figure 4.8: Measured water table level for the year 2021

4.4 Soil properties

Researchers investigated soil features by using on-site evaluations and experiments conducted in the laboratory. The Van Genuchten parameters, such as residual (θr) and saturated (θs) moisture content, empirical parameters (α and n), and the saturated hydraulic conductivity (Ks), were used to describe flow in the vadose zone. Table4.1 provides, various parameters obtained from laboratory experiments on a set of the samples gathered from five station are listed.

Station	**Soil depth cm**	**Ks cm/day 2021**	**θr 2021**	**θs 2021**	**alpha 1/cm 2021**	**n 2021**
1	0-20	99.98	0.064	0.4619	0.0041	1.7340
1	20-40	70.62	0.064	0.4518	0.0048	1.6867
1	40-60	219.24	0.047	0.4876	0.0112	1.4787
1	60-80	39.95	0.046	0.397	0.0142	1.4851
2	0-20	29.41	0.0626	0.4163	0.0052	1.6712
2	20-40	42.96	0.0584	0.4218	0.0056	1.6496
2	40-60	108.28	0.0444	0.3879	0.03879	1.7432
2	60-80	108.28	0.0444	0.3879	0.0382	1.7432
3	0-20	72.75	0.0647	0.4553	0.0048	1.6821
3	20-40	90.32	0.0624	0.4605	0.0051	1.6638
3	40-60	47.92	0.0408	0.379	0.0332	1.4645
3	60-80	332.12	0.0487	0.4328	0.038	2.1096
4	0-20	52.57	0.0726	0.4642	0.0048	1.6823
4	20-40	52.17	0.0713	0.4598	0.0047	1.6919
4	40-60	510.02	0.0664	0.6658	0.0098	1.4754
4	60-80	112	0.0543	0.4682	0.0089	1.5331
5	0-20	109.91	0.0705	0.4877	0.0047	1.6869
5	20-40	172.84	0.0703	0.5095	0.0046	1.6849
5	40-60	319.83	0.0559	0.6852	0.0289	1.3357
5	60-80	280.27	0.0564	0.6889	0.0317	1.3297

Table 4.1 Soil properties obtained from laboratory tests.

The values reported in the table above were obtained using (Rosetta, 2001) PTFs to (A Closed-form Equation for Predicting the Hydraulic Conductivity of Unsaturated Soils1, 1980) water retention parameters and saturated hydraulic conductivity by using textural class, textural distribution, bulk density and one or two water retention points as input.

The VanGmodel's were stored in an excel file in which the water content at each matric potential was graphically represented for each station and the four depth intervals: 0 – 20cm, 20 - 40 cm, 40 – 60 cm, and 60 – 80 cm (Figures 4.9 – 4.13)

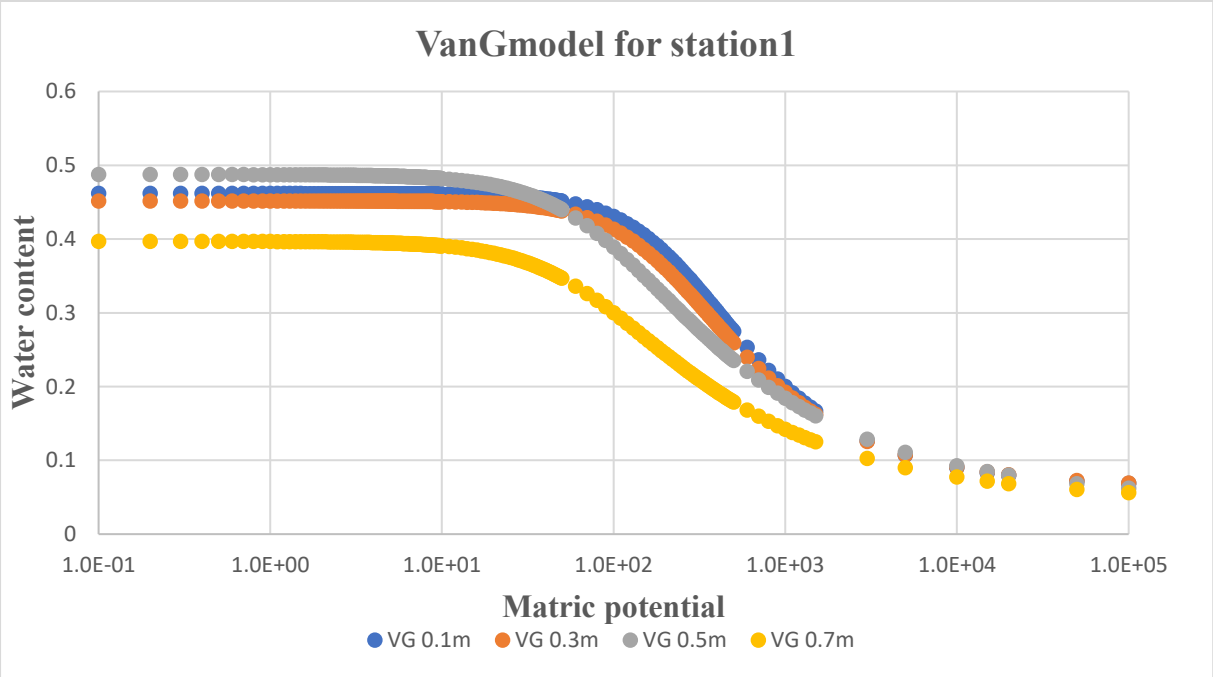

Figure 4.9: VanGmodel for station S*1 at a depth of 0.1 m*,0.3 m,0.5 m and 0.7 m respectively.

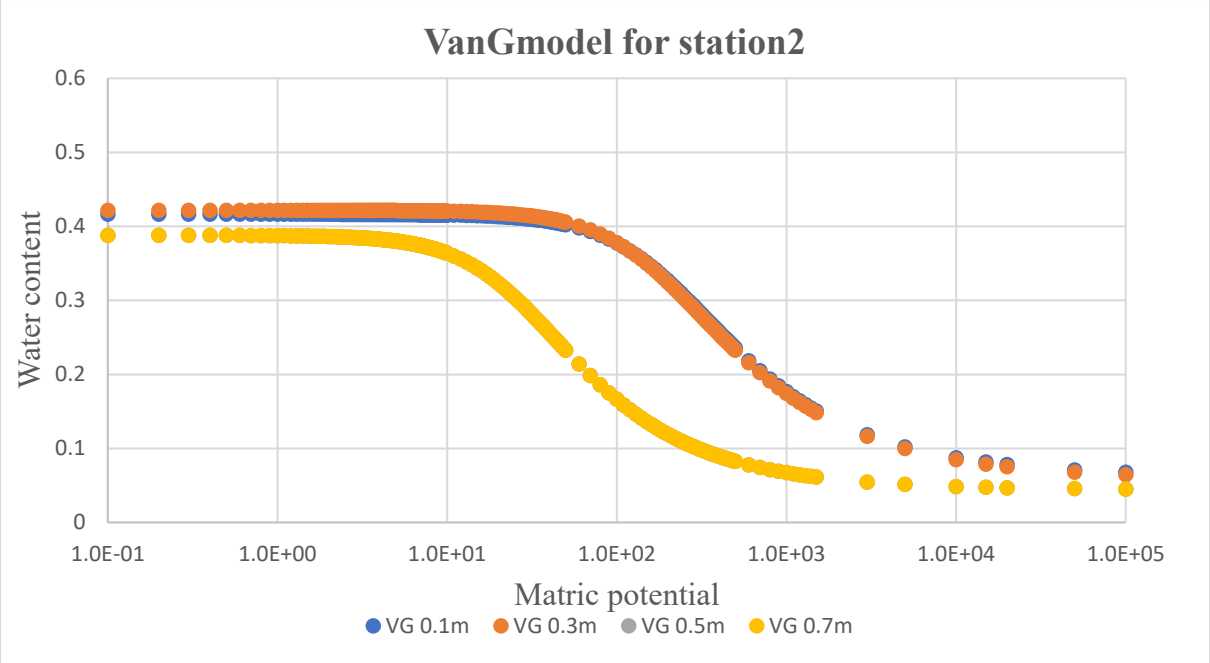

Figure 4.10: VanGmodel for station S2 *at a depth of 0.1 m*,0.3 m,0.5 m and 0.7 m respectively.

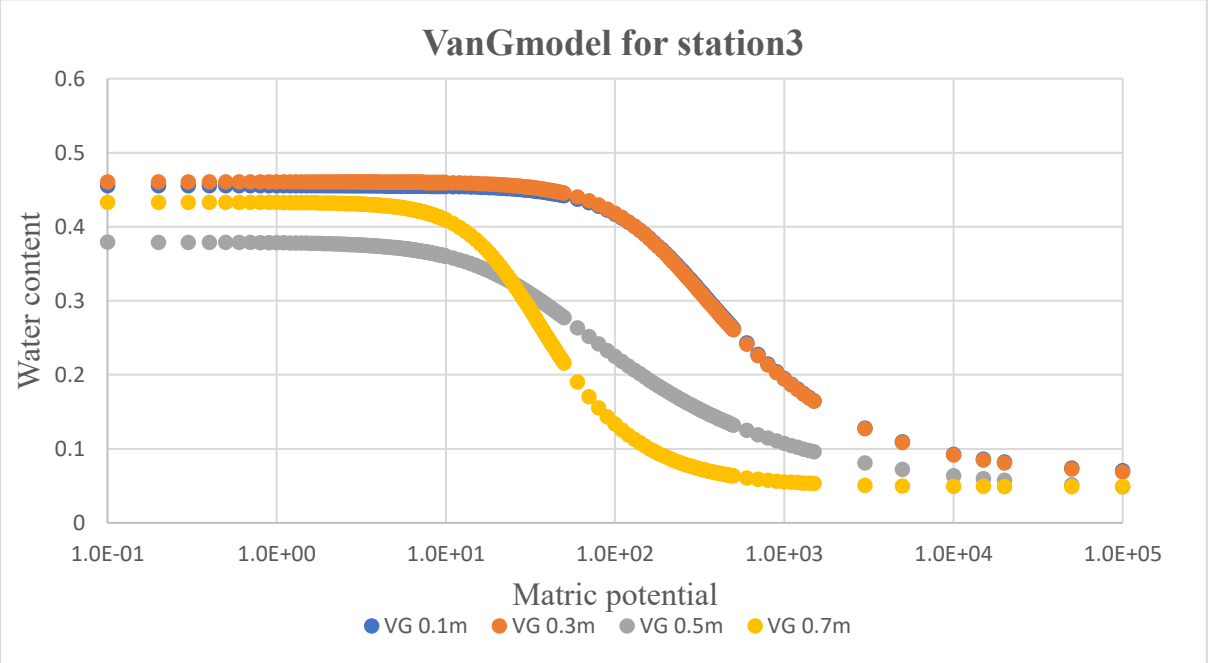

*Figure 4.11: VanGmodel for statio*n3 *at a depth of 0.1m*,0.3m,0.5m and 0.7m respectively.

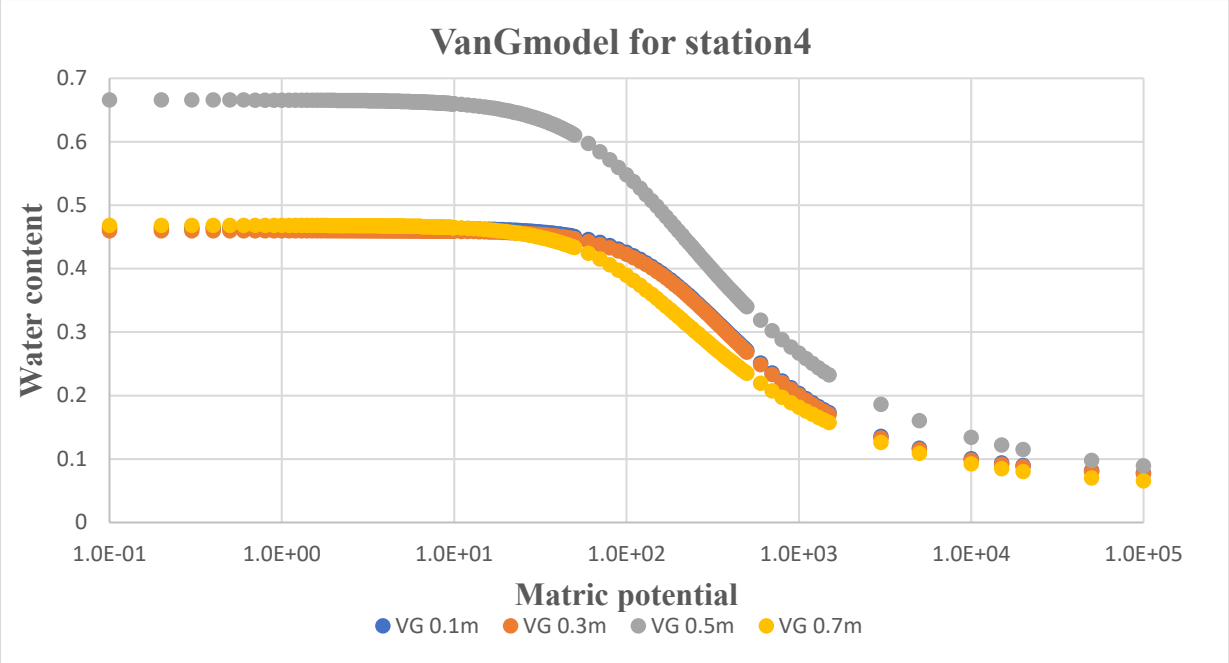

*Figure 4.12: VanGmodel for station*4 *at a depth of 0.1m*,0.3m,0.5m and 0.7m respectively.

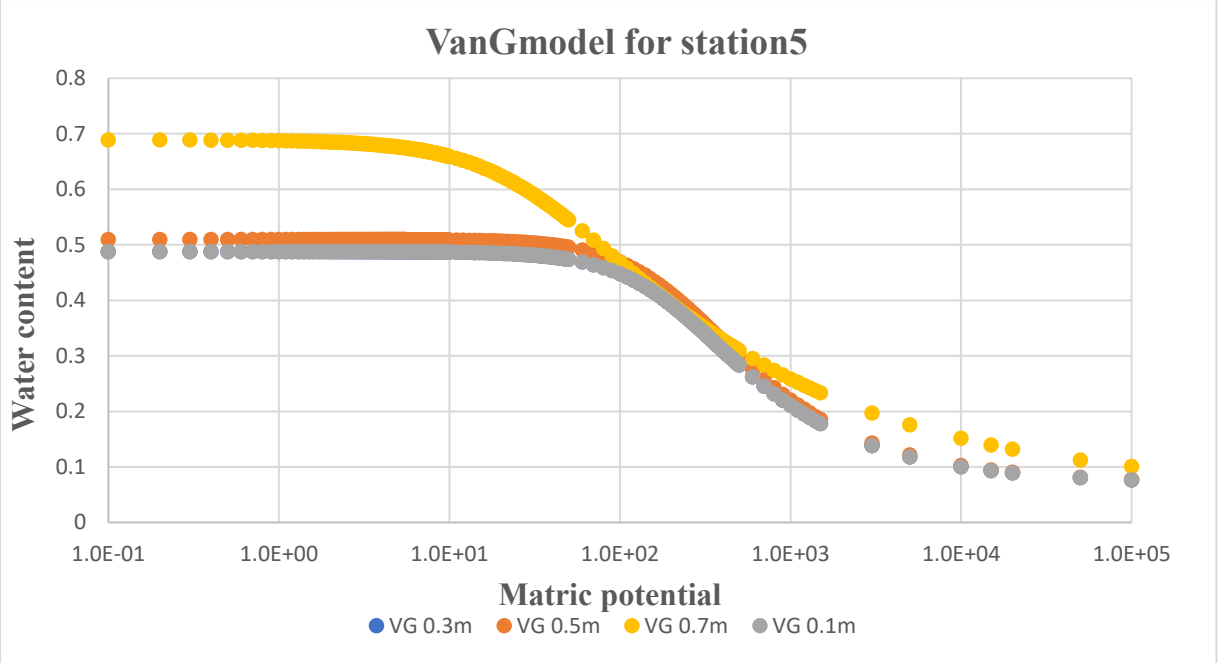

*Figure 4.13: VanGmodel for station*5 *at a depth of 0.1m*,0.3m,0.5m and 0.7m respectively.

4.5 Meteorological data

The recorded precipitation over the year 2021 by a meteorological station located at the monitoring site became very useful for climate study of that area and the recorded data were used in analyzing the temporal behaviour of simulated and observed moisture content (Figure 6.36 – 6.55) and the behaviour of simulated and observed pressure head (Figure 6.56-6.70). In Figure 4.29 the effective rainfall as obtained by the difference between rainfall and an estimation of the crop evapotranspiration are shown where the evapotranspiration is obtained by adding the transpiration and evaporation values, the effective precipitation was observed highest (almost 65 mm) in the month of December2021.

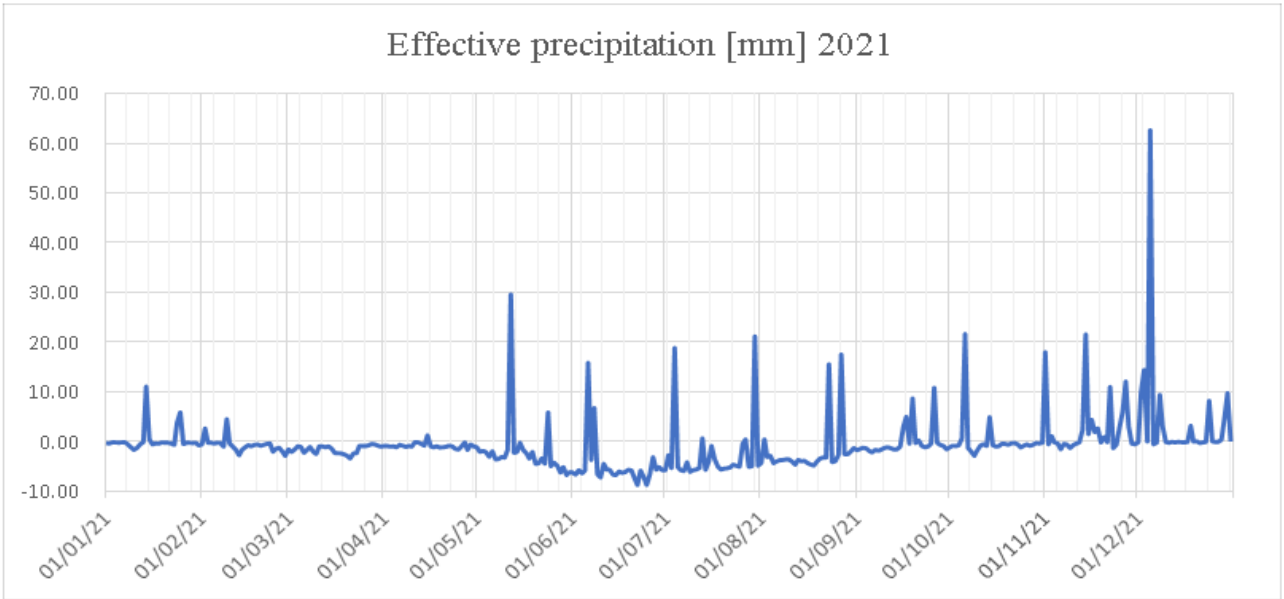

Figure 4.14: Effective precipitation in the year 2021.

5. METHODS

Creating and running a 3D model in Hydrus software is a straightforward process that involves importing site information such as soil properties, as in this case the site is located in a low-lying agricultural field at the southern boundary of Venice Lagoon, Italy. The area under consideration exhibits distinct characteristics, including heterogeneous soil properties with a presence of peat and a water table reaching a depth of approximately 1m. Observations for VWC were daily acquired at five stations in four consecutive depths chosen within the study area to explore the wide variety of the soil organic content.

5.1 Defining the domain and the mesh

The domain of the model is defined by fixing the boundaries of the soil and groundwater system. For the simulation a rectangular domain tool is selected, and 3D layered geometry was formed characterized by length (2600 cm), breadth (2000 cm) and highest point of (810 cm), moreover this ditch is located almost 200 cm below the ground level (Figure 5.2). After defining the domain, the user should create a mesh by selecting a tool named as Mesh Generator where the element size (TS) in the mesh is considered as 40 cm for this thesis. (Figure 5.1) illustrates five Geo-layers with specific mesh density in which layer5 has the highest mesh density.

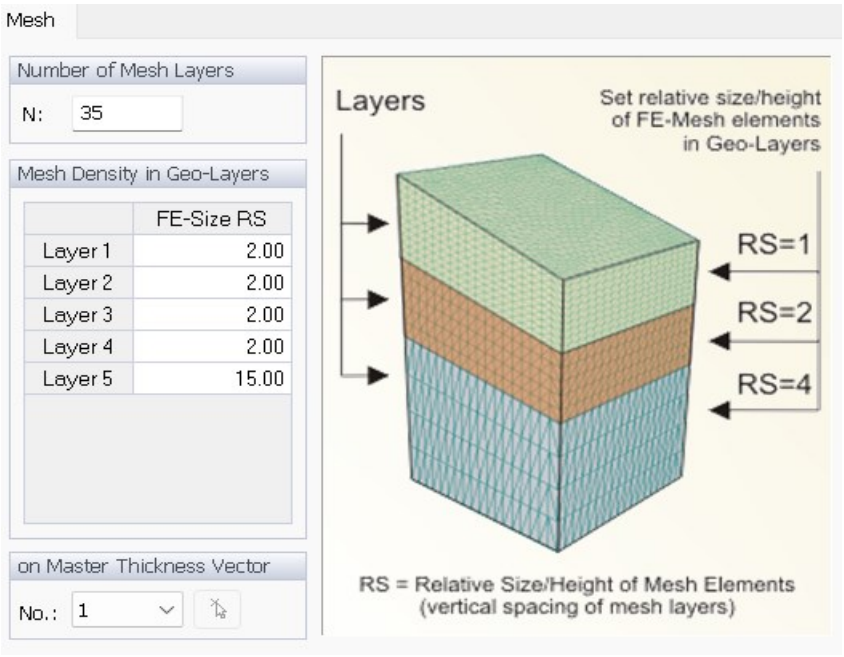

Figure 5.1 : *Geolayers with its mesh density.*

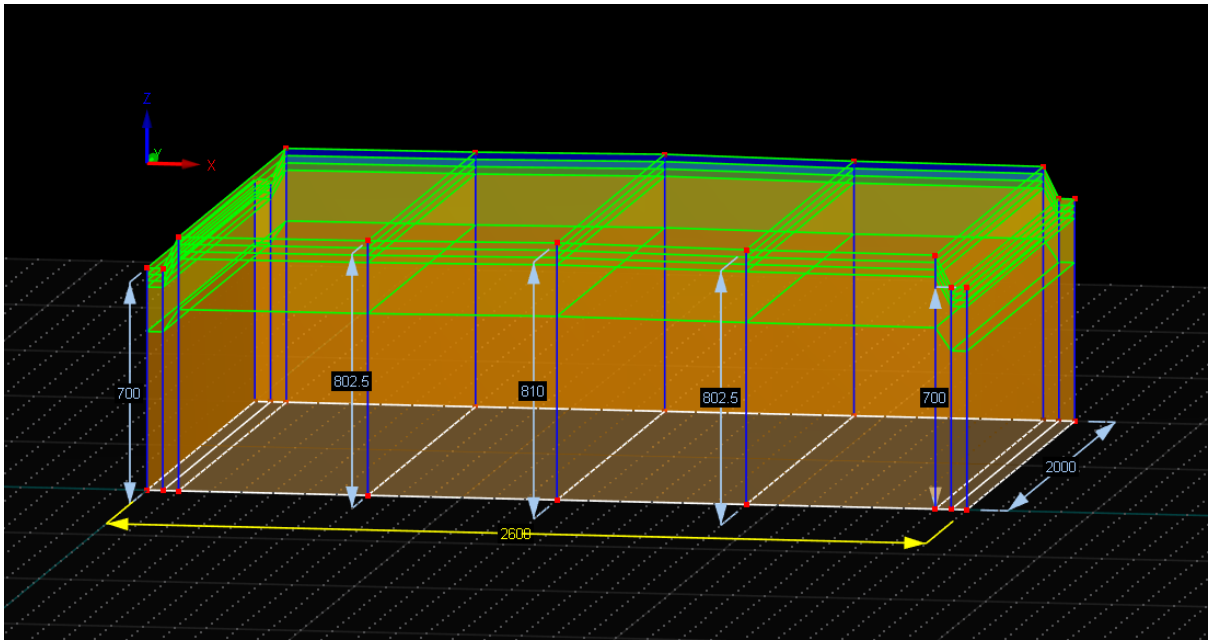

Figure 5.2: Geometry of the domain in cm *(made by points and lines in HYDRUS-3D)*

5.2 Flow and transport parameters

5.2.1 Main Process dialog window

In the Main Processes dialog window, users specify the processes to be simulated, i.e., Water Flow, Solute Transport, Heat Transport, and/or Root Water Uptake. The work of the thesis focuses on the water flow.

5.2.2 Time Information dialog window

The Time Information dialog window contains information associated with the Time Discretization, the time units and the implementation of boundary conditions, the initial time and the final time is provided as 0 (day) to 143 (day), in this thesis time variable boundary condition is selected as boundary condition where it repeats the same set of BC records each time.

5.2.3 Output Information

The output information window allows to select the print times that contain detailed information about pressure head and water content, T-level information is provided where every n time step is set as 1, (i.e.) the water content will be printed after an interval of each day in output results. Ultimately the total no of print iteration is established as 143, where

comprehensive details regarding pressure heads, water contents, concentrations, temperature and fluxes will be provided and presented in a printed format.

5.2.4 Iteration criteria

The Iteration criteria dialogue box provides information on the iterative process necessary to solve the nonlinear Richards equation. To obtain the solutions of the global matrix equation at each time step, a linearized system of algebraic equations is first derived and then solved using either Gaussian elimination or the conjugate gradient method. After solving the matrix equation, the coefficients are re-evaluated using the solution, and the new equations are solved again. This iterative process continues until an acceptable level of convergence is achieved, where the absolute change in pressure head or water content between two successive iterations is less than a small value determined by the imposed pressure head tolerance. For the simulation the maximum number of iterations was set as 10, water content tolerance was provided 0.001 and the pressure head tolerance was set as 1 cm. Finally, the initial condition for the water flow calculation in terms of pressure head was selected.

5.2.5 Numerical modelling of water flow in variably saturated conditions

The groundwater flow in porous medium where water saturation varies depending on the external conditions can be described by Richard's equation,

$$\sigma \frac{\partial \psi}{\partial t} = \nabla \cdot [K_s K_r (\nabla \psi + \eta_z)] + q \qquad (5.1)$$

where σ is the global storage coefficient, ψ is the pressure head, t is time, ∇ is the gradient operator, K_S is the saturated hydraulic conductivity tensor, K_r is the relative hydraulic conductivity, η_z is a vector equal to zero along the horizontal directions x and y equal to 1 in its z component (along the vertical direction), and q represents distributed source or sink terms (volumetric flow rate per unit volume) positive if injected.

The global storage term σ is:

$$\sigma = S_w S_s + \phi \frac{\partial S_w}{\partial \psi} \tag{5.2}$$

where $S_W = \theta/\theta_S$ is the water saturation (θ the volumetric moisture content and θ_S the saturated moisture content, usually equal to the porosity ϕ), and S_S is the specific elastic storage of the porous medium. The Richards equation is obtained by combining the Darcy equation applied to an unsaturated porous medium.

$$q = -K_s K_r (\nabla \psi + \eta_z) \tag{5.3}$$

The continuity equation for an incompressible fluid:

$$\nabla \cdot q + \frac{\partial \theta}{\partial t} = 0 \tag{5.4}$$

Equation (5.1) is highly non-linear due to the dependence of the storage and relative conductivity coefficients on ψ. This non-linear dependence has been extensively studied and can be expressed through constitutive relations of a semi-empirical nature, also known as characteristic relations, which describe the hydraulic properties of the porous medium. One of them, the van Genuchten equations adopted for the model, are shown below:

$$S_e = \frac{\theta - \theta_r}{\theta_s - \theta_r} = [1 - (\alpha\psi)^n]^{-m} \tag{5.5}$$

$$K(\theta) = K_s S_e^{1/2} [1 - (1 - S_e^{1-m})^m]^2 \tag{5.6}$$

where θ_r is the residual moisture content, K is the unsaturated hydraulic conductivity, S_e is the effective saturation, and α, n and $m = 1 - 1/n$ are empirical parameters.

5.2.6 Water flow parameters and neural network prediction

The software uses PTFS that rely on neural networks, as described by (Schaap, 2001), to make predictions about (A Closed-form Equation for Predicting the Hydraulic Conductivity of Unsaturated Soils1, 1980) water retention parameters and saturated hydraulic conductivity starting from textural information. If the user decides to use the parameter estimation feature, they must input initial estimates for the optimized soil hydraulic parameters and indicate which parameters should be optimized (by checking the appropriate boxes). The user may also set parameters constraints for the optimization process by entering minimum and maximum values, The software includes soil hydraulic parameter data for twelve textural classes of the USDA soil textural triangle based on (Robert F. Carsel, 1988) analytical functions for van Genuchten.

At last, after obtaining the predictions, a user can input the number of materials and them to the domain. In (Figure: 5.3) different colours represent different materials assigned to the domain.

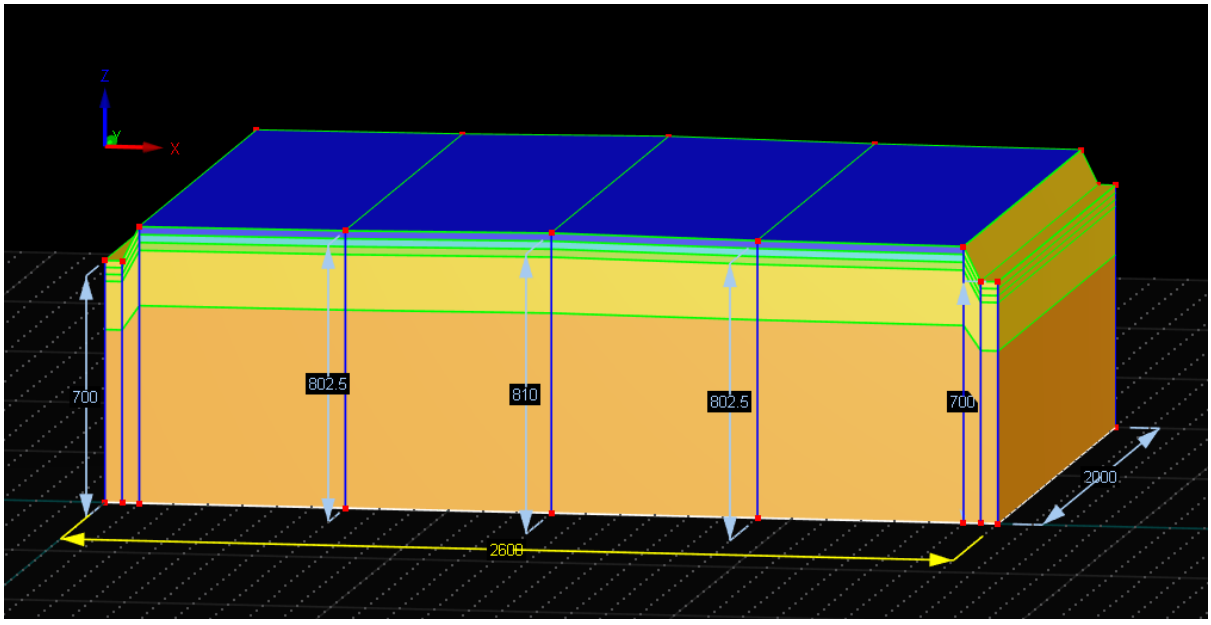

Figure 5.3: *Materials assigned to five different layers in the domain.*

5.2.7 Time Variable boundary condition

In the time variable dialog box information about precipitation, evaporation, and transpiration are inserted. The table has a capacity for about 32,000 records (depends on the number of columns). When a longer time record is to be simulated, then one needs to directly edit the Atmosph.in input file in the working directory using any standard software, such as MS Excel. The manually modified Atmosph.in file then needs to be imported back into HYDRUS.

5.3 FE-Mesh Parameters

In the command box shown in (Figure 5.4) the targeted element size is inserted following by the number of mesh layers to create the mesh in the next steps. The type of elements used in this case is taken as tetrahedral instead of triangular prism. (Figure 5.5) shows the final mesh used in the computation. The number of nodes and elements on the domain boundary are 18362 and 36720 respectively.

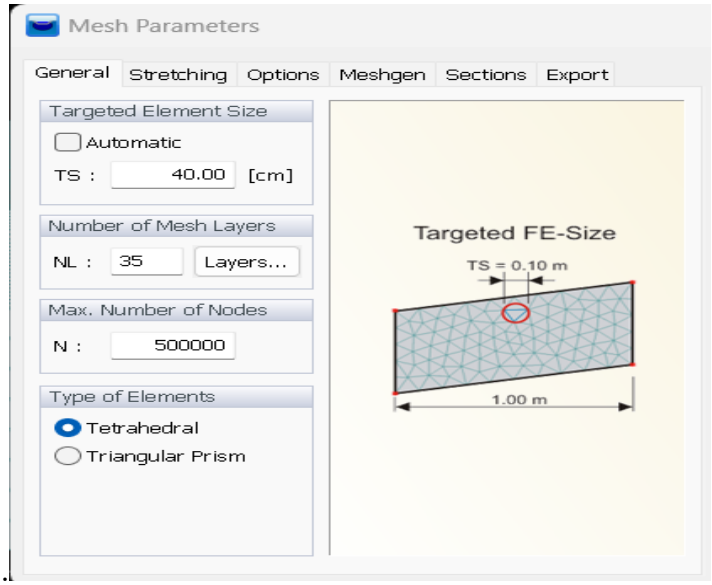

Figure 5.4: Mesh parameters for the construction of the domain.

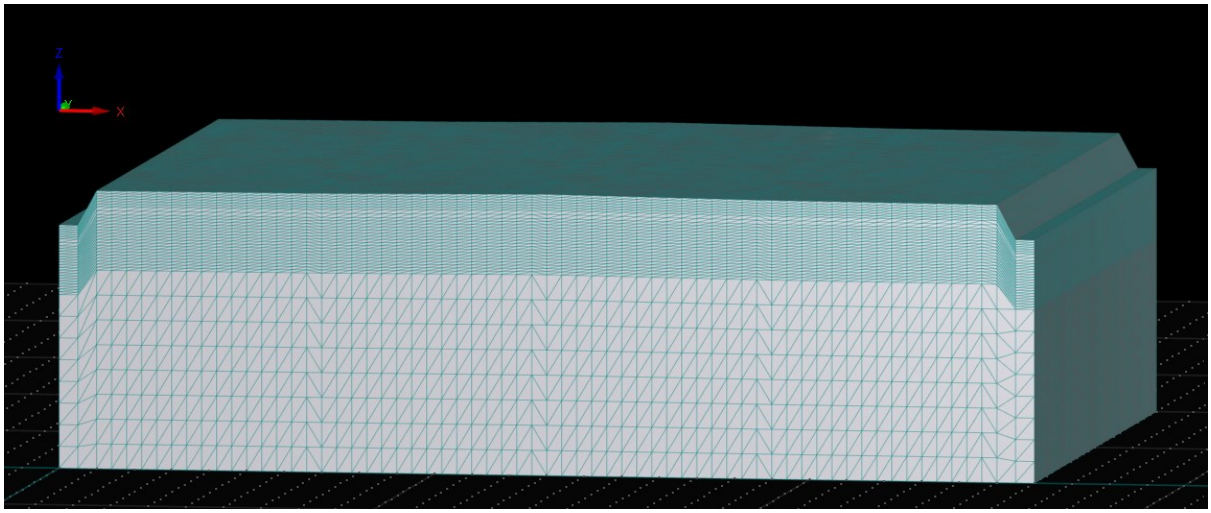

Figure 5.5: FE mesh view for the selected domain.

5.4 Default domain properties and initial conditions

As soon as the finite element mesh is created, the initial Default Domain Properties for the rectangular two-dimensional domains and layered three-dimensional domains are adjusted. These parameters will initially apply to every horizontal layer of the transport domain but can be changed visually later. Numerous variables are involved in this process. The set of rules for the boundary conditions includes codes such as 0 indicating absence of flow, -1 indicating constant flux, +1 indicating constant head, -2 indicating unsaturated seepage face and +2 indicating saturated seepage face. Additionally, codes such as -3 (-7, -8, -9) signify variable flux while +3 (+7, +8, +9) indicates variable head. Other codes include -4 for atmospheric, -5 for tile drain, and -6 for free drainage. In this thesis no flux boundary condition (0), seepage face boundary condition (through which water leaves the saturated part of the flow domain +2), and atmospheric boundary condition (-4) are used which is illustrated in (Figure 5.7).

Observation nodes (Figure 5.6) are inserted at the face of the domain to compare the computed and observed water content and pressure head.

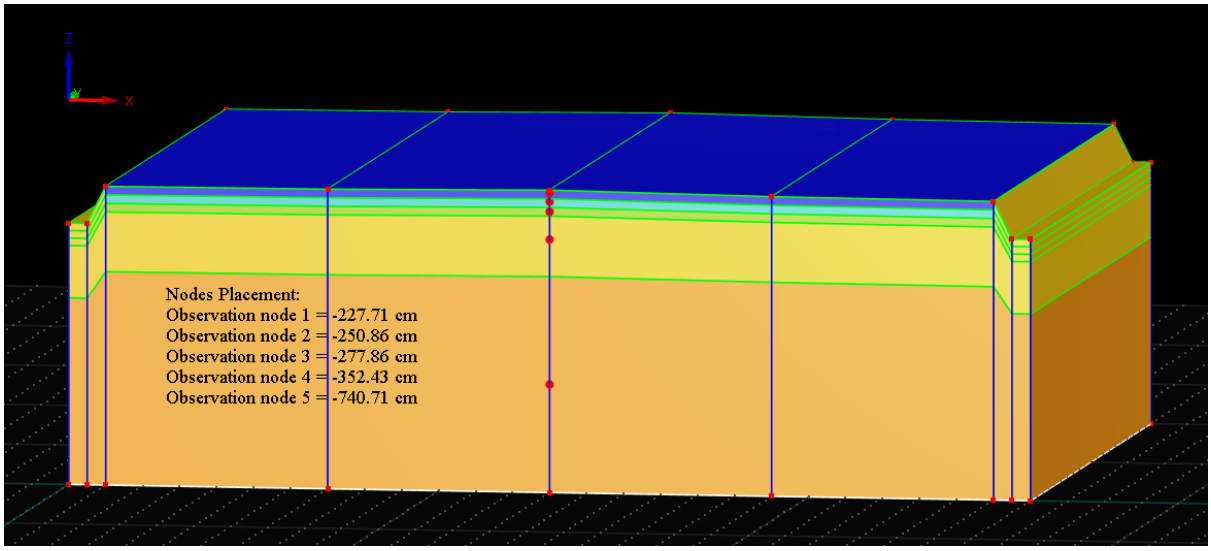

Figure 5.6: Observation points in the domain.

In the Initial Conditions a linear distribution of the pressure head with depth is selected, at the top and bottom of the model pressure head values are given equal to -100 cm and 700 cm respectively.

5.5 Defining the boundary conditions.

Boundary conditions can be specified in HYDRUS either selecting them directly on the finite element mesh or by selecting geometrical objects also known as Geo Objects (Figure 5.7). In this case the boundary conditions are applied on the Geo Objects. The user just needs to go to the edit bar to add a new water flow BDRC and then assign those BDRC to the respective domain.

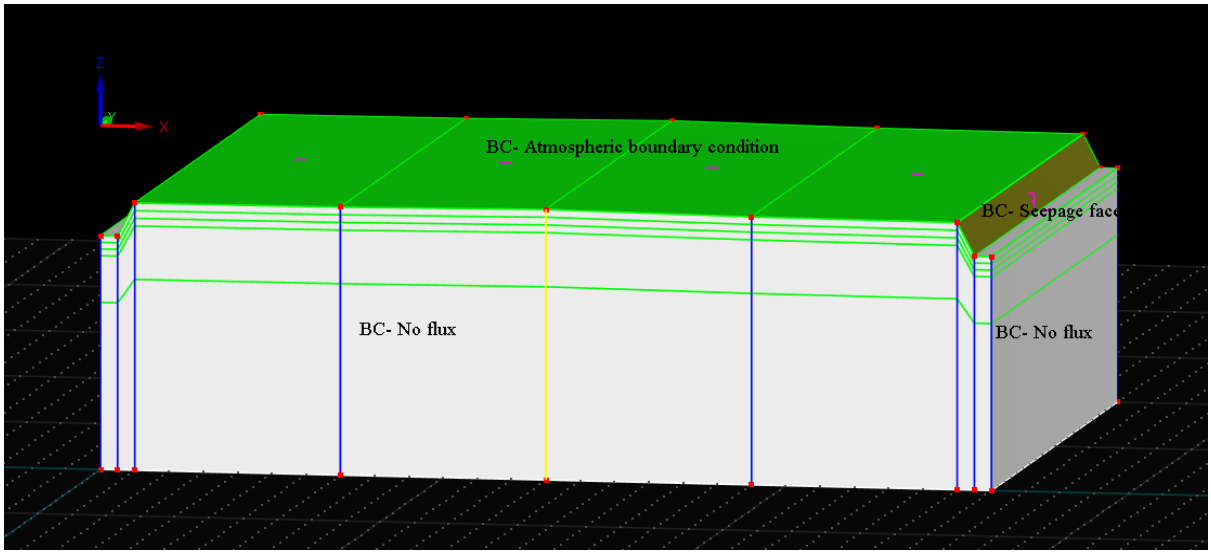

Figure 5.7 :Boundary conditions assigned to the domain.

5.6 Running the model.

After completing all the above steps, the user should initiate to run the model by selecting the Run Model tool. The simulation results will be displayed after the simulation time has elapsed which usually depend on the time interval and size of the file.

5.7 Analyse and view results

A range of tools is provided by HYDRUS-3D to visualize and analyze the simulation results. Usually, the results are analysed to gain insights into the soil and groundwater system and to evaluate the model capability to reproduce available observations. Visualizations such as contour plots, time-series graphs and animations can be generated to present the results. An example is provided in (Figure 5.8).

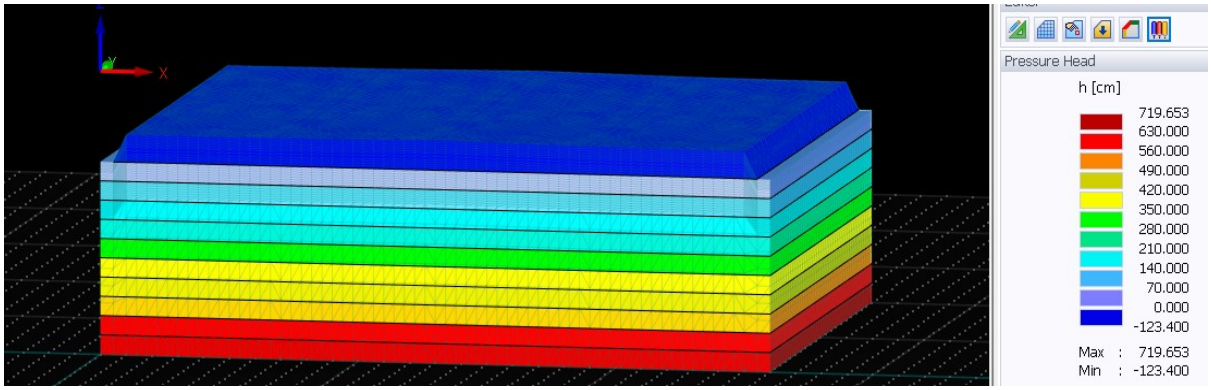

Figure 5.8: Initial pressure head in the model domain.

6. RESULTS AND DISCUSSION

The simulation span was given by time interval from 8 June 2021 to 28 October 2021 and a daily time step has been used for the simulation.

6.1 Comparing observed and simulated moisture content value.

The comparison between the observed and simulated water content is provided from (Figure 6.1 to Figure 6.20)

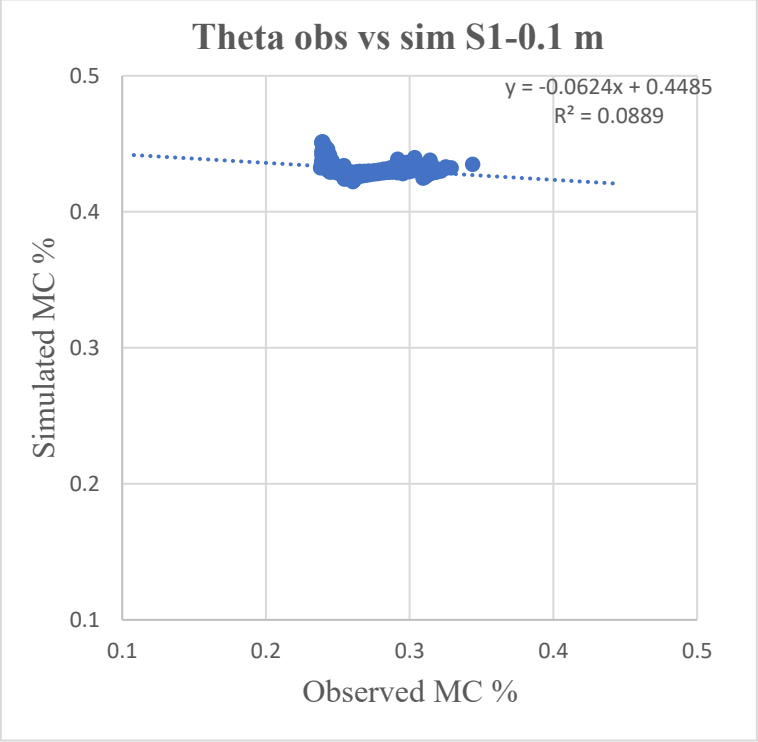

Figure 6.1: Simulated versus observed moisture content with trendline and equation for station S*1 at a depth of 0.1 m.*

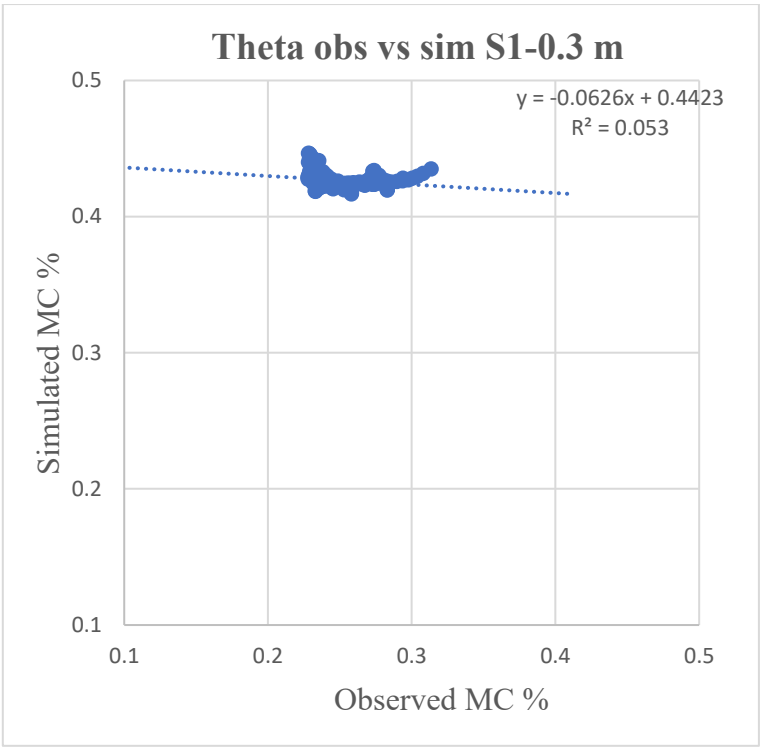

Figure 6.2: Simulated versus observed moisture content with trendline and equation for station S1 at a depth of 0.3 m.

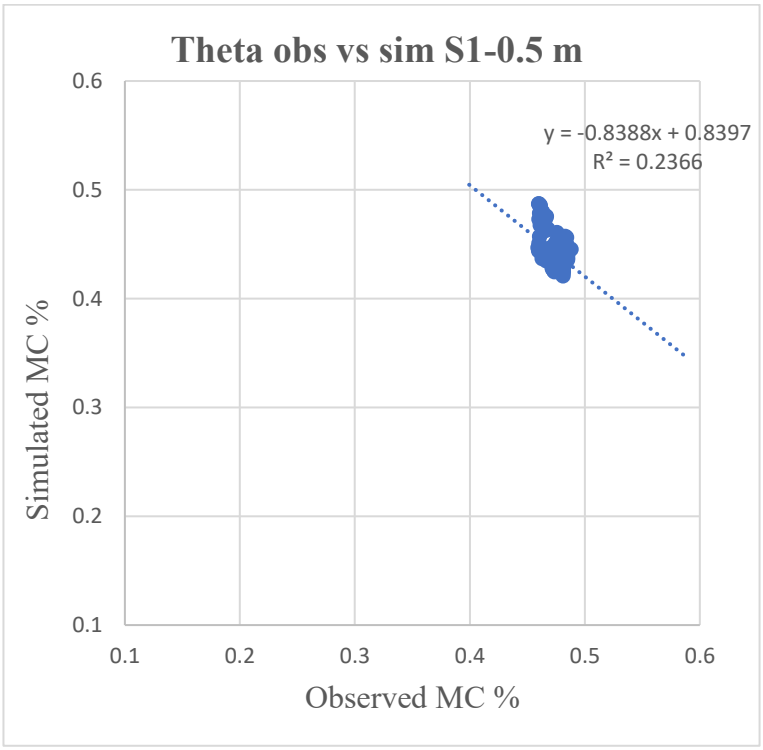

Figure 6.3: Simulated versus observed moisture content with trendline and equation for station S1 at a depth of 0.5 m.

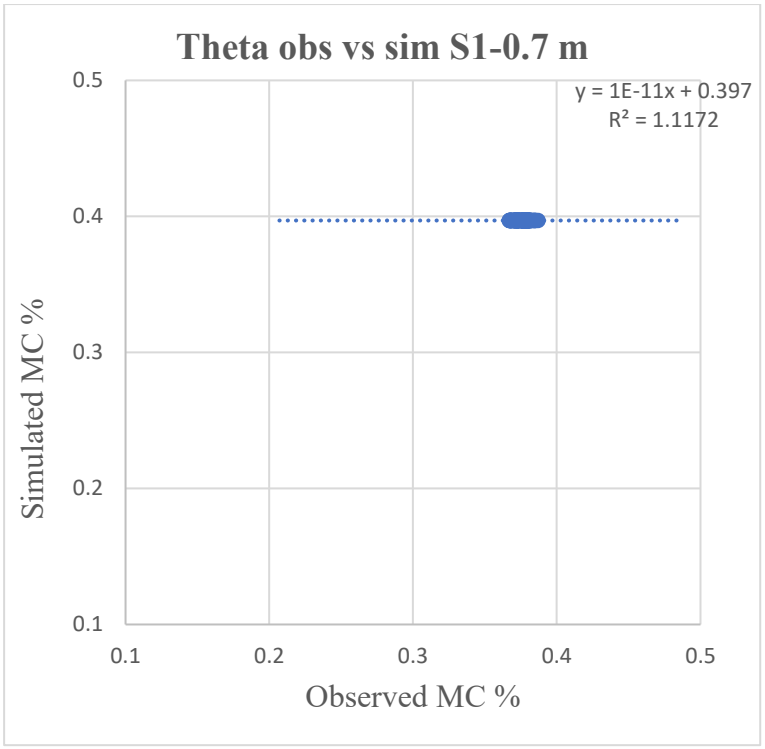

Figure 6.4: Simulated versus observed moisture content with trendline and equation for station S*1 at a depth of 0.7 m.*

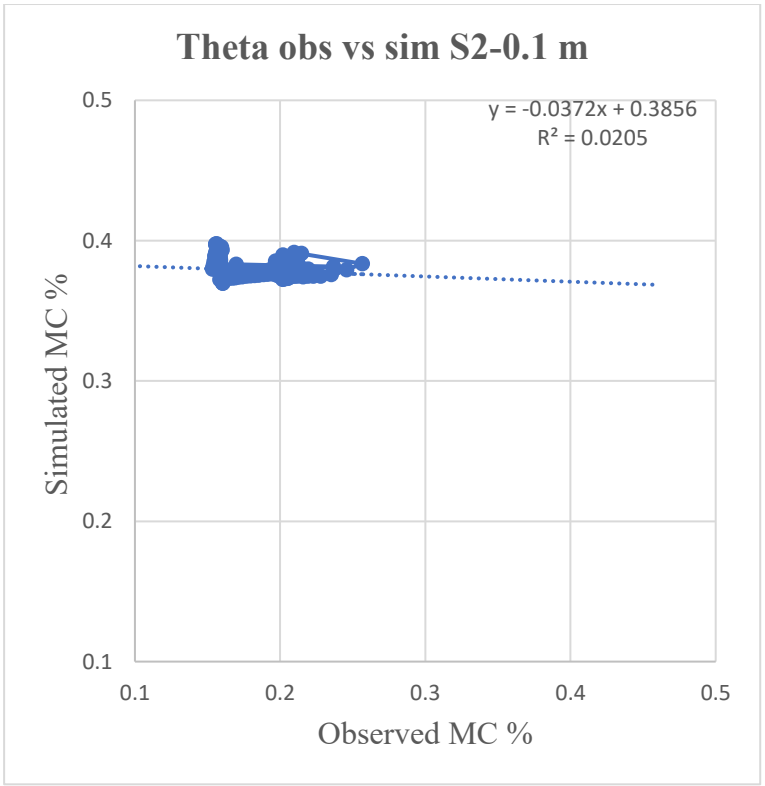

Figure 6.5: Simulated versus observed moisture content with trendline and equation for station S2 *at a depth of 0.1 m.*

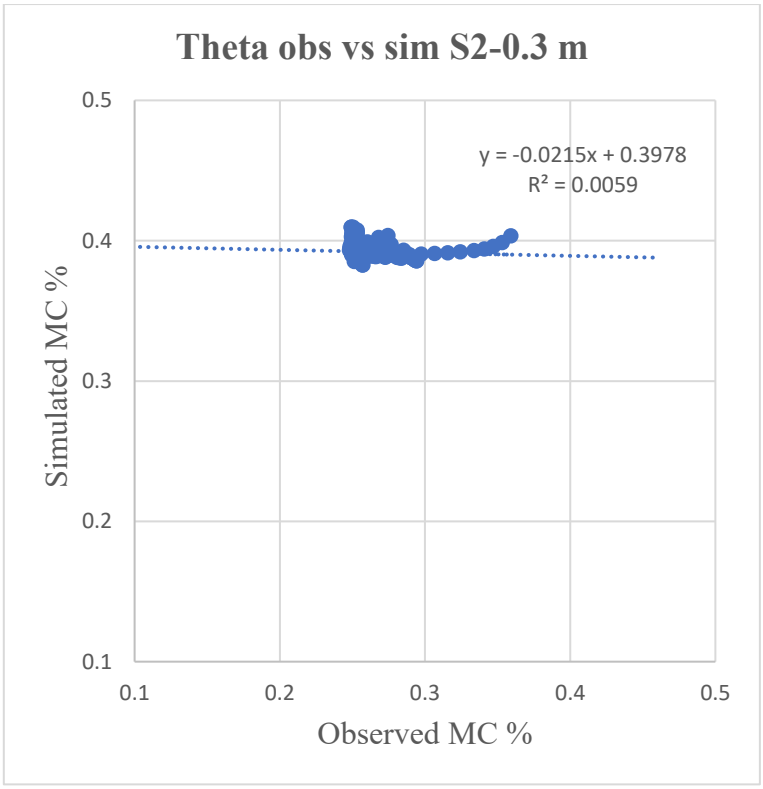

Figure 6.6: Simulated versus observed moisture content with trendline and equation for s station S2 at a depth of 0.3 m.

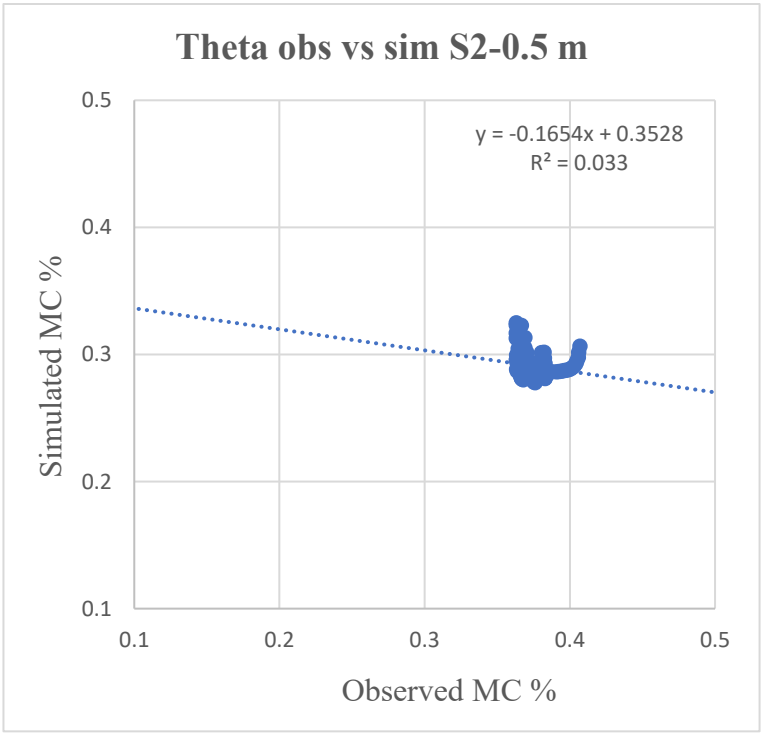

Figure 6.7: Simulated versus observed moisture content with trendline and equation for station S2 *at a depth of 0.5 m.*

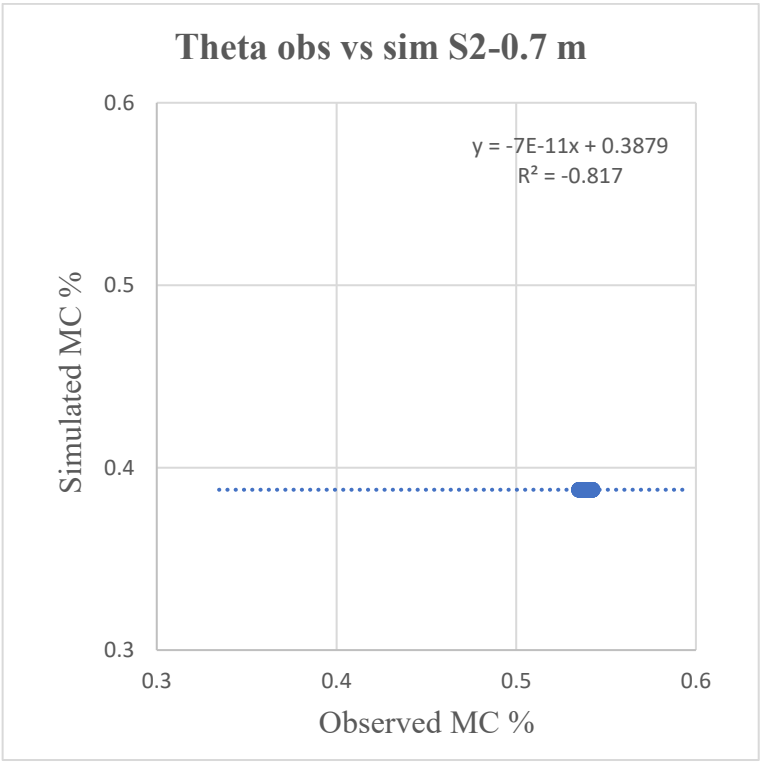

Figure 6.8: Simulated versus observed moisture content with trendline and equation for station S2 *at a depth of 0.7 m.*

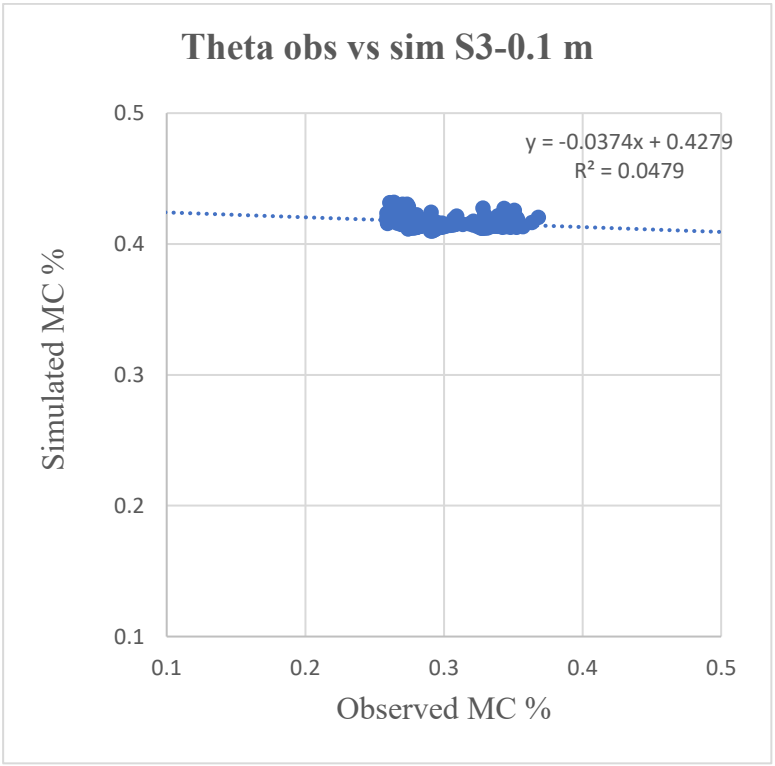

Figure 6.9: Simulated versus observed moisture content with trendline and equation for station S3 *at a depth of 0.1 m.*

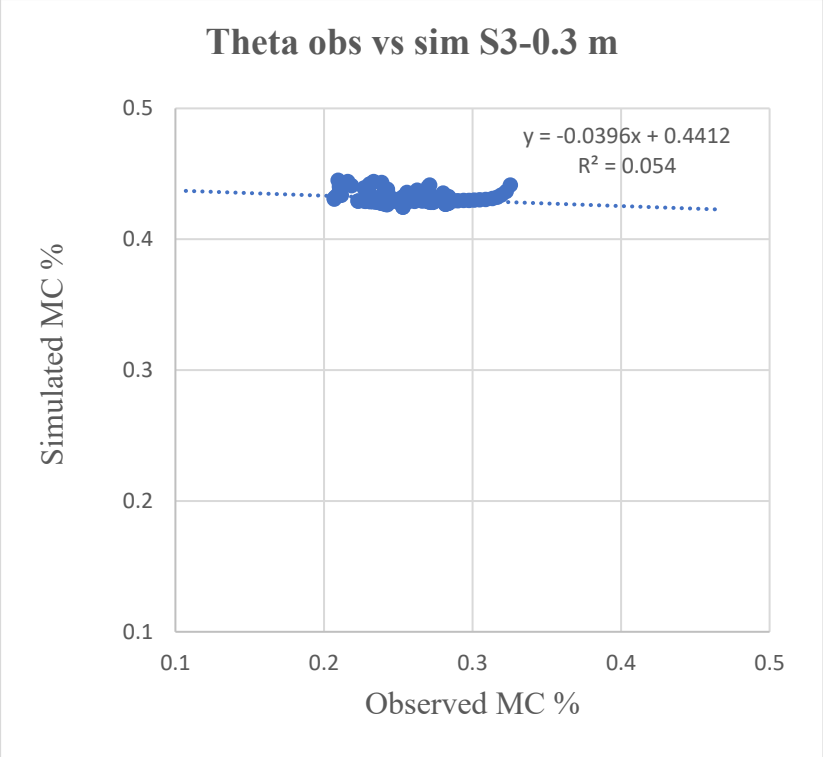

Figure 6.10: Simulated versus observed moisture content with trendline and equation for station S3 at a depth of 0.3 m.

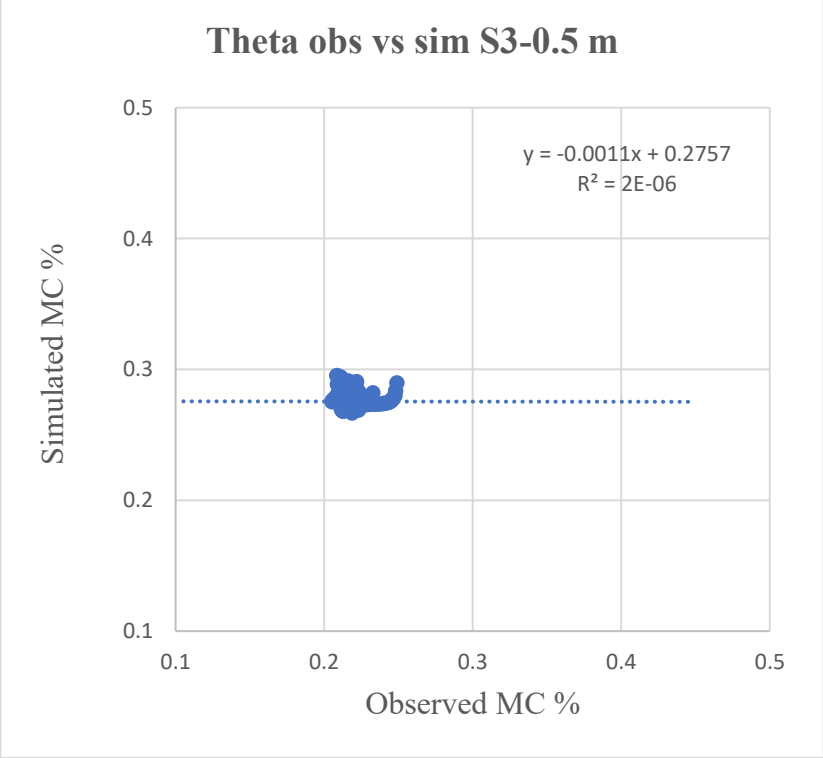

Figure 6.11: Simulated versus observed moisture content with trendline and equation for station S3 *at a depth of 0.5 m.*

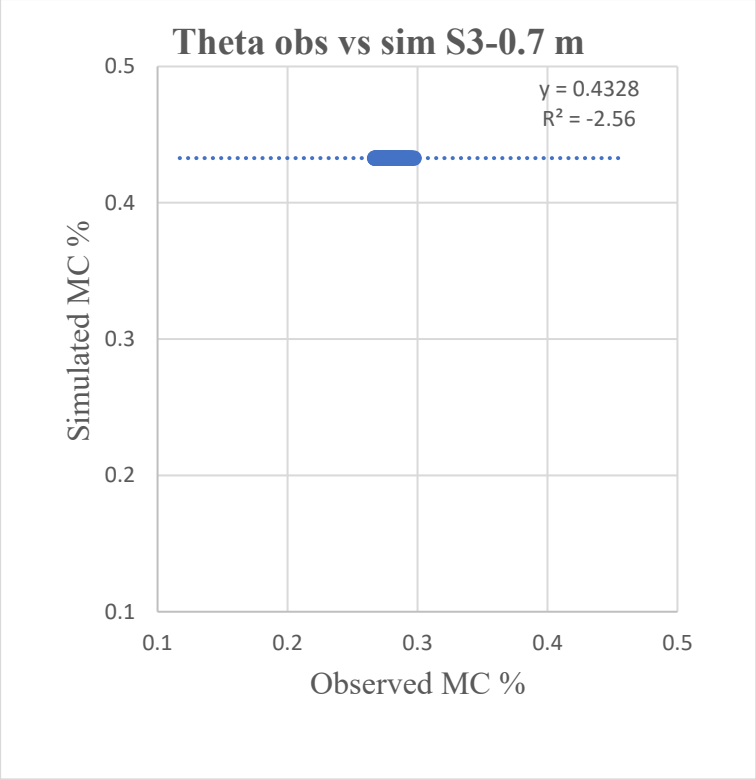

Figure 6.12: Simulated versus observed moisture content with trendline and equation for station S3 *at a depth of 0.7 m.*

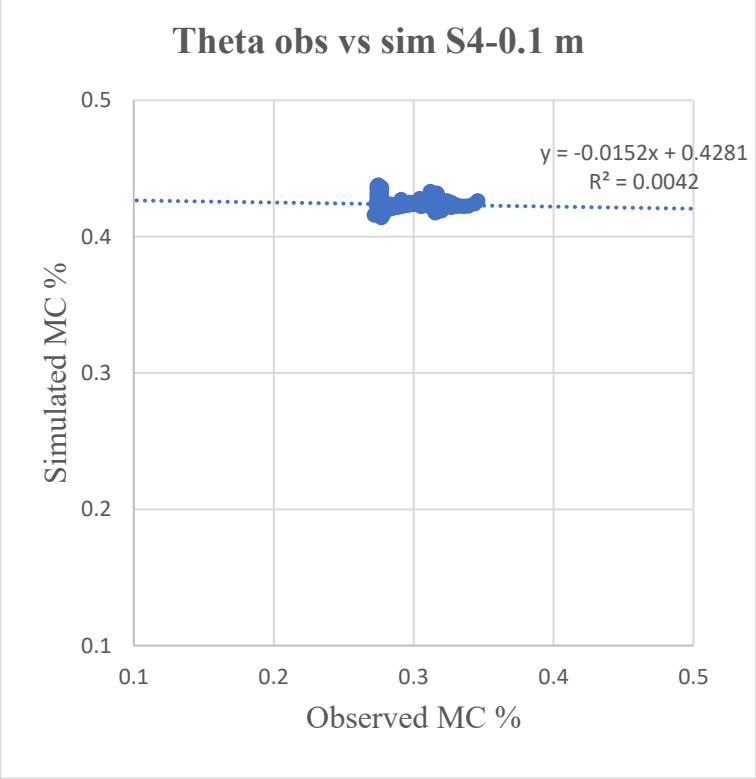

Figure 6.13: Simulated versus observed moisture content with trendline and equation for station S4 *at a depth of 0.5 m.*

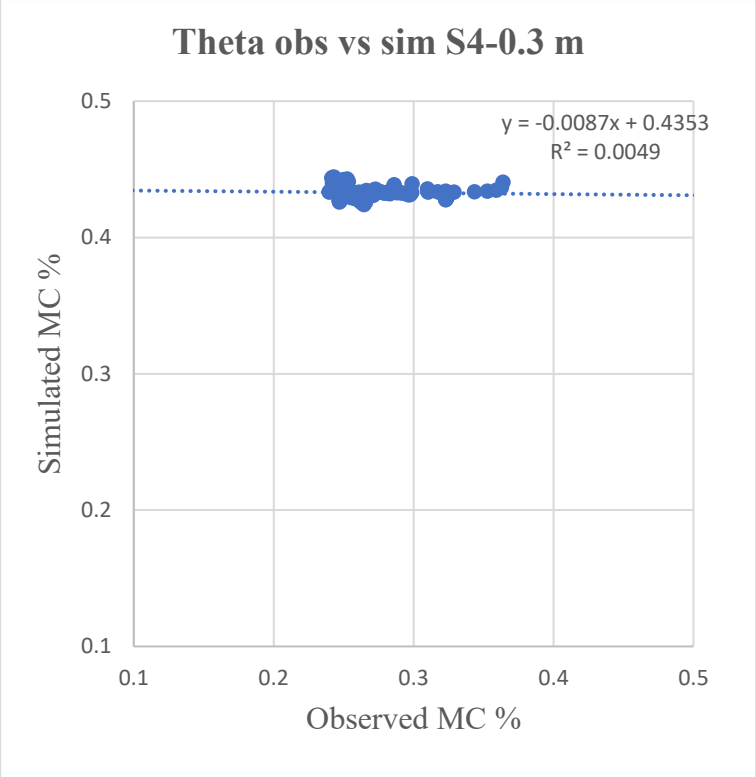

Figure 6.14: Simulated versus observed moisture content with trendline and equation for station S4 *at a depth of 0.3 m.*

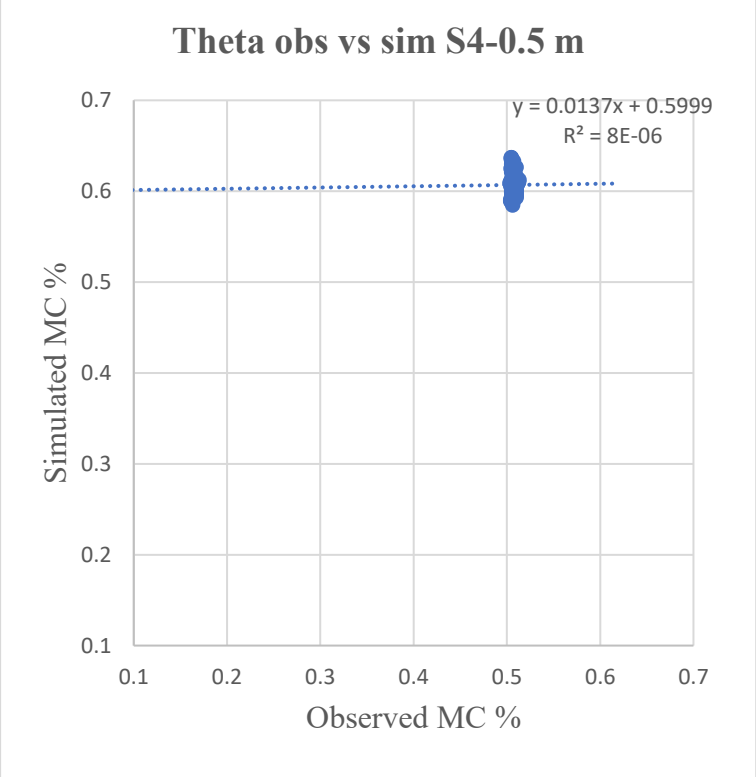

Figure 6.15: *Simulated versus observed moisture content with trendline and equation for* station S4 *at a depth of 0.5 m.*

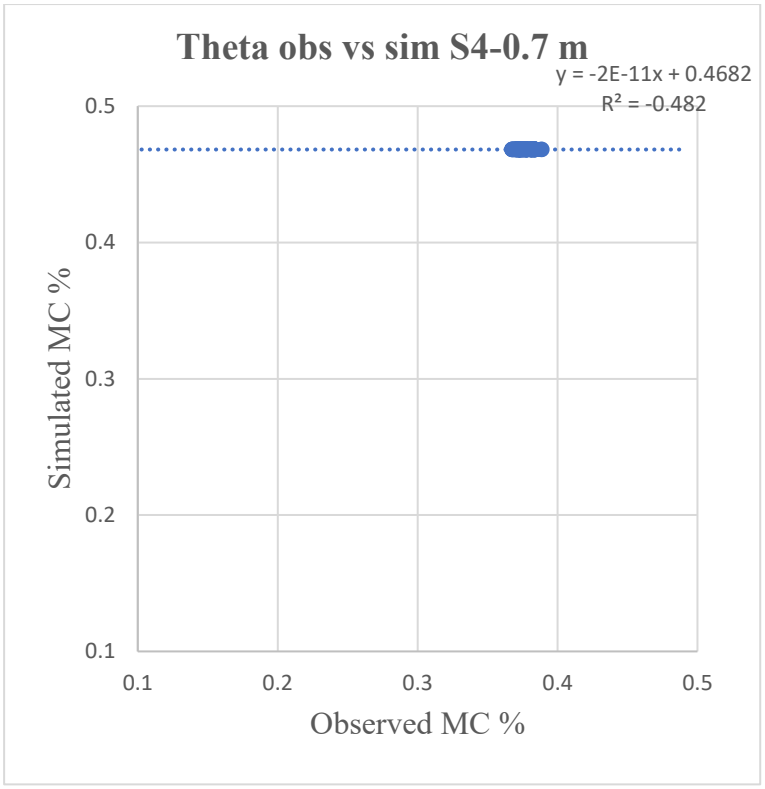

Figure 6.16: Simulated versus observed moisture content with trendline and equation for station S4 at a depth of 0.7 m.

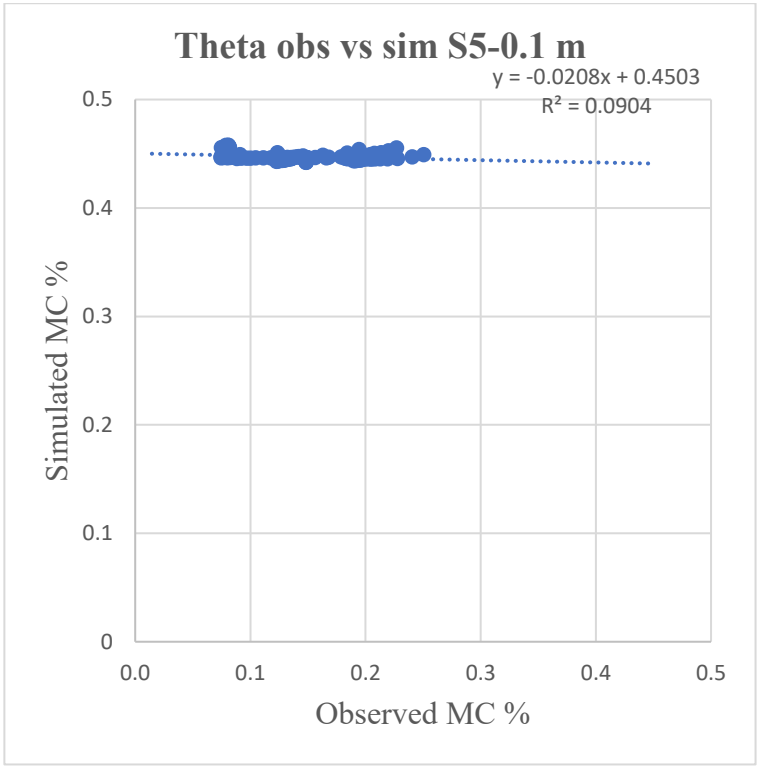

Figure 6.17: Simulated versus observed moisture content with trendline and equation for station S5 at a depth of 0.1 m.

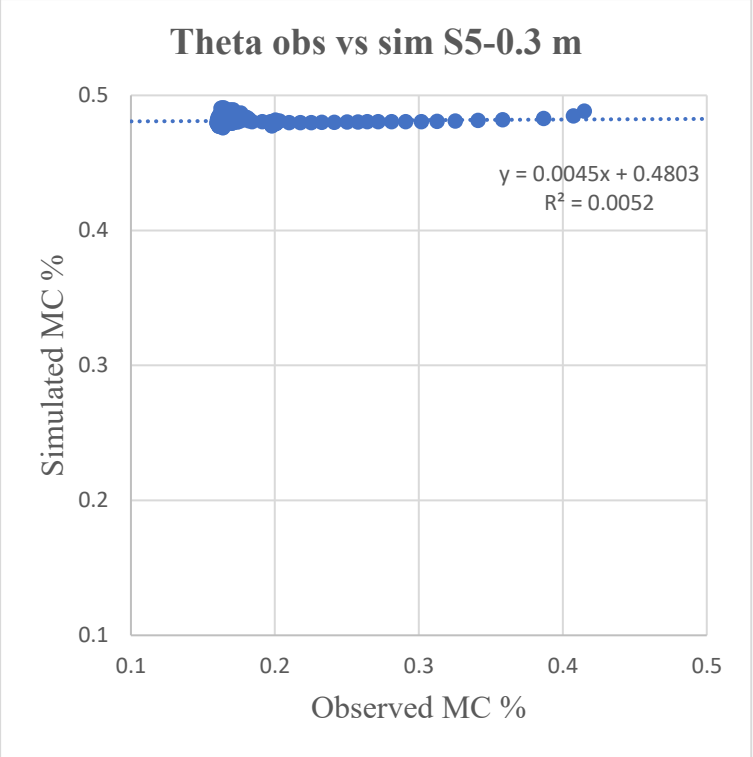

Figure 6.18: Simulated versus observed moisture content with trendline and equation for station S5 at a depth of 0.3 m.

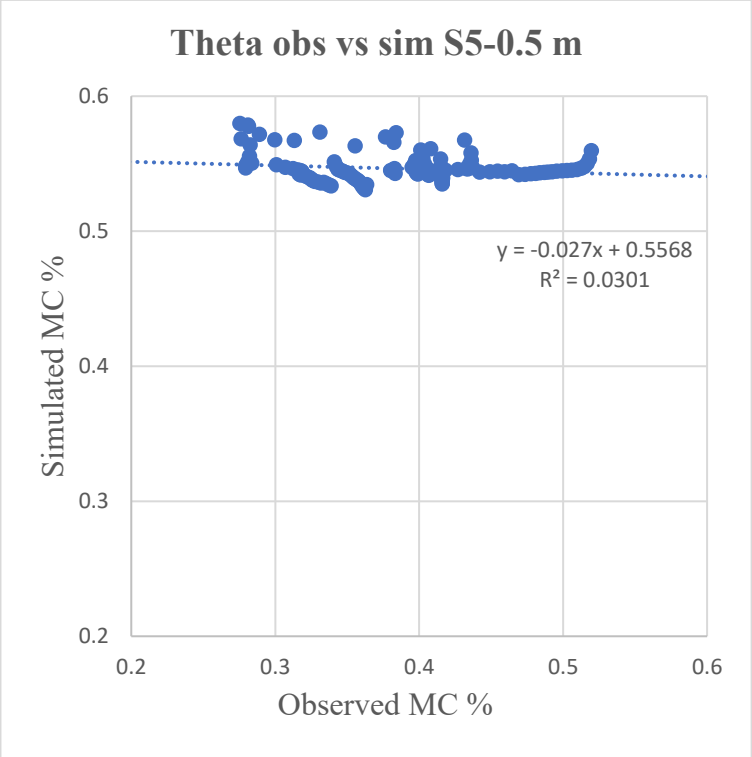

Figure 6.19: Simulated versus observed moisture content with trendline and equation for station S5 at a depth of 0.5 m.

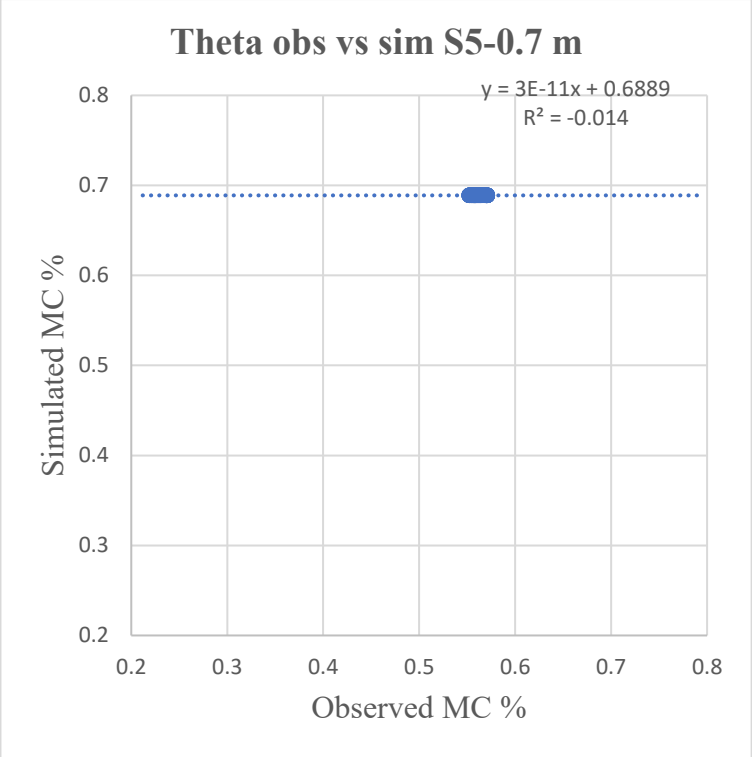

Figure 6.20: Simulated versus observed moisture content with trendline and equation for station S5 *at a depth of 0.7 m.*

In Figures (6.1 to 6.20) observed moisture content refers to the measurements obtained in the field during the year 2021. On the other hand, the simulated moisture content represents the values computed by the HYDRUS-3D simulation. By employing mathematical equations, soil properties, boundary conditions, and user-provided inputs the software predicts the movement of water in the soil over time. The simulated moisture content is depicted as dots on the graph. Ideally, the simulated moisture content should closely align with the observed data. A strong agreement is indicated when the simulated line closely follows the trend and variations of the observed data points, Figures (6.1 to 6.20) show that the model can better reproduce the field records in station S1 and station S2. However, discrepancies may arise due to the factors such as uncertainties in input parameters, measurement inaccuracies, or limitations of the simulation model.

Moreover, the equation provided in each graph represents the mathematical expression that describes the relationship between the observed and simulated moisture content. It is typically derived using regression analysis. This equation also allows us to identify any systematic biases or proportional scaling between the observed and simulated data. It often includes slope and intercept terms which indicate the rate at which the simulated value

change in response to changes in the observed values, basically it provides insights into the proportional relationship between two datasets.

The coefficient of determination which is the R-squared value, is a statistical measure that quantifies the goodness of the fit between the observed and simulated data points. Ranging from 0 to 1, a greater R indicates a stronger correlation and a better fit between the two datasets.

In summary, the graph obtained from comparing observed and simulated moisture content in HYDUS-3D is valuable for the assessment of the model's ability to replicate field conditions and understanding soil water movement and dynamics. It helps in validating the model's accuracy and reliability, pinpointing areas that require improvement, and supporting decision-making in irrigation, water management or soil-related studies.

6.2 Comparing observed and simulated matric potential.

The comparison between the observed and simulated matric potential is provided from Figure 6.21 to 6.40.

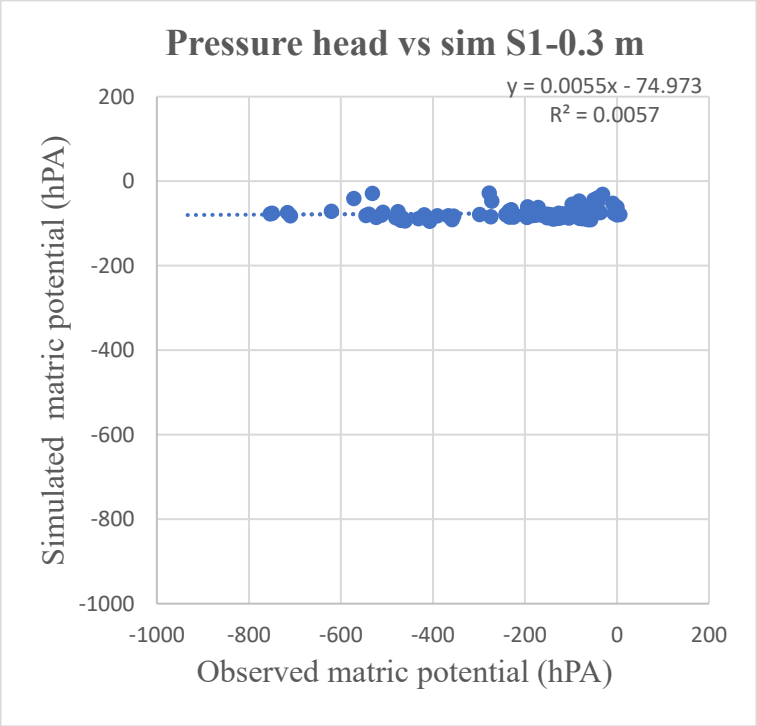

Figure 6.21: Simulated versus observed matric potential with trendline and equation for station S1 at a depth of 0.3 m.

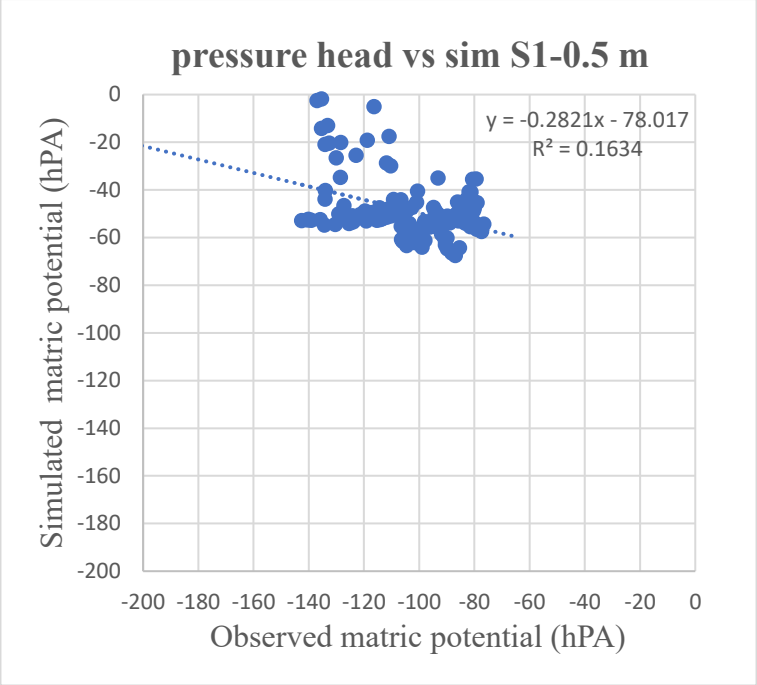

Figure 6.22: Simulated versus observed matric potential with trendline and equation for station S1 at a depth of 0.5 m.

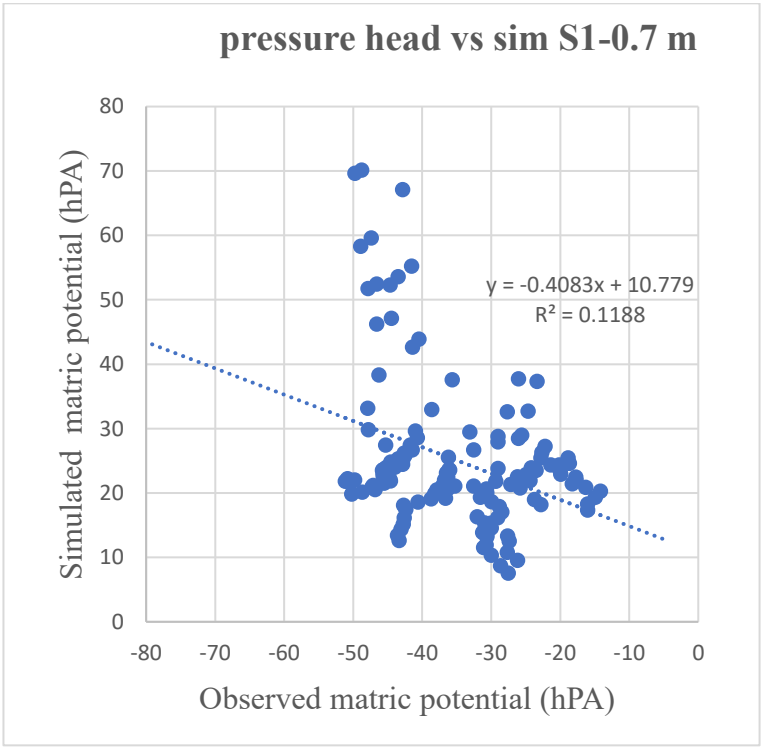

Figure 6.23: Simulated versus observed matric potential with trendline and equation for station S1 at a depth of 0.7 m.

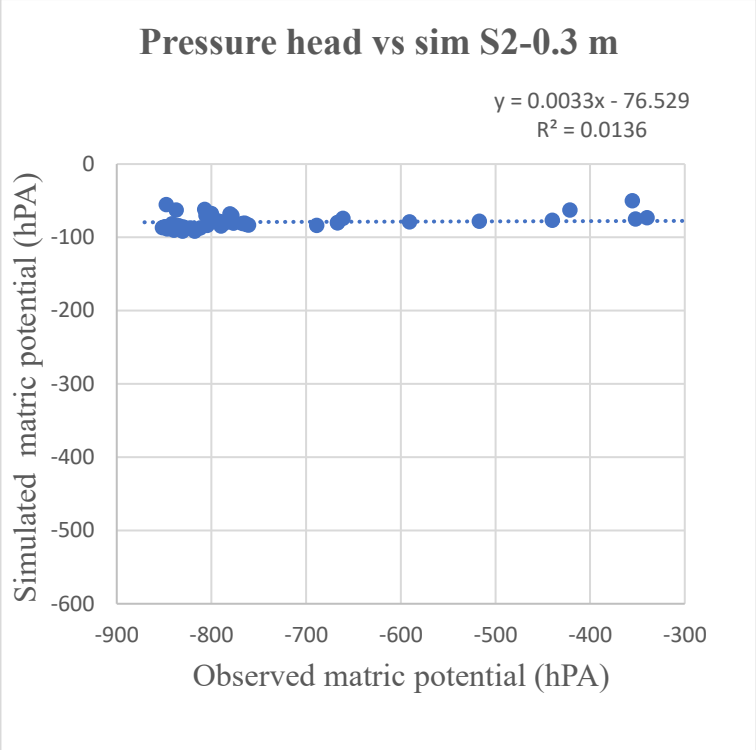

Figure 6.24: Simulated versus observed matric potential with trendline and equation for station S*1 at a depth of 0.3 m.*

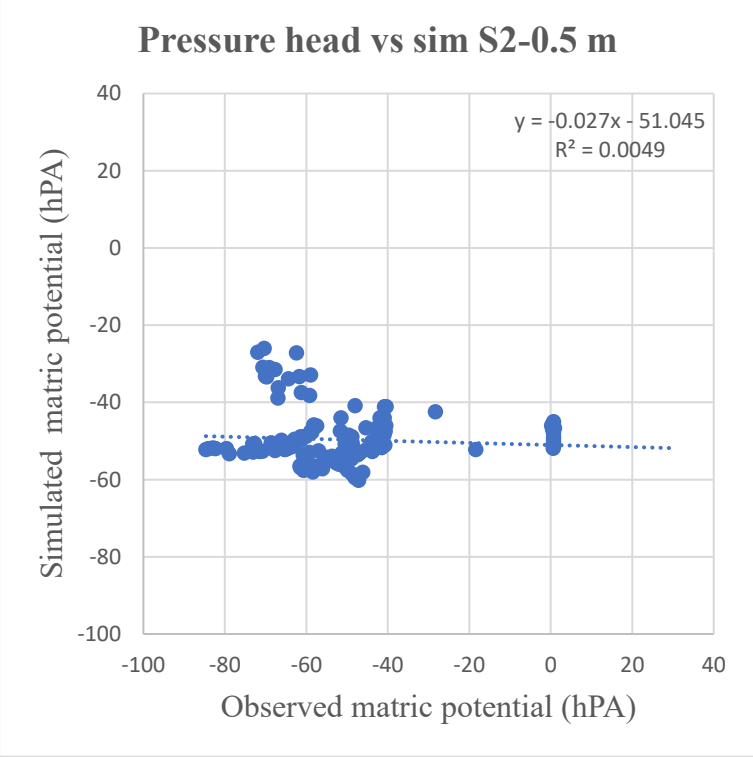

Figure 6.25: Simulated versus observed matric potential with trendline and equation for station S2 *at a depth of 0.5 m.*

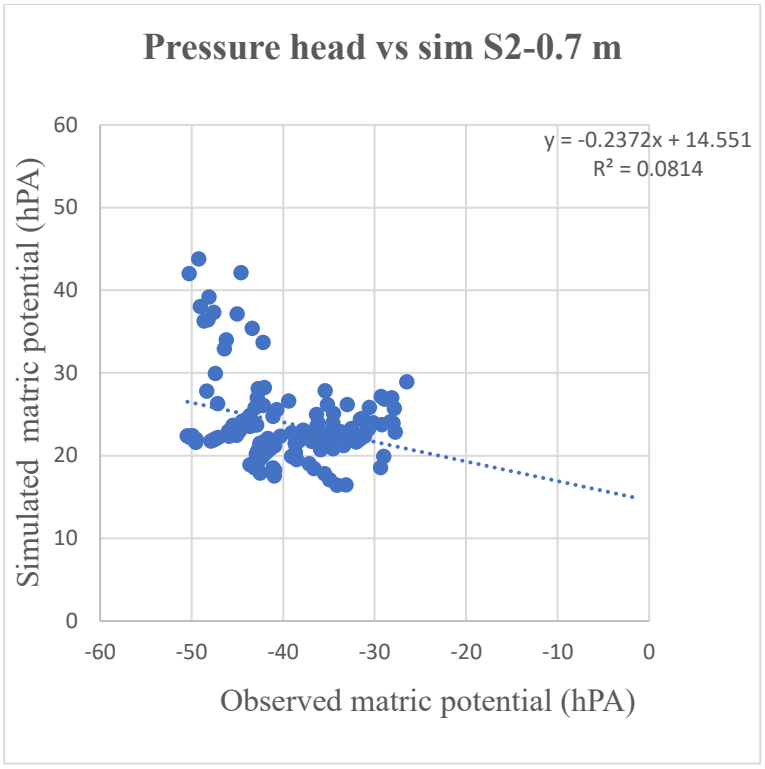

Figure 6.26: Simulated versus observed matric potential with trendline and equation for station S2 *at a depth of 0.7 m.*

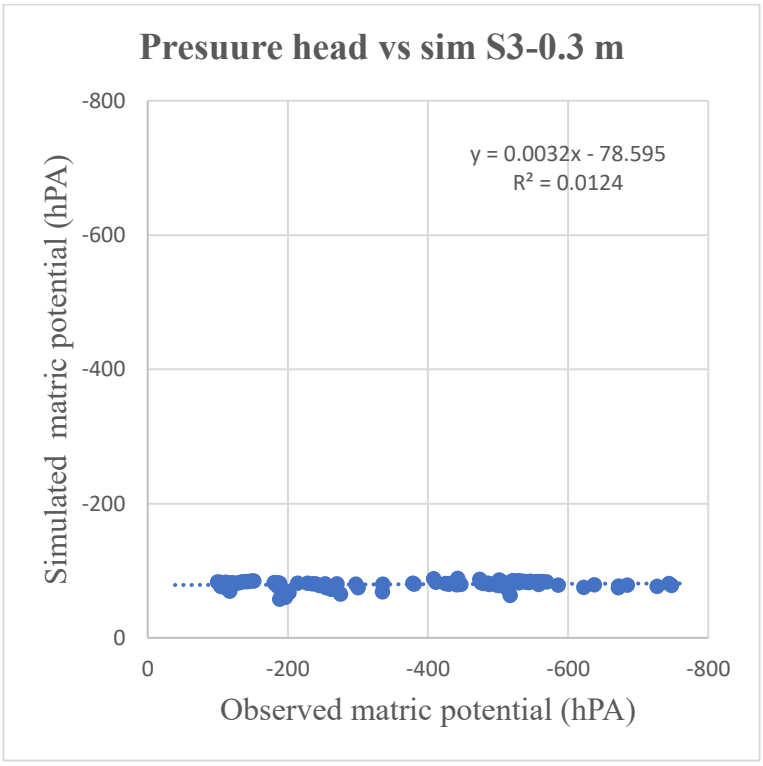

Figure 6.27: Simulated versus observed matric potential with trendline and equation for station S3 at a depth of 0.3 m.

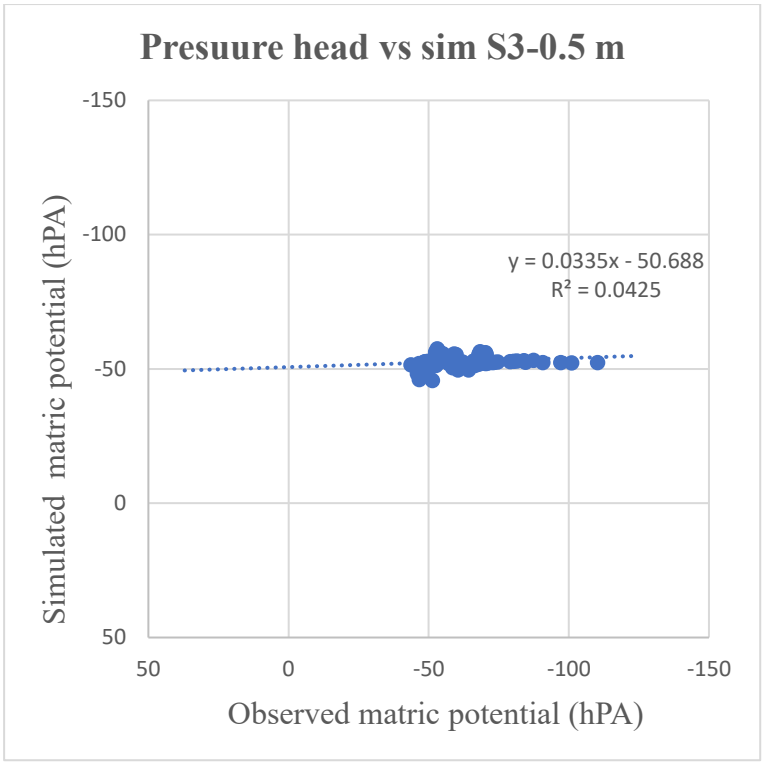

Figure 6.28: Simulated versus observed matric potential with trendline and equation for station S3 at a depth of 0.5 m.

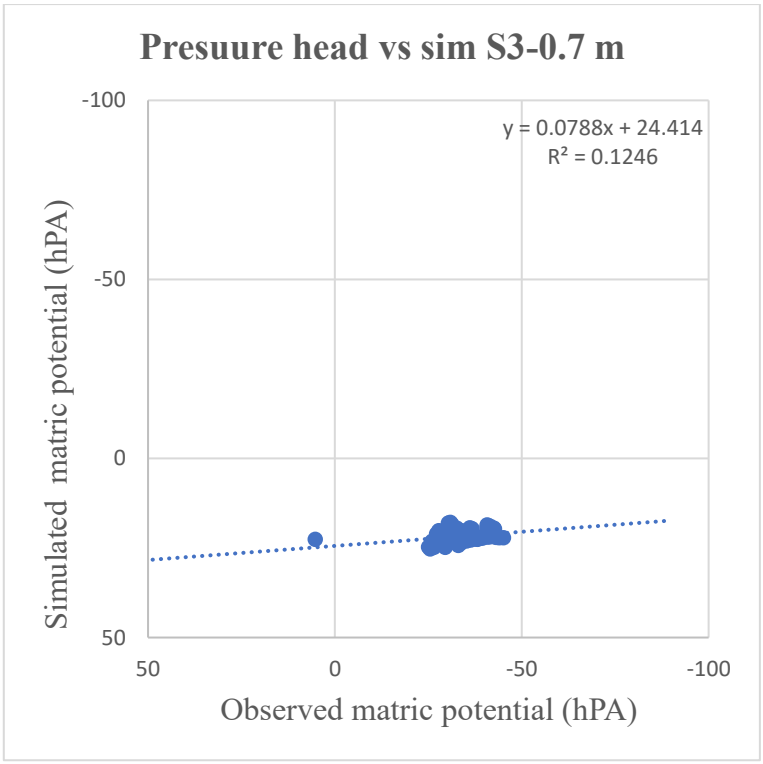

Figure 6.29: Simulated versus observed matric potential with trendline and equation for station S3 *at a depth of 0.7 m.*

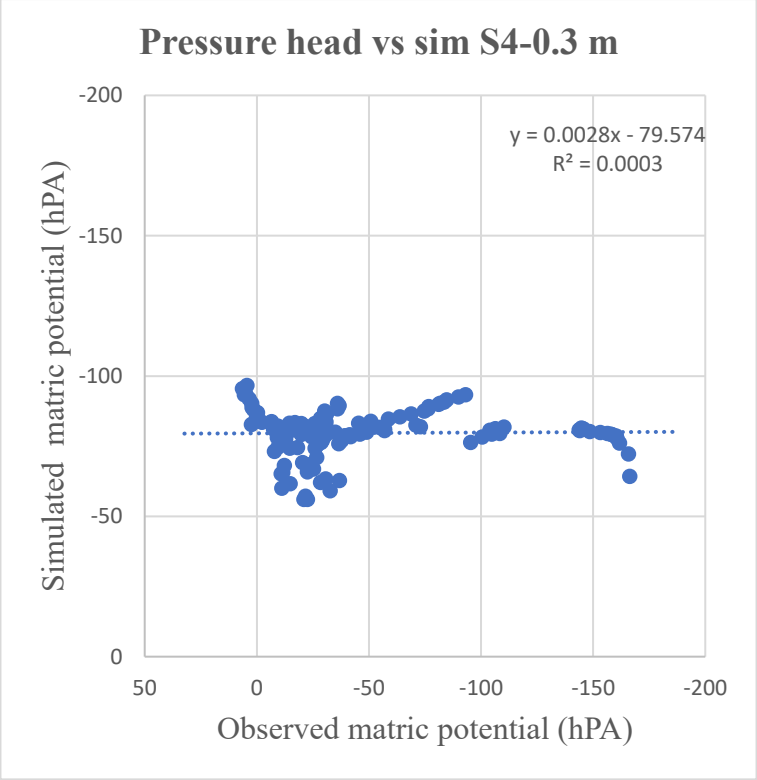

Figure 6.30: Simulated versus observed matric potential with trendline and equation for station S4 at a depth of 0.3 m.

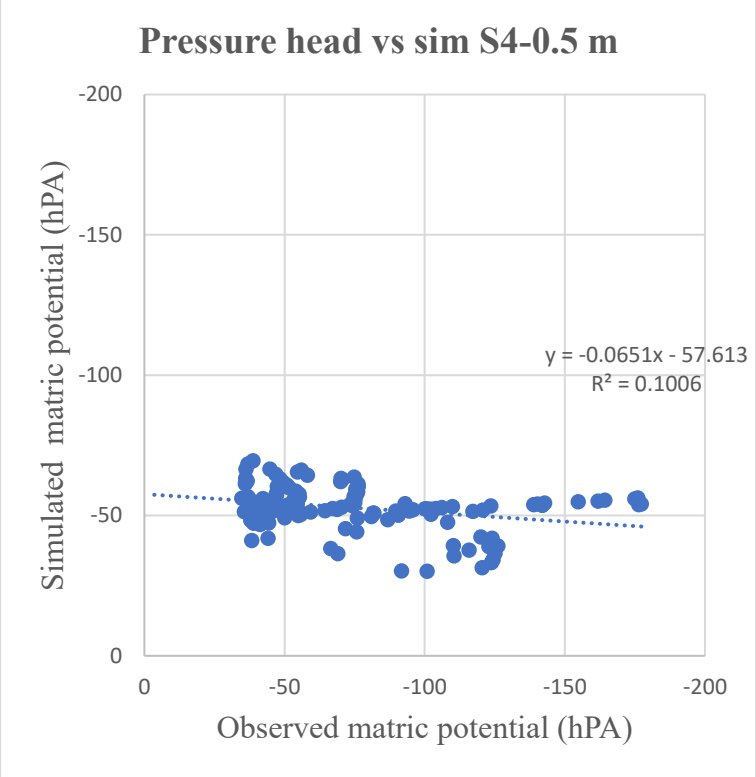

Figure 6.31: Simulated versus observed matric potential with trendline and equation for station S4 *at a depth of 0.5 m.*

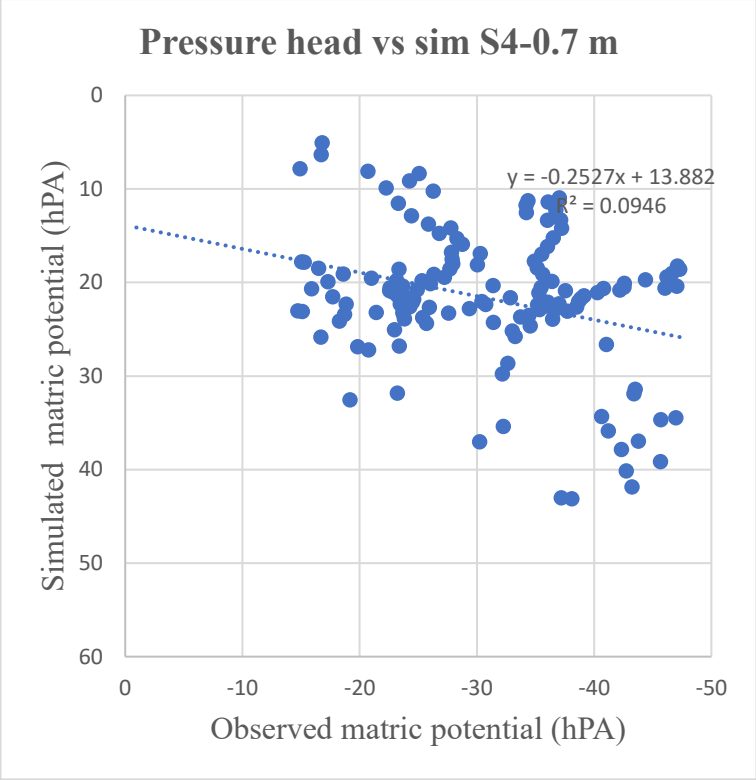

Figure 6.32: Simulated versus observed matric potential with trendline and equation for station S4 *at a depth of 0.7 m.*

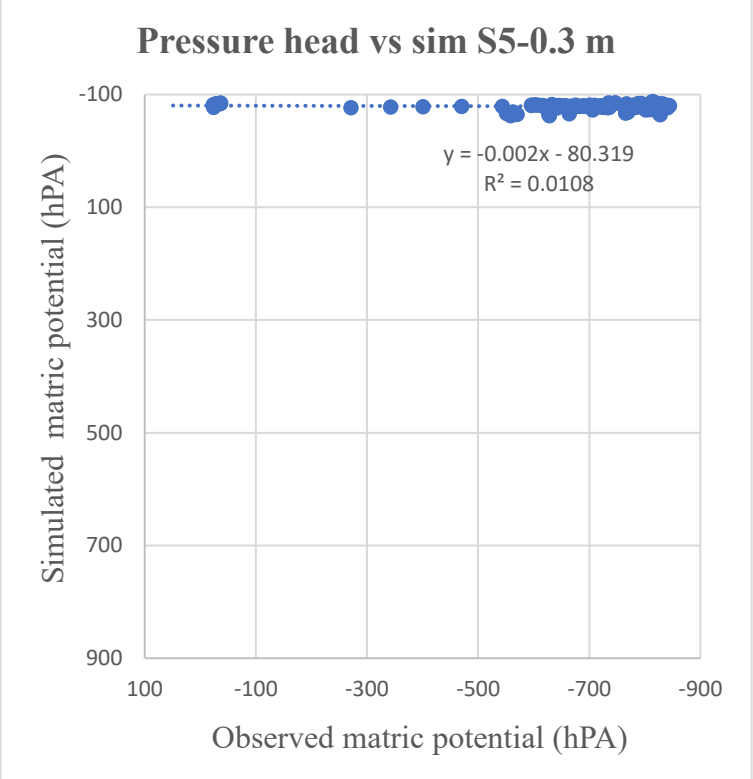

Figure 6.33: Simulated versus observed matric potential with trendline and equation for station S5 *at a depth of 0.*

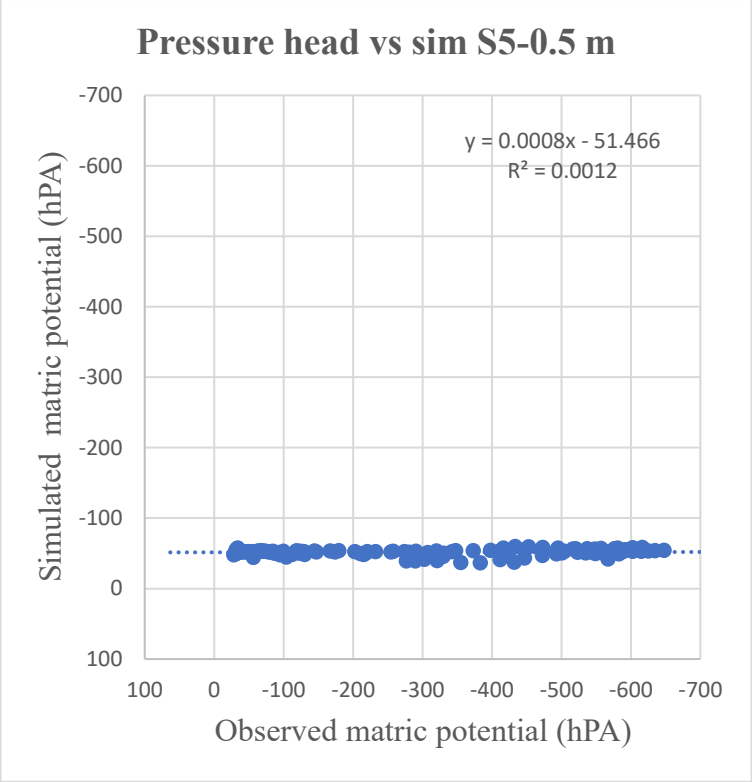

Figure 6.34: Simulated versus observed matric potential with trendline and equation for station S5 *at a depth of 0.3 m.*

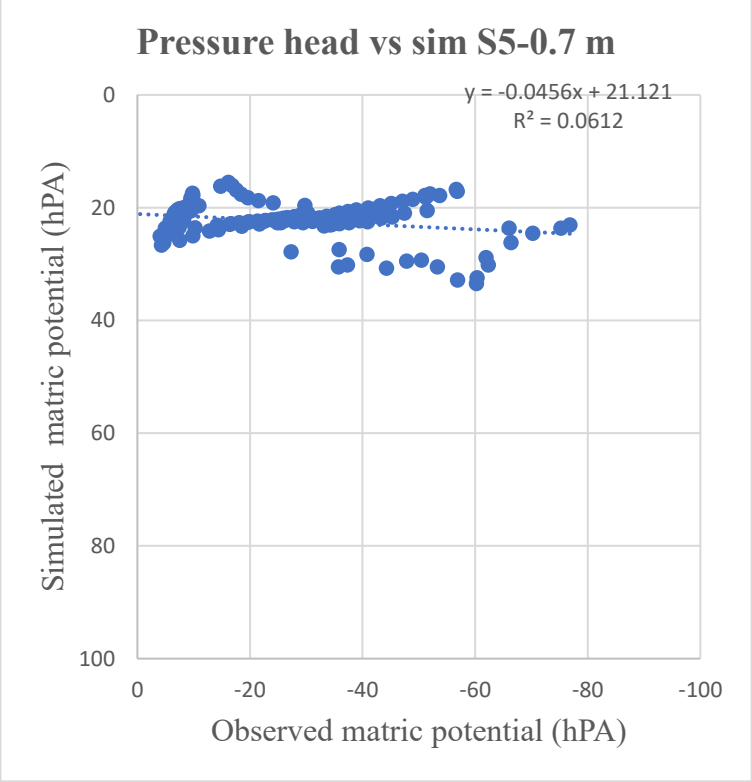

Figure 6.35: Simulated versus observed matric potential with trendline and equation for station S5 at a depth of 0.7 m.

The observed matric potential is determined by directly measuring the potential in the field using the tensiometers installed at the five-monitoring location. On the other hand, the simulated matric potential is calculated using a simulation model that considers various factors such as soil properties, climatic data, and boundary conditions.

(In the Figures 6.21 to 6.35), the following graphs has a greater R value S1 at a depth of 0.5 m and 0.7 m, S3 at a depth 0.7 m, S4 at a depth of 0.5 m. So, at these points the model matches the observation values and improved alignment between two values (observed and simulated) are obtained. Whereas in the following graphs the R value is consecutively low, 0.3 m deep at station S1 (Figure 6.21), 0.5 m deep at station S2 (Figure 6.25), 0.3 m deep at station S4 (Figure 6.30) and 0.5 m deep at S5 (Figure 6.34).

In summary, the graph obtained from comparing simulated and observed matric potential provides an agreement between the two datasets offering the insights into the performance of the simulation model and enhances the understanding of matric potential behaviour in the soil.

6.3 Analyzing the temporal behaviour of simulated and observed moisture content.

Finally, the model output was compared with the temporal behaviour of the data acquired in the field (Figures 6.36 to 6.55). This visual compassion allows for the identification of temporal trends and fluctuation between the simulated and observed datasets. The graphs also incorporate evapotranspiration values, providing insights to the relationship between moisture content and evapotranspiration patterns.

Notice the mode response to the meteorological events. For example, (Figure 6.36) shows that peak in moisture content (up to 0.472) computed for S1at a depth of 0.1 m took place on 4th July 2021 because of 21.9 mm rainfall and then again, some increase in the moisture content was observed on 16th July (up to 0.456) because of 20 mm rainfall recorded.

(Figure 6.37) points out how the moisture content rises at 0.3 m depth in station S1 on July 4, 16 and 27 when significant precipitation events occurred at a depth of 0.5 m (Figure 6.38), the variation is smaller and at a depth of 0.7 m the soil is almost saturated with null changes (Figure 6.39). The layers in which the model is capable of capturing the observation dynamics are (station S1 at a depth of 0.5 m, station S2 at a depth of 0.5 m, station S3 at a depth of 0.1 m, station S4 at a depth of 0.1 m and 0.3 m). Some interesting characteristics of station S4 and S5 at a depth of 0.5 m (Figure 6.50 and 6.54) are that the moisture content reaches up to 0.6 and in S4 station it crosses 0.6. Although the moisture dynamics over time is quite well captured by the model, the simulation overestimates the water content in the shallower layers (0.1 and 0.3 m deep), possibly indicating a bias in the evaluation of θ_s based on the textural information only.

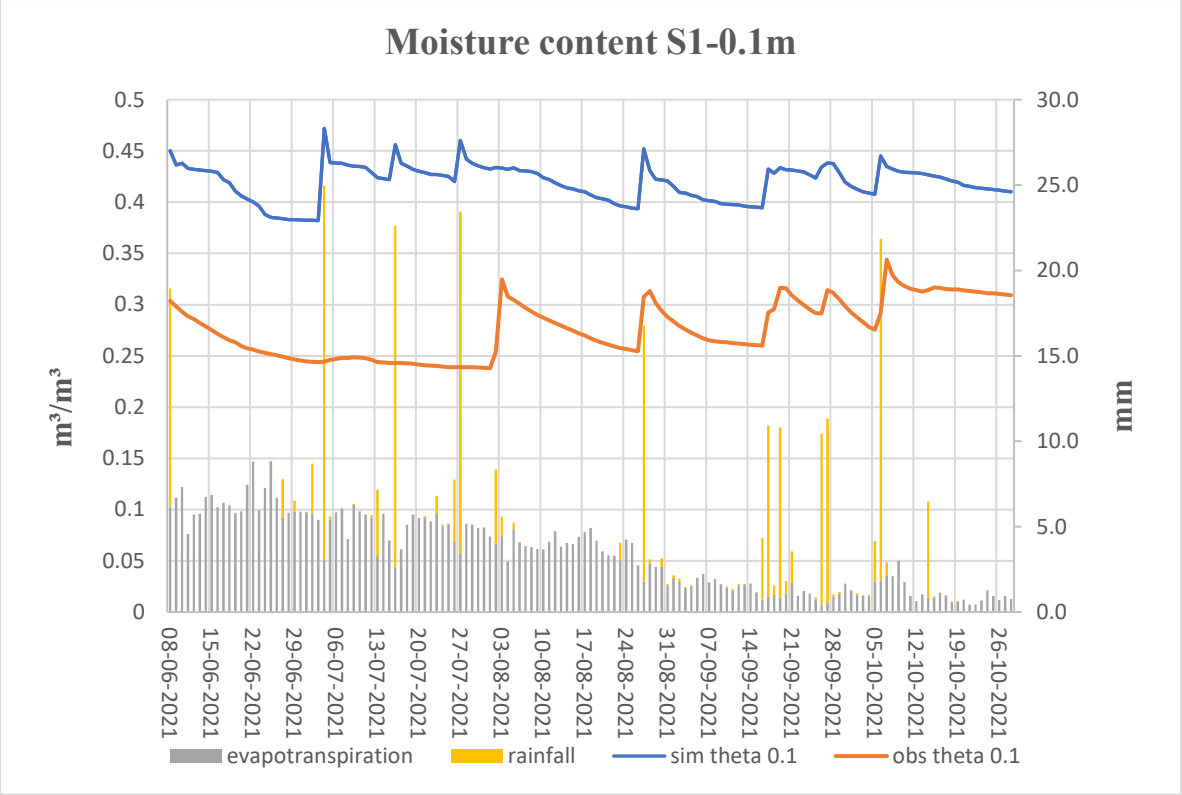

Figure 6.36: Simulated and measured moisture content versus time for station S1 at a depth of 0.1 m.

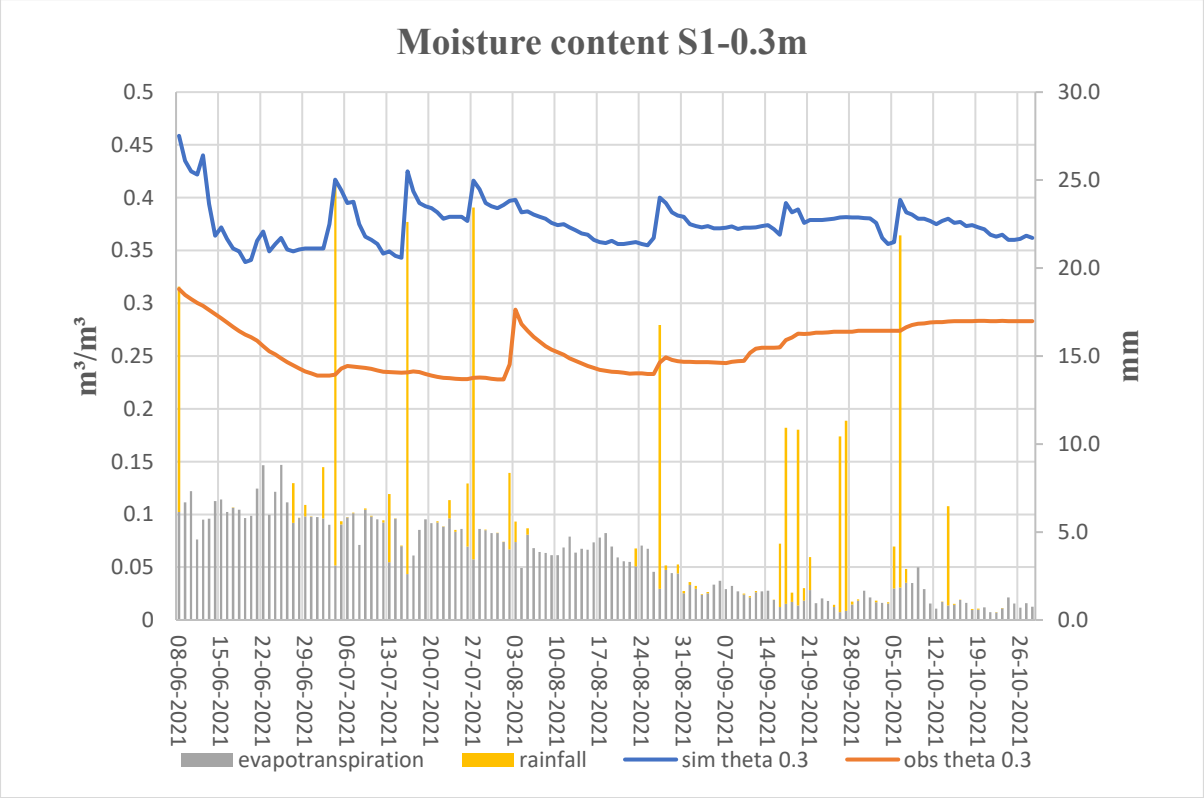

Figure 6.37: Simulated and *measured moisture content* versus time *for station* S*1 at a depth of 0.3 m.*

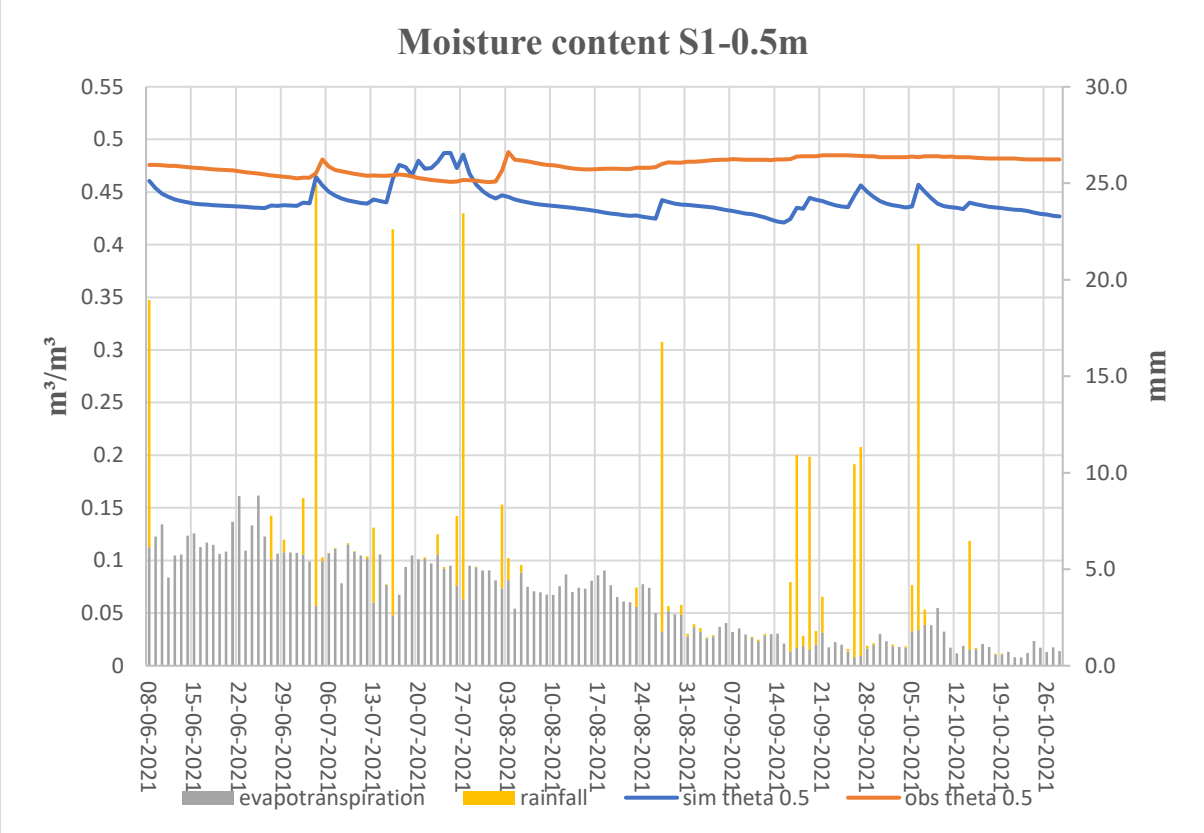

Figure 6.38: Simulated and measured moisture content versus time *for station* S1 *at a depth of 0.5 m.*

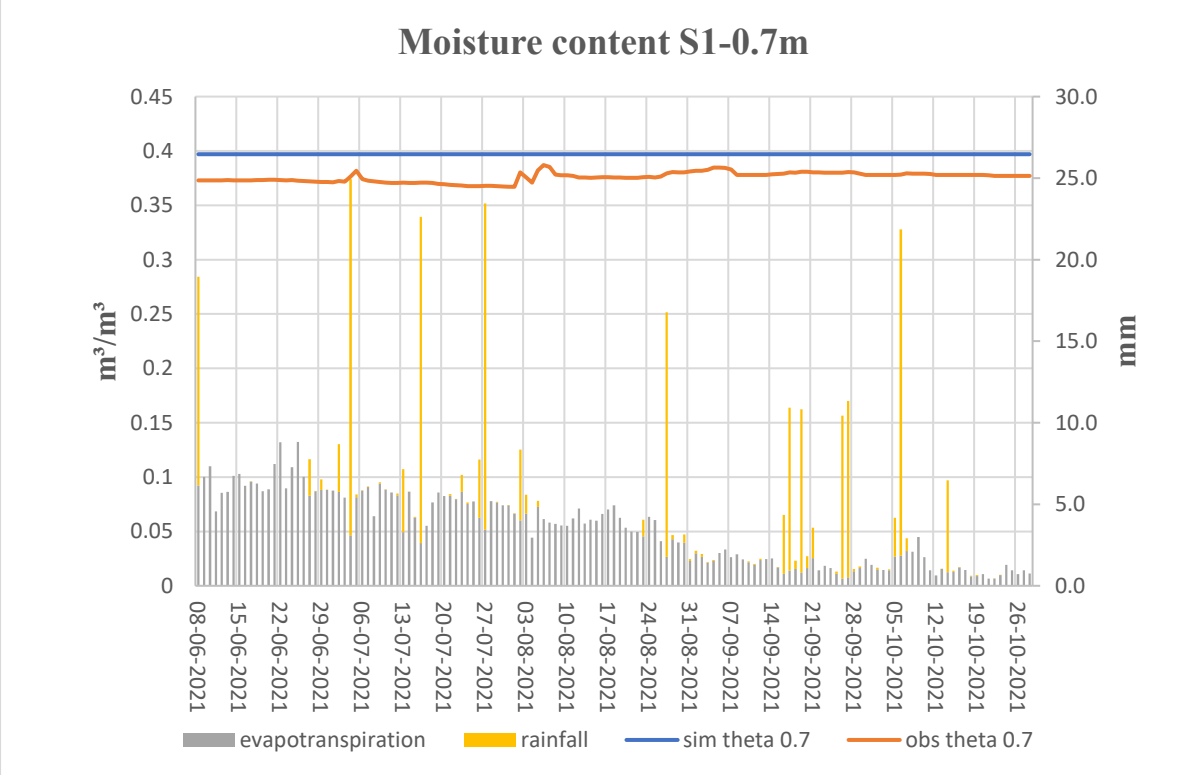

Figure 6.39: Simulated and measured moisture content versus time *for station* S1 *at a depth of 0.7*

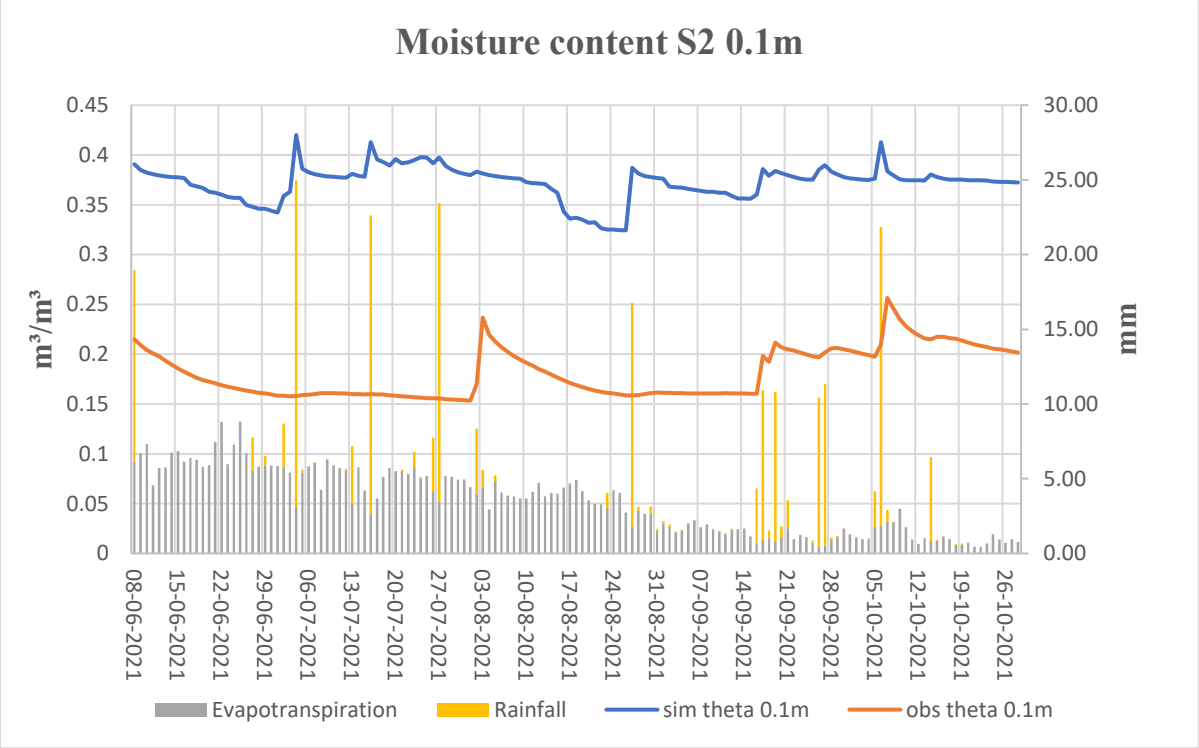

Figure 6.40: Simulated and measured moisture content versus time *for station* S2 *at a depth of* 0.1 *m.*

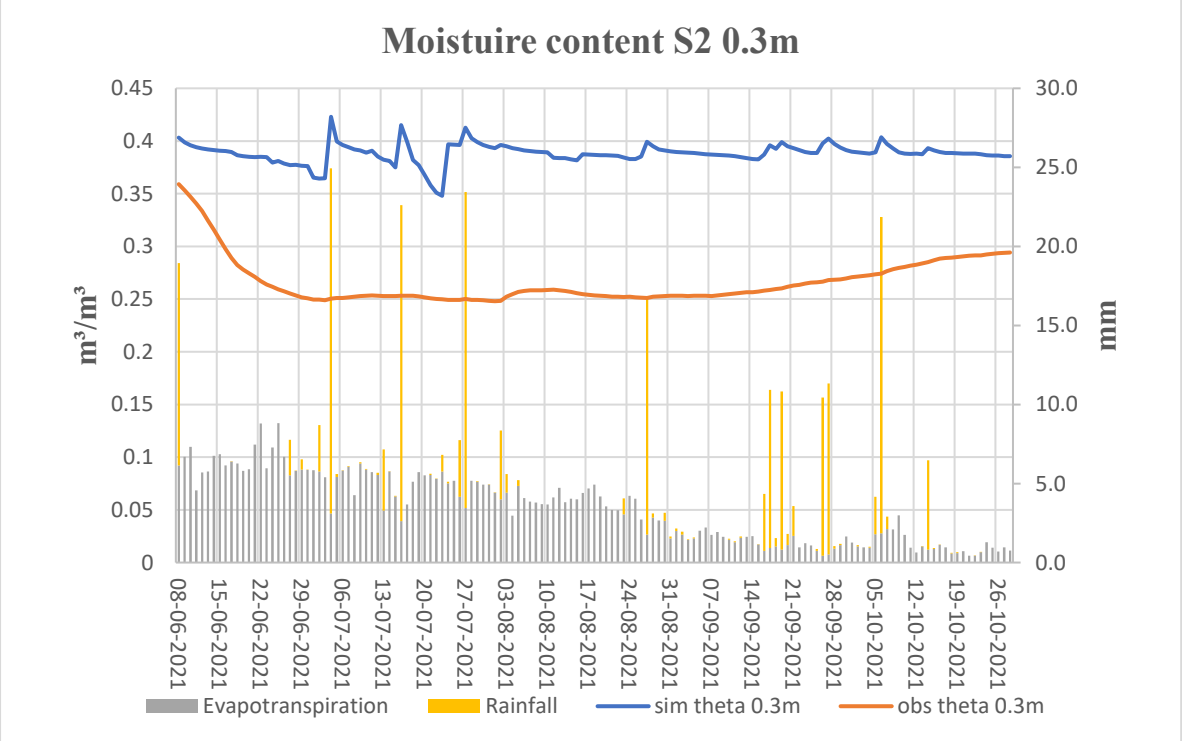

Figure 6.41: Simulated and measured moisture content versus time *for station* S2 *at a depth of* 0.3 *m.*

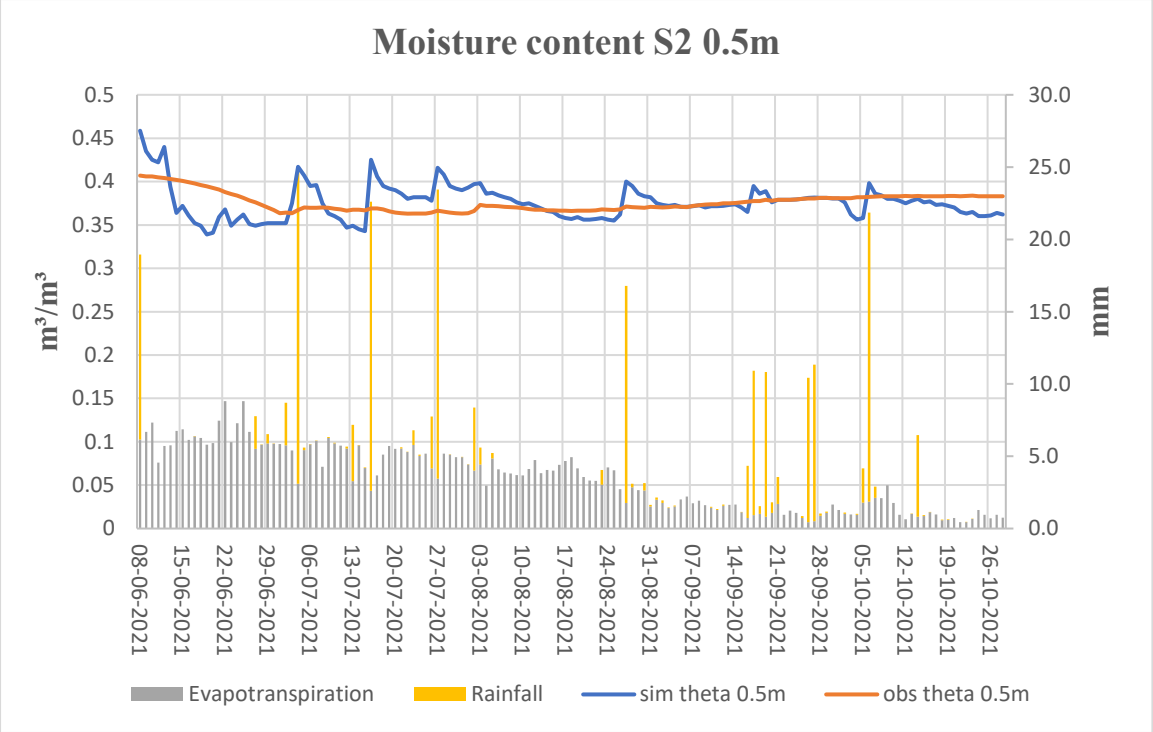

Figure 6.42: Simulated and measured moisture content versus time *for station* S2 *at a depth of 0.5 m.*

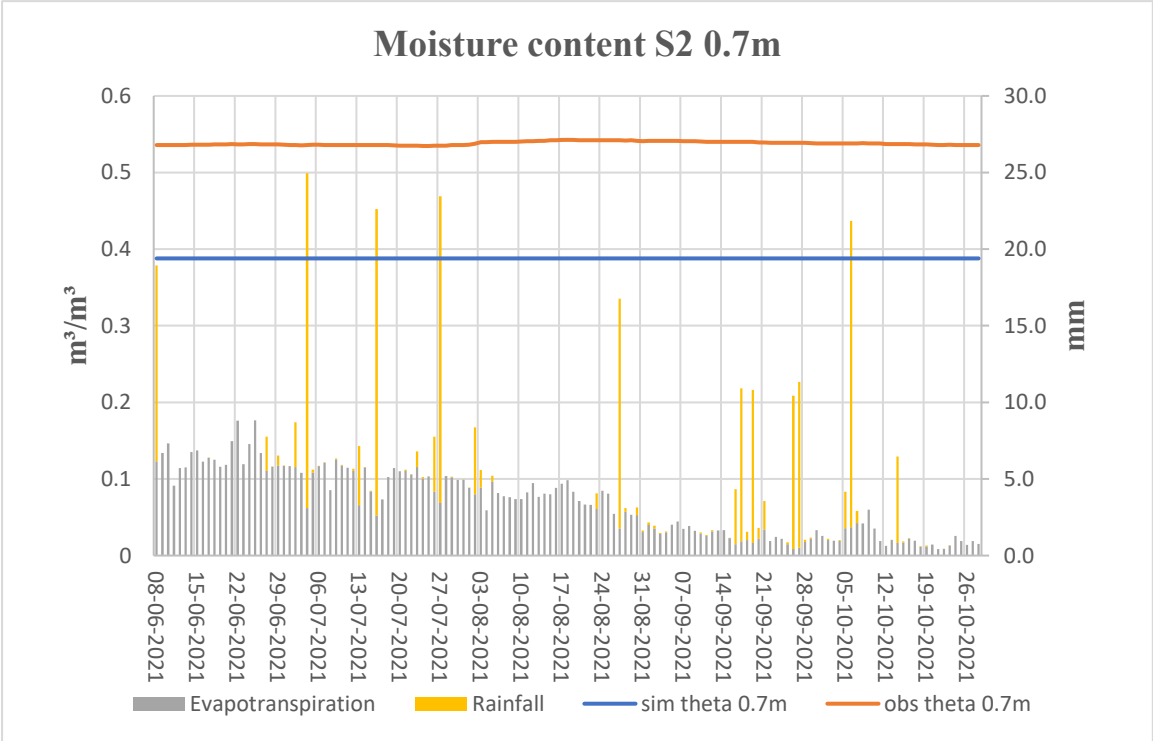

Figure 6.43: Simulated and measured moisture content versus time *for station* S2 *at a depth of 0.7 m*

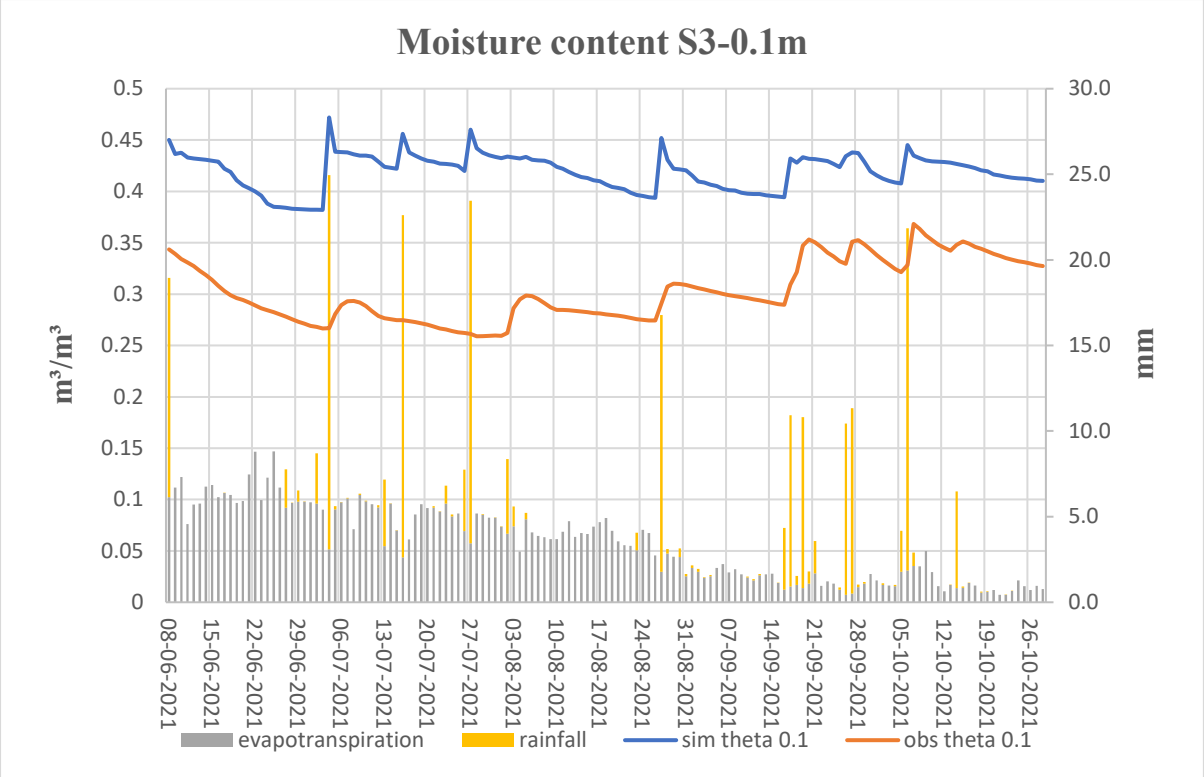

Figure 6.44: Simulated and measured moisture content versus time *for station* S3 *at a depth of* 0.1 *m.*

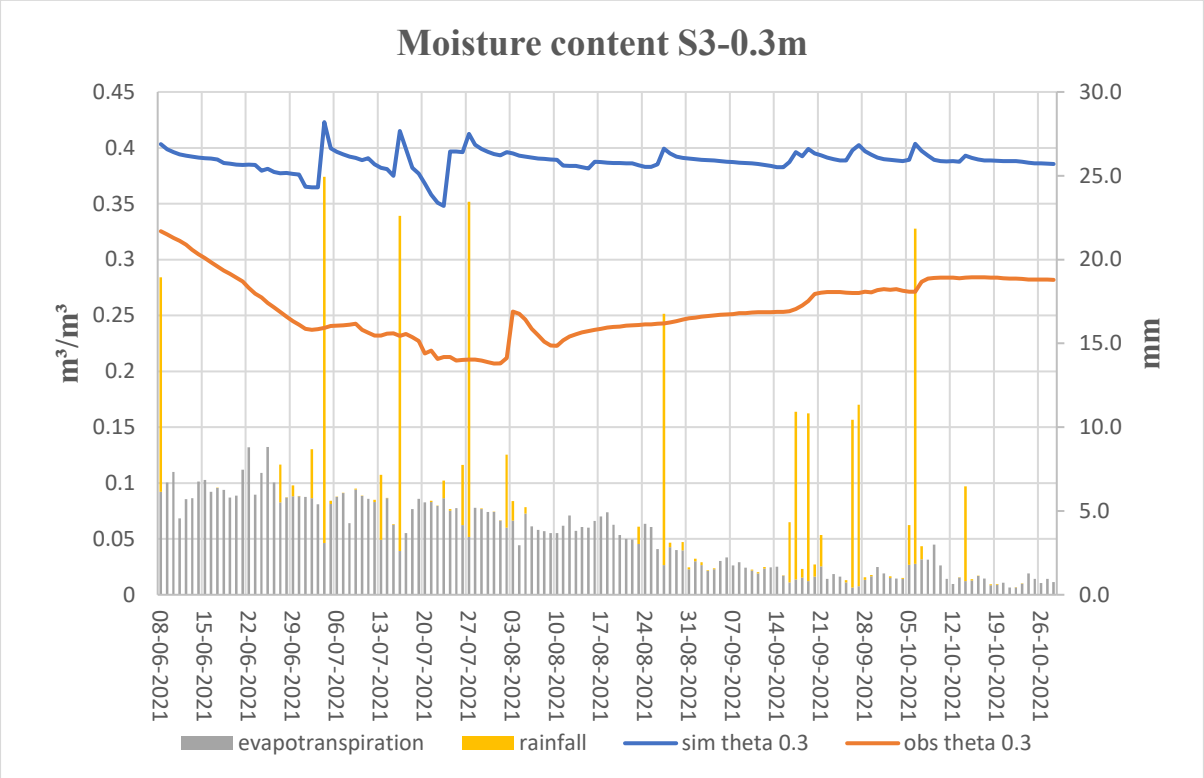

Figure 6.45: Simulated and measured moisture content versus time *for station* S3 *at a depth of* 0.3 *m.*

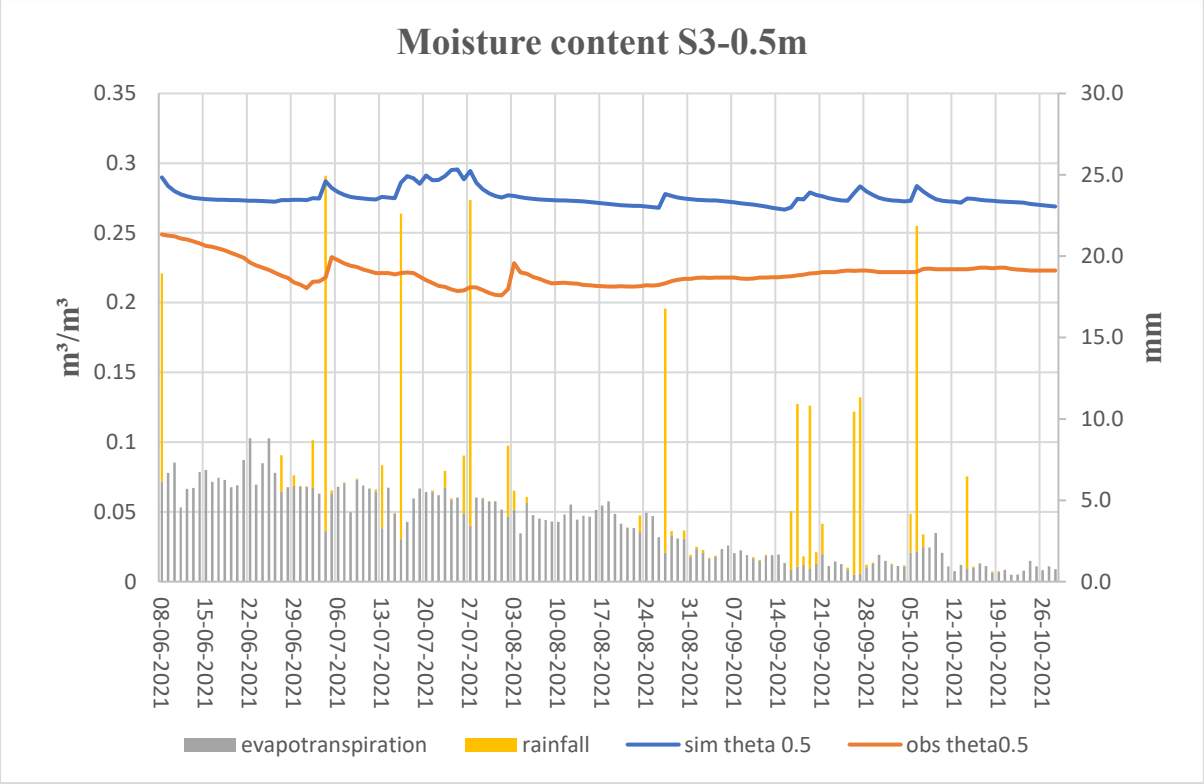

Figure 6.46: Simulated and measured moisture content versus time *for station* S3 *at a depth of 0.5 m.*

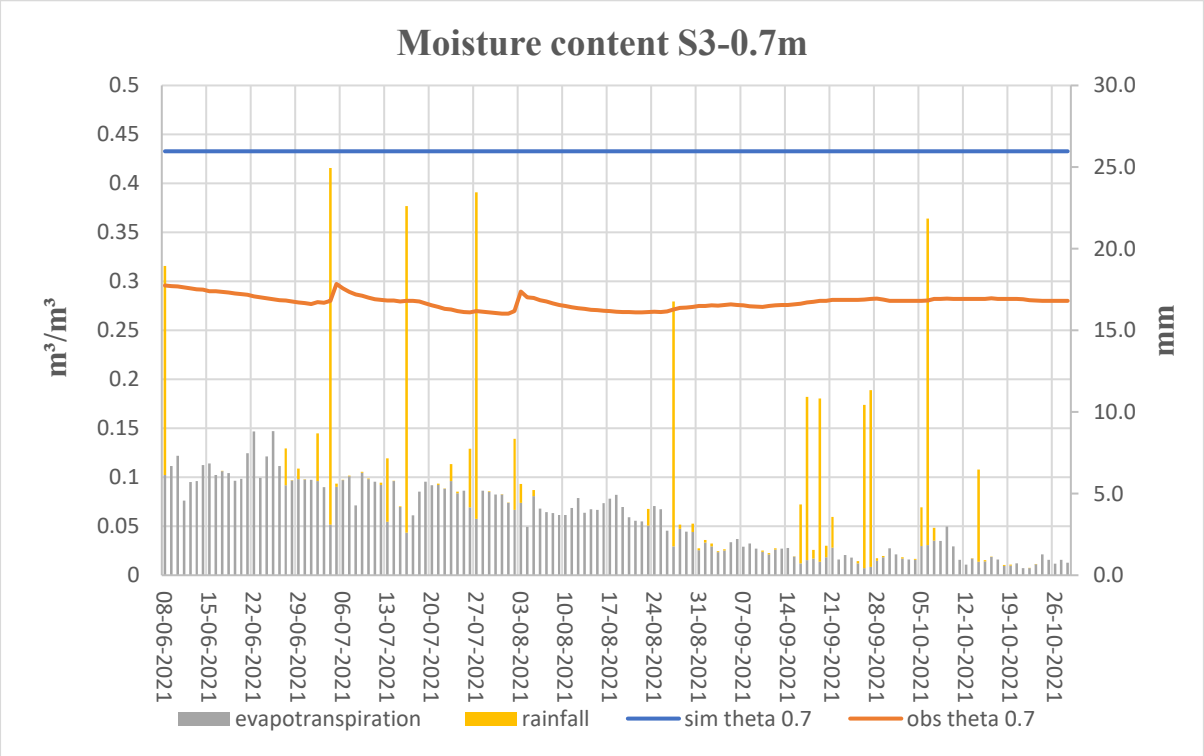

Figure 6.47: Simulated and measured moisture content versus time *for station* S3 *at a depth of 0.7 m.*

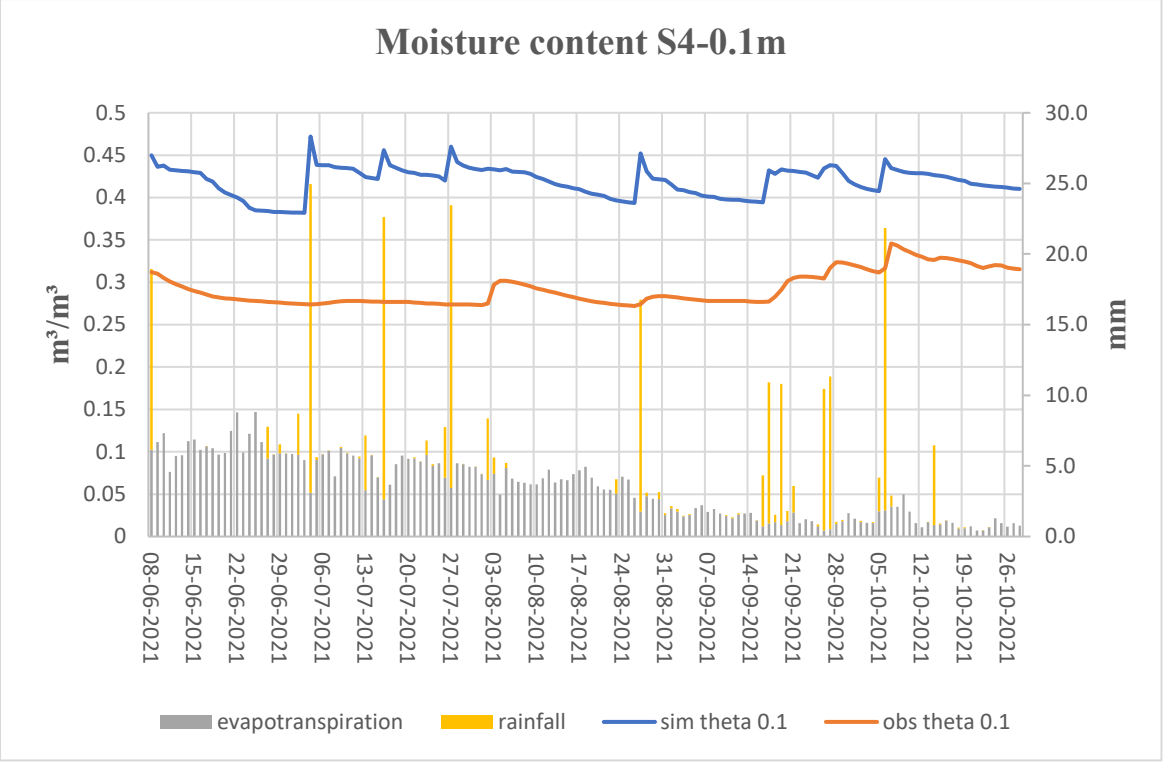

Figure 6.48: Simulated and measured moisture content versus time *for station* S4 *at a depth of 0.*1 *m.*

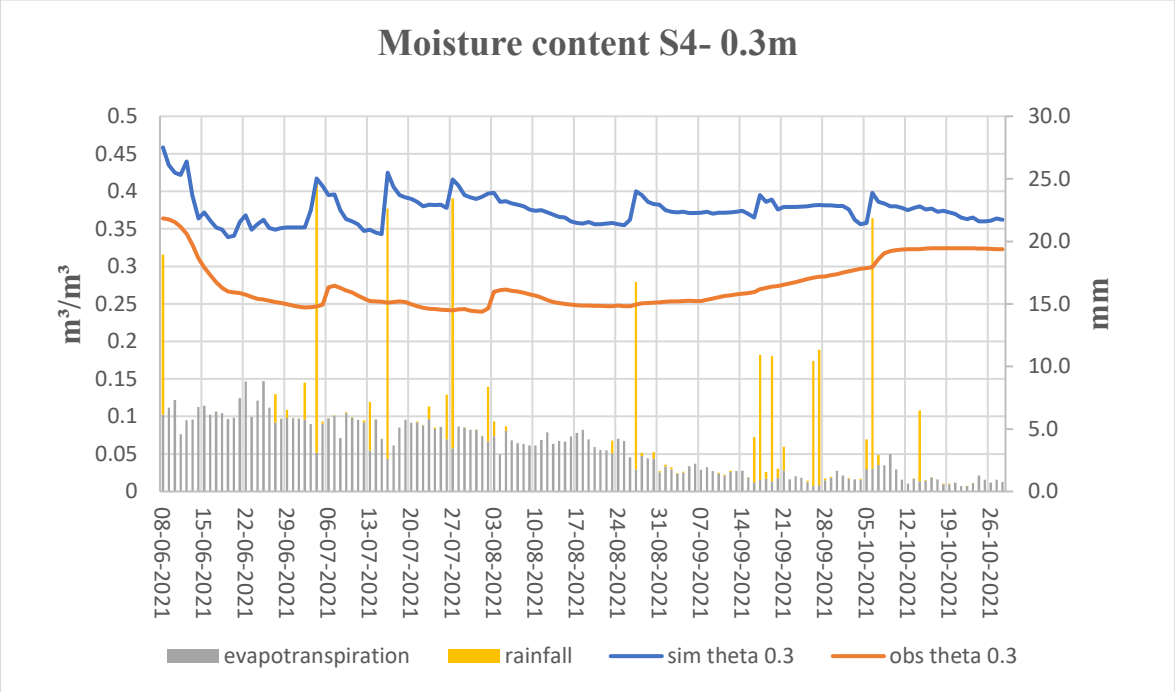

Figure 6.49: Simulated and measured moisture content versus time *for station* S4 *at a depth of 0.*3 *m.*

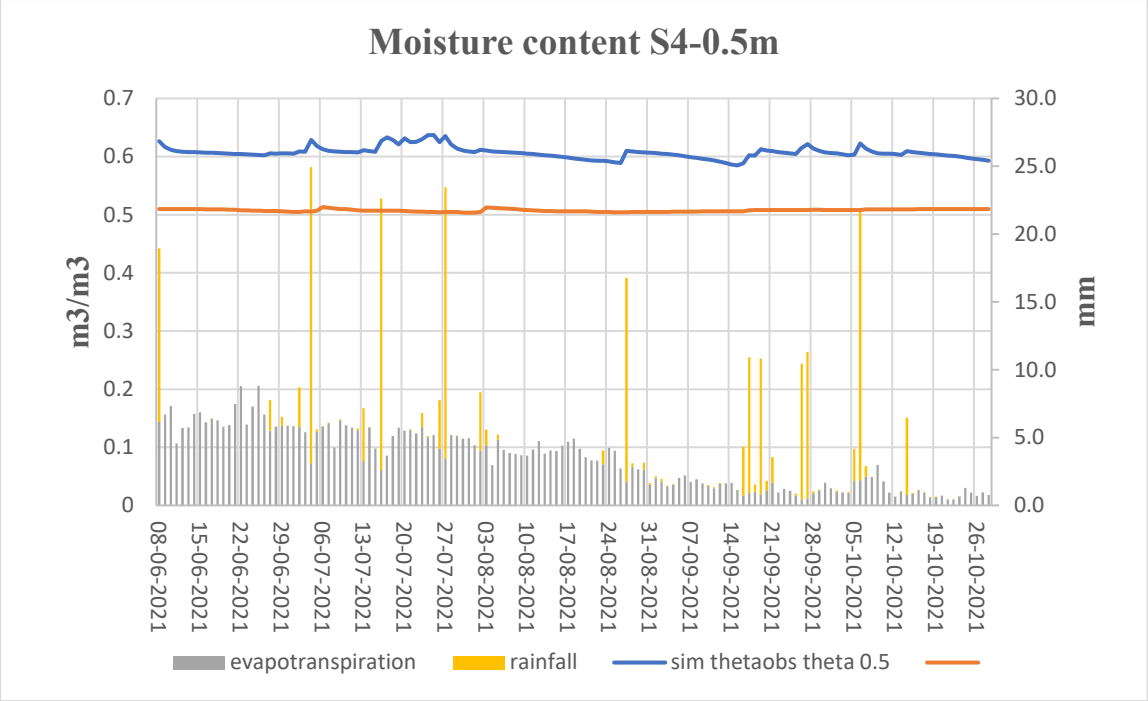

Figure 6.50: Simulated and measured moisture content versus time *for station* S4 *at a depth of 0.5 m.*

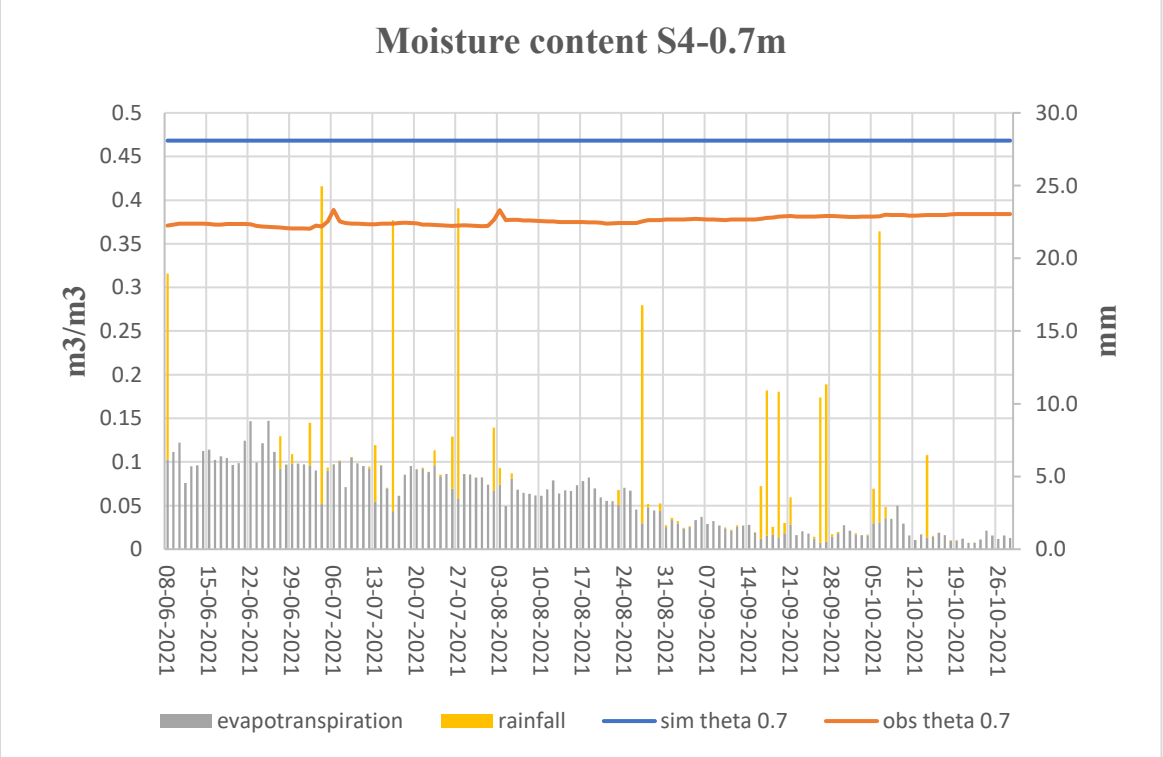

Figure 6.51: Simulated and measured moisture content versus time *for station* S4 *at a depth of 0.7 m.*

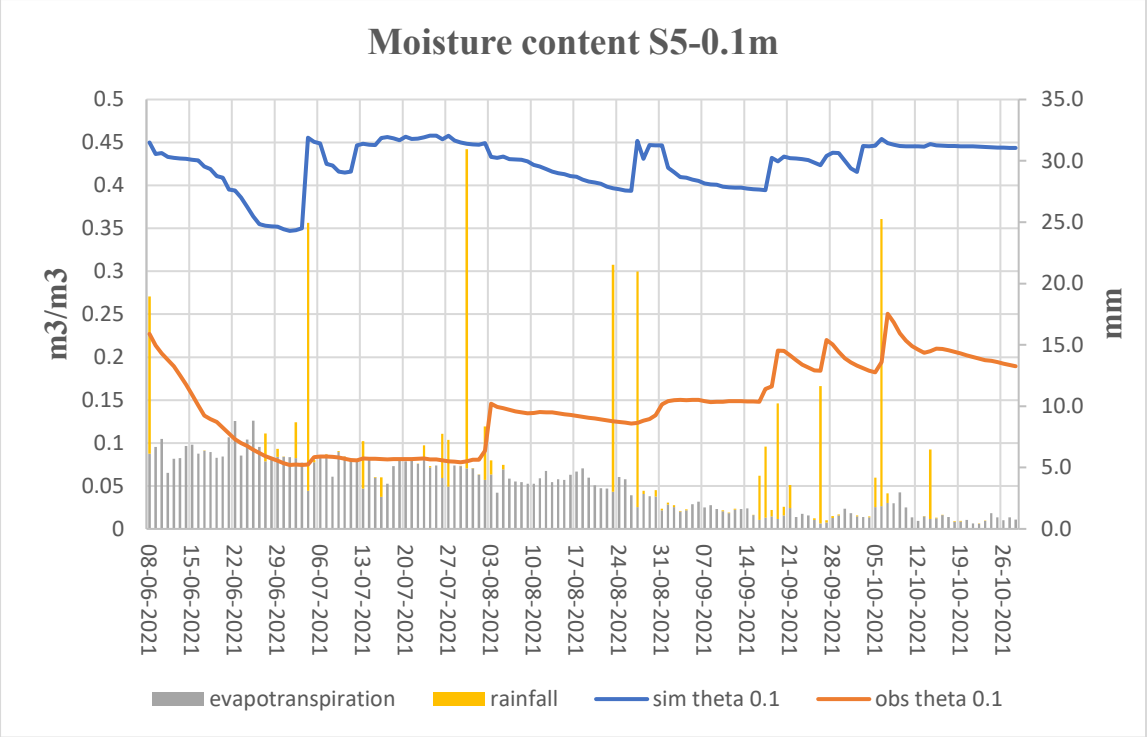

Figure 6.52: Simulated and measured moisture content versus time *for station* S5 *at a depth of 0.*1 *m.*

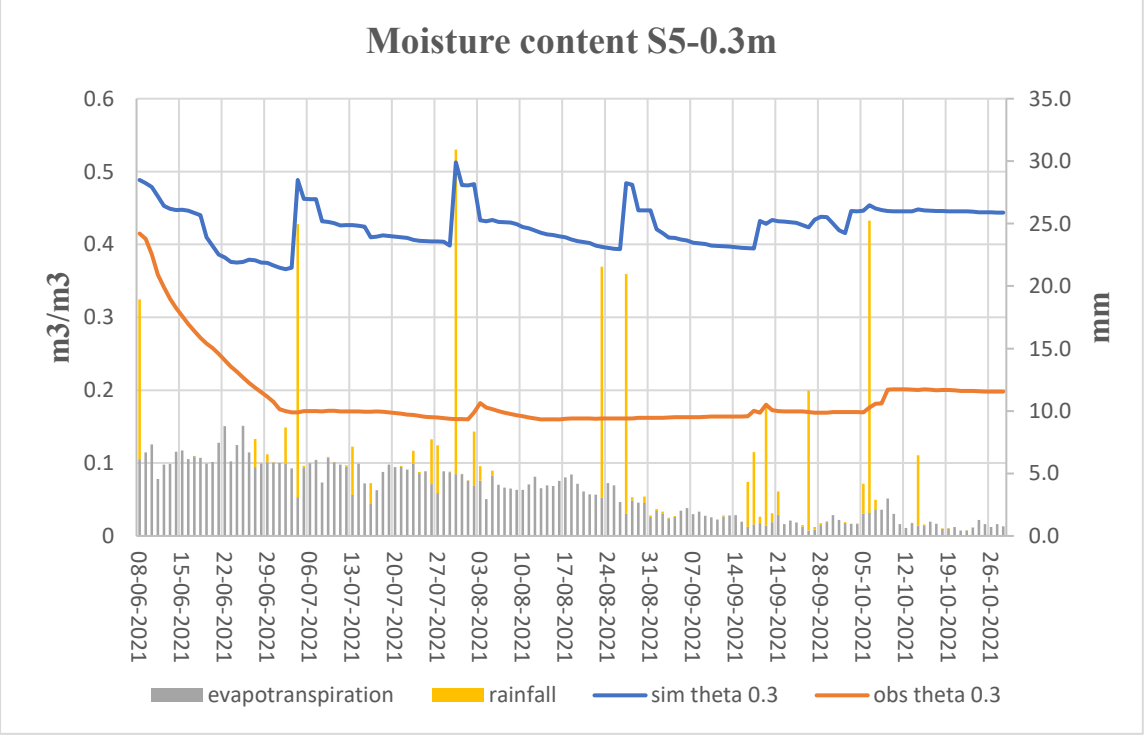

Figure 6.53: Simulated and measured moisture content versus time *for station* S5 *at a depth of 0.*3 *m.*

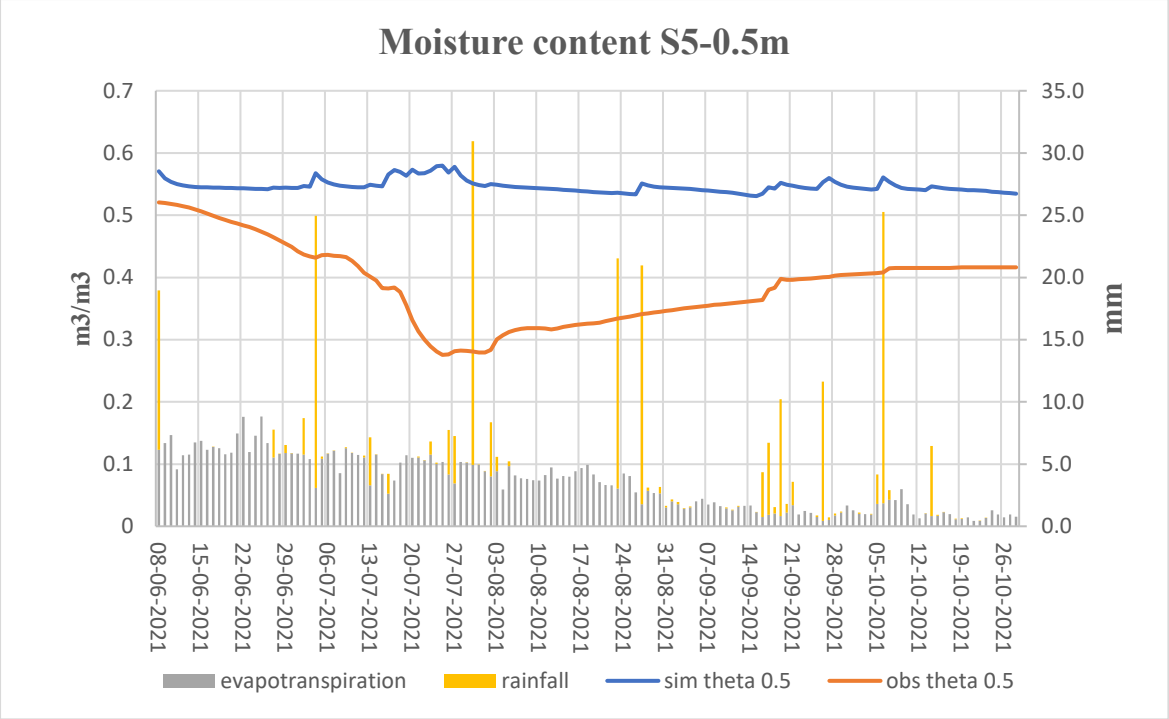

Figure 6.54: Simulated and measured moisture content versus time *for station* S5 *at a depth of 0.5 m.*

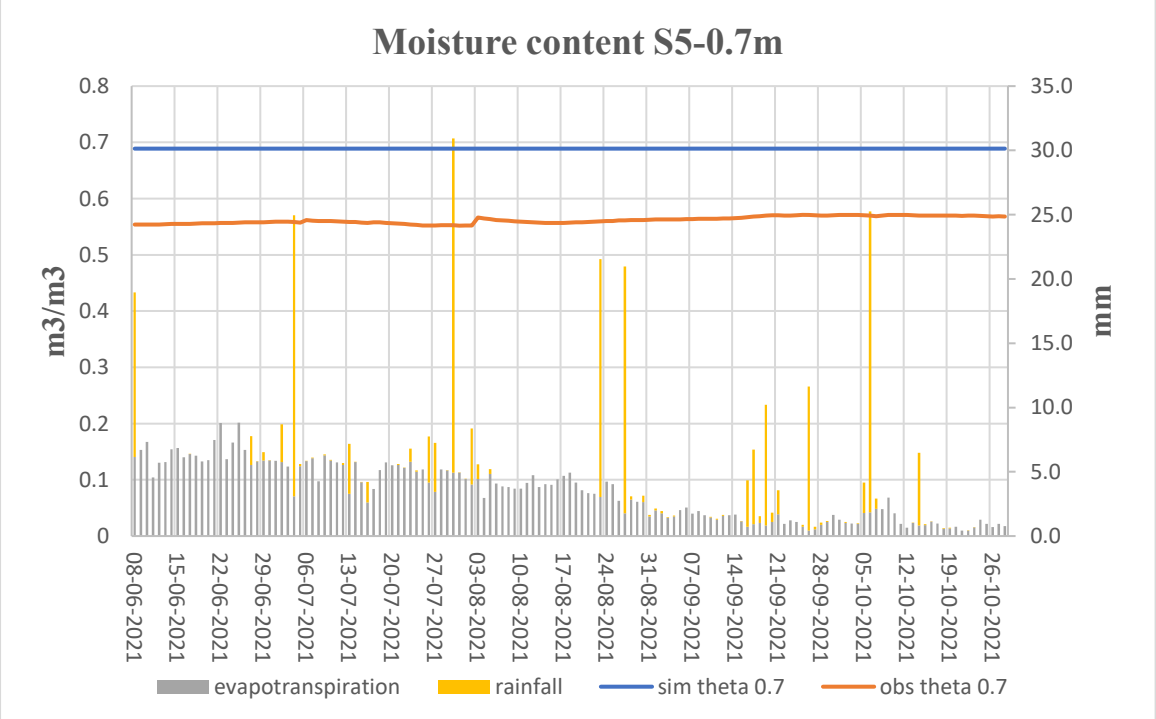

Figure 6.55: Simulated and measured moisture content versus time *for station* S5 *at a depth of 0.7 m.*

6.4 Analyzing the temporal patterns of simulated and observed capillary rise in relation to evaporation.

Soil matric potential refers to the energy status of the water in the soil and reflects the force needed to extract water from the soil matrix. This is influenced by various factors such as soil structure, texture, existing soil moisture, precipitation which includes rainfall and other forms of moisture.

(Figures 6.56 to 6.70) provide the behaviour versus time of the measured and observed pressure head. The figures point out that the effect of precipitation on the soil matric potential is significant, at the time of precipitation water infiltrates the soil reducing the soil matric potential or the capillary pressure. The frequency and timing of the precipitation events has a big contribution to the capillary pressure, for example regular rainfall events helps to maintain a high soil moisture level resulting in a lower soil matric potential, conversely prolonged time without rainfall causes to reduce the soil moisture, leading to a high capillary pressure.

The simulated values were able to capture the observation dynamics at the following stations with its respective layers, station S1 at a depth of 0.3m (Figure 6.56), station S2 at a depth of 0.5 m (Figure 6.60), station S3 at a depth of 0.5 m (Figure 6.63) and station S4 at a depth of 0.5 m (Figure 6.66). Moreover, it was noted that in all the stations specifically the layer at 0.7 m the pressure head values were positive which indicates that the layer is saturated, while the value in rest of the layers for all the stations are negative. While the simulated pressure head value for stations S1, S2, S3, S5 in its 0.3 m depth reaches up to -100, whereas simulated value for station S4 (Figure 6.65) stays between -60 to -90 initially. In some cases, the model also fails to mimic the observation correctly for example in station S2 at a depth of 0.3 m (Figure 6.59), also in station S3 and S5 at a depth of 0.3 m (Figure 6.63 and 6.68).

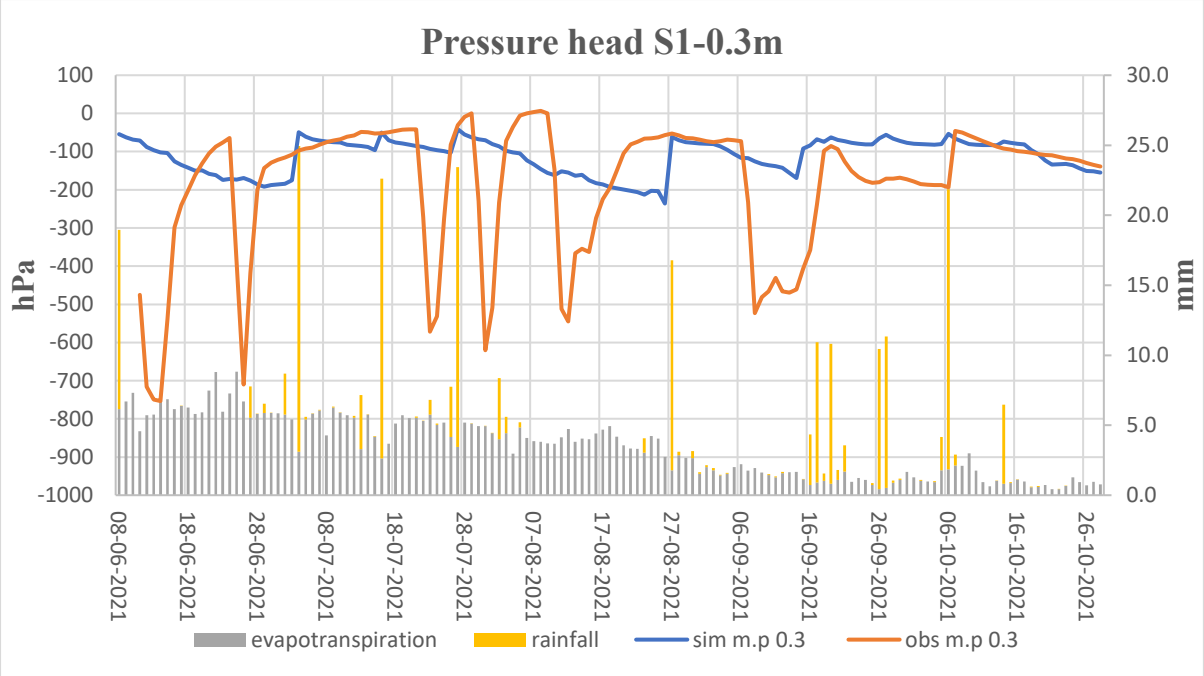

Figure 6.56: Simulated and measured pressure head *for station* S*1 at a depth of 0*.3 *m.*

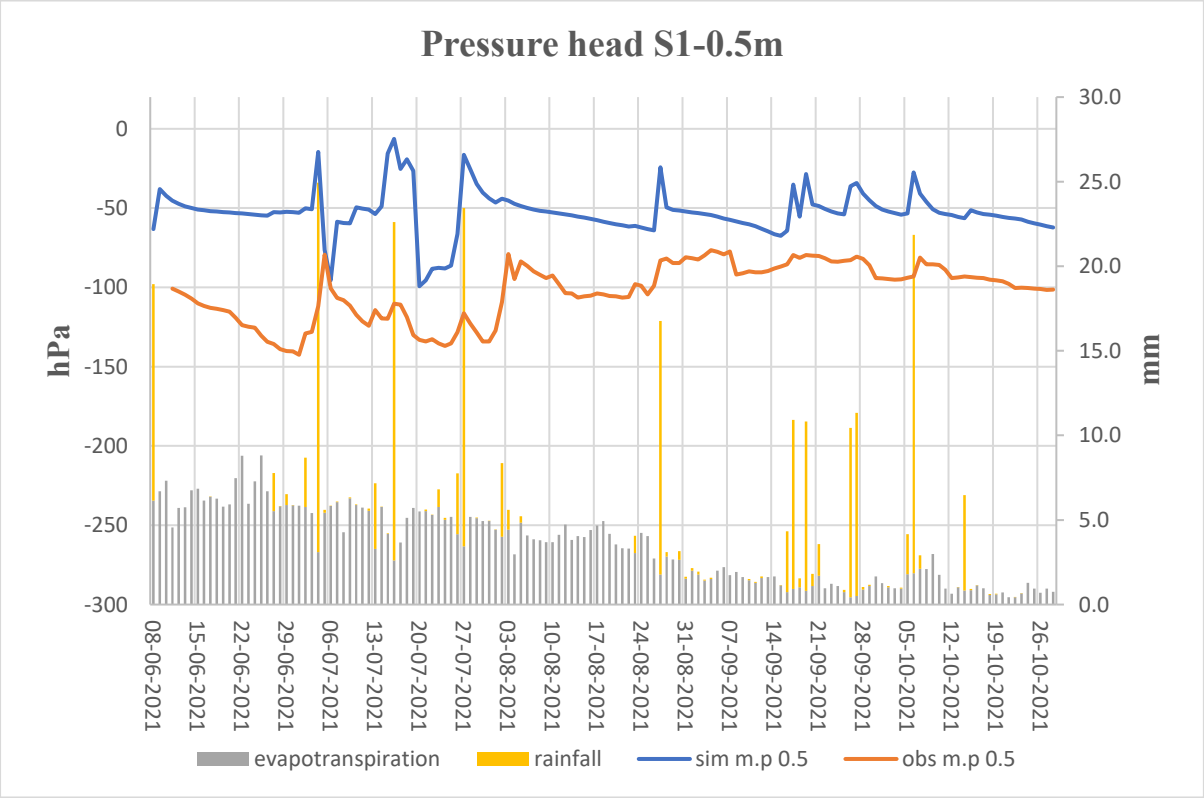

Figure 6.57: Simulated and measured pressure head *for station* S*1 at a depth of 0*.5 *m.*

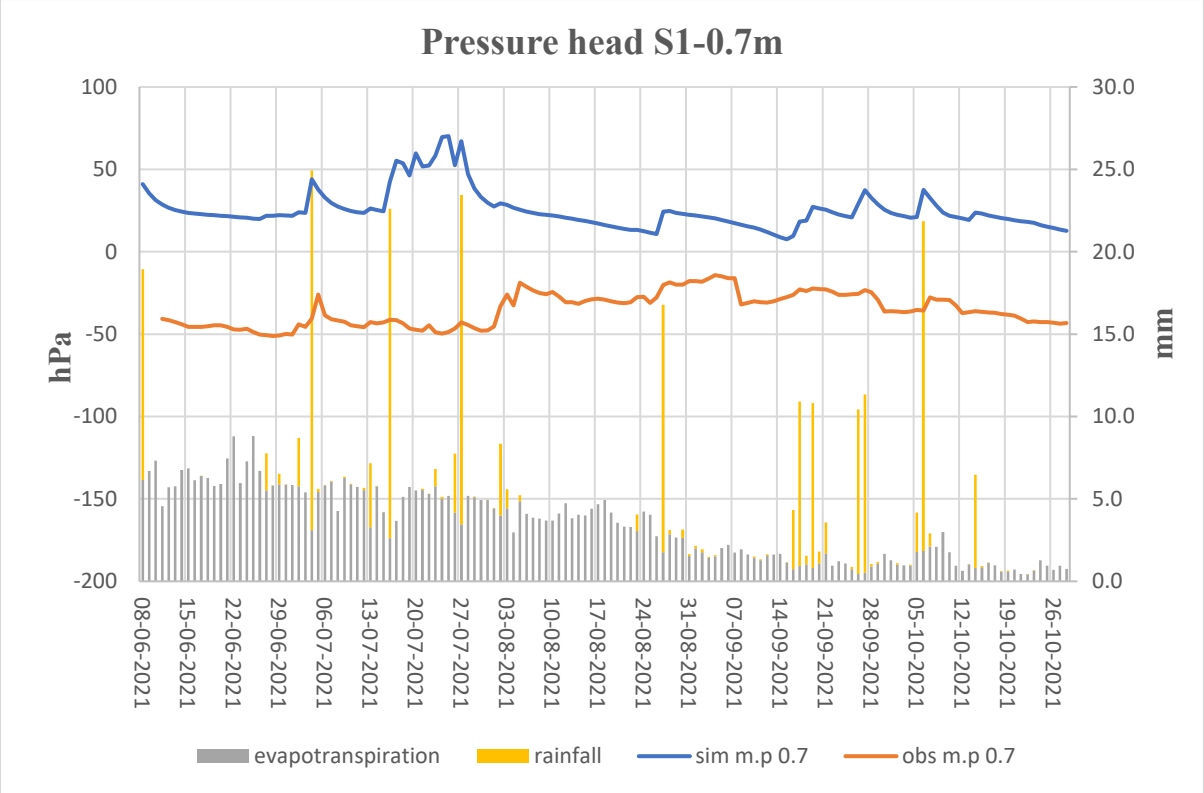

Figure 6.58: Simulated and measured pressure head *for station* S1 *at a depth of 0.7 m.*

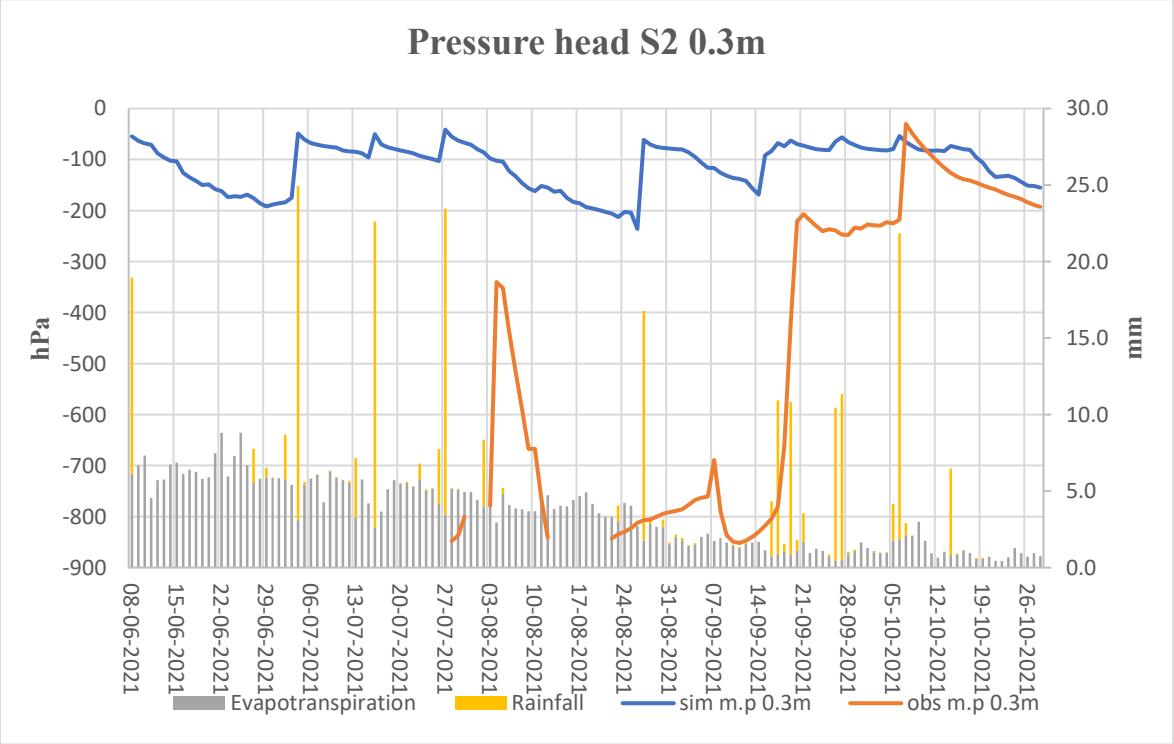

Figure 6.59: Simulated and measured pressure head *for station* S2 *at a depth of 0.3 m.*

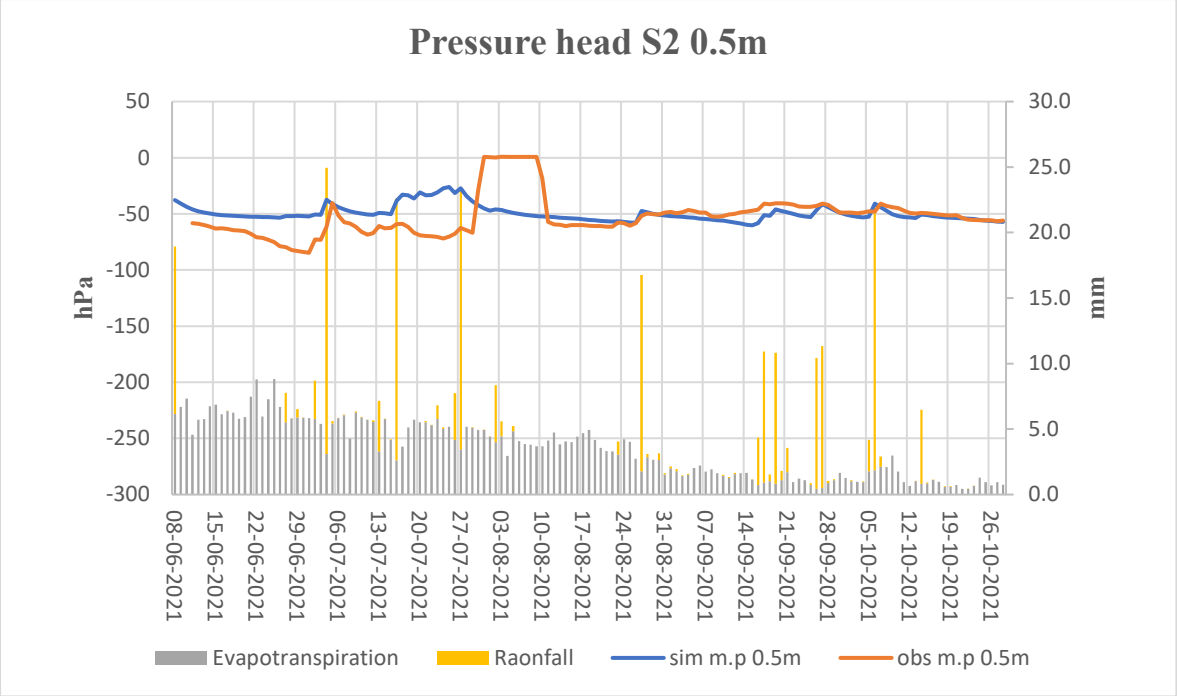

Figure 6.60: Simulated and measured pressure head *for station* S2 *at a depth of 0.5 m.*

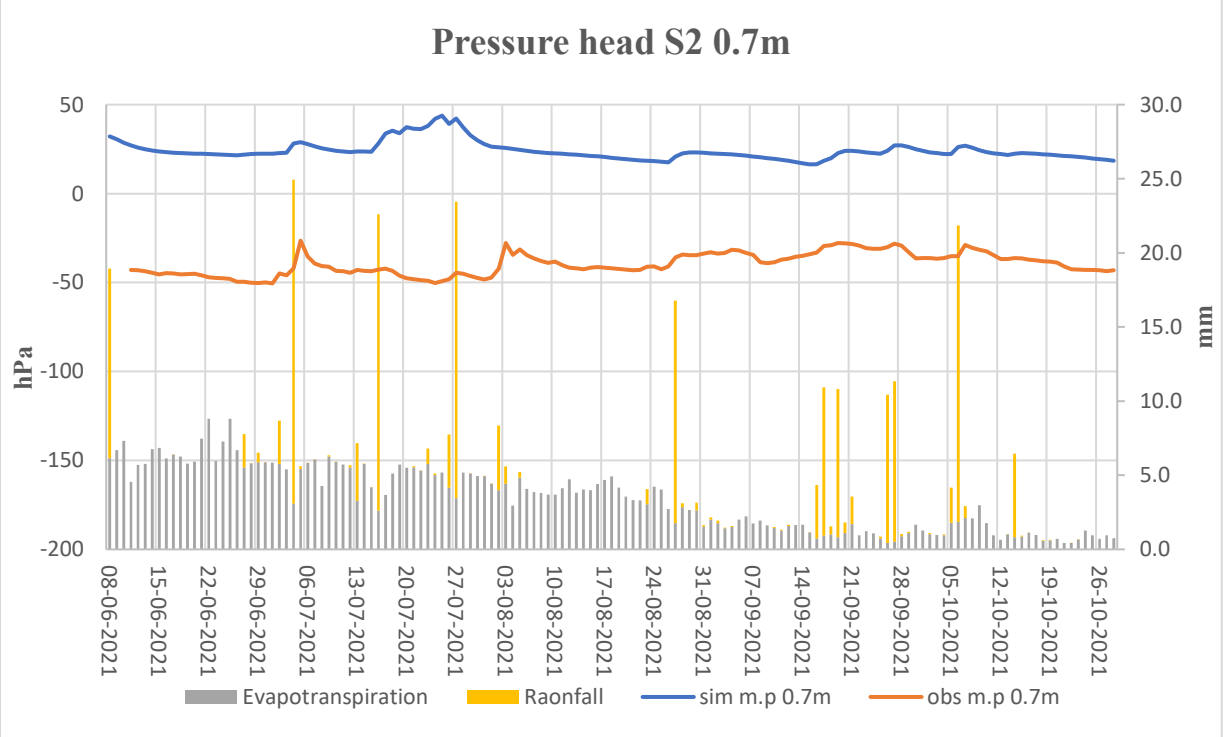

Figure 6.61: Simulated and measured pressure head *for station* S2 *at a depth of 0.7 m.*

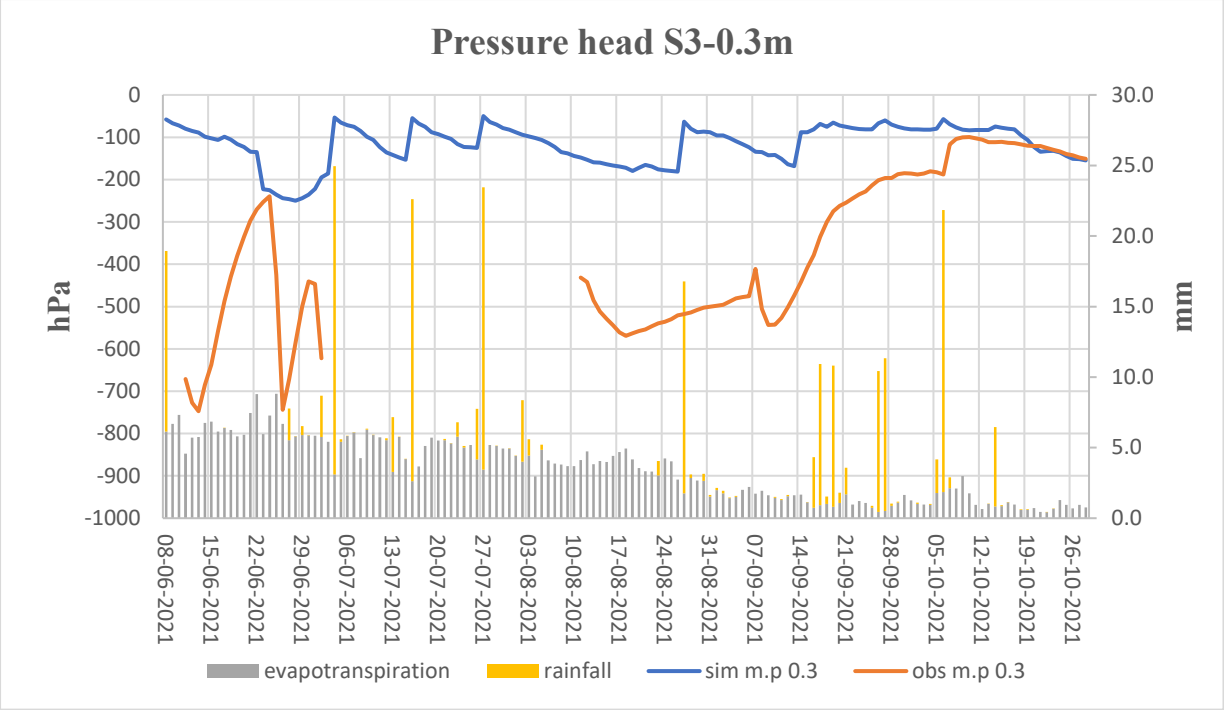

Figure 6.62: Simulated and measured pressure head *for station* S3 *at a depth of 0.3 m.*

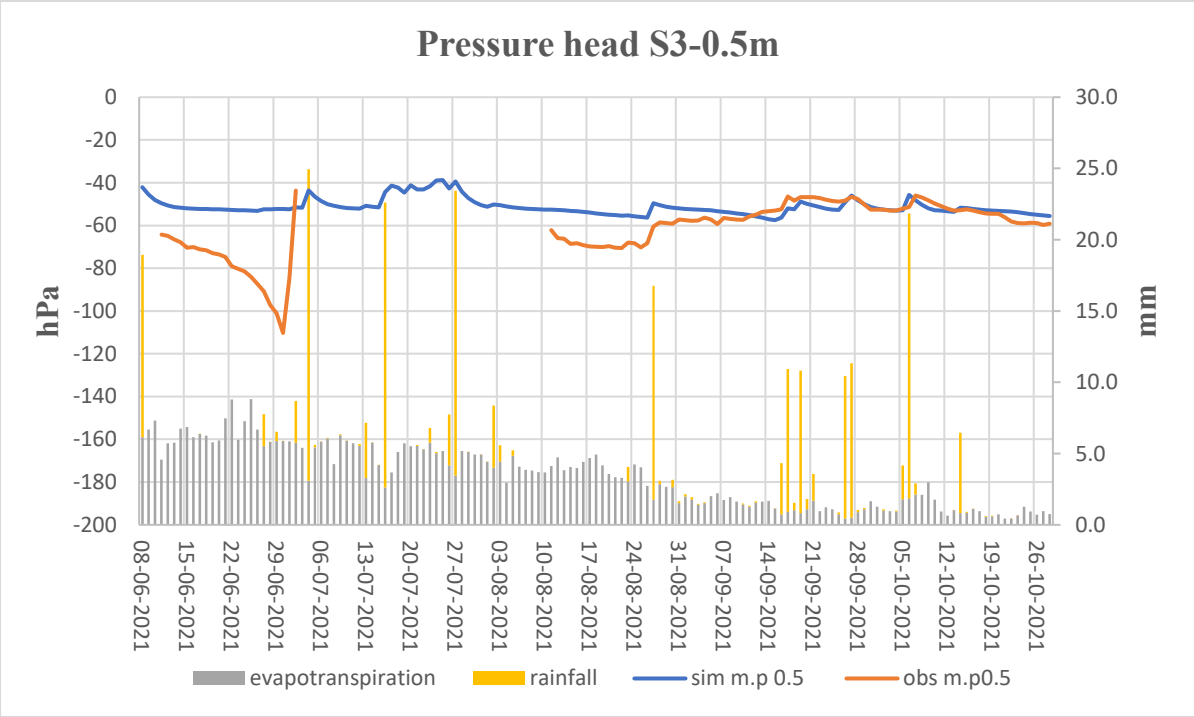

Figure 6.63: Simulated and measured pressure head *for station* S3 *at a depth of 0.5 m.*

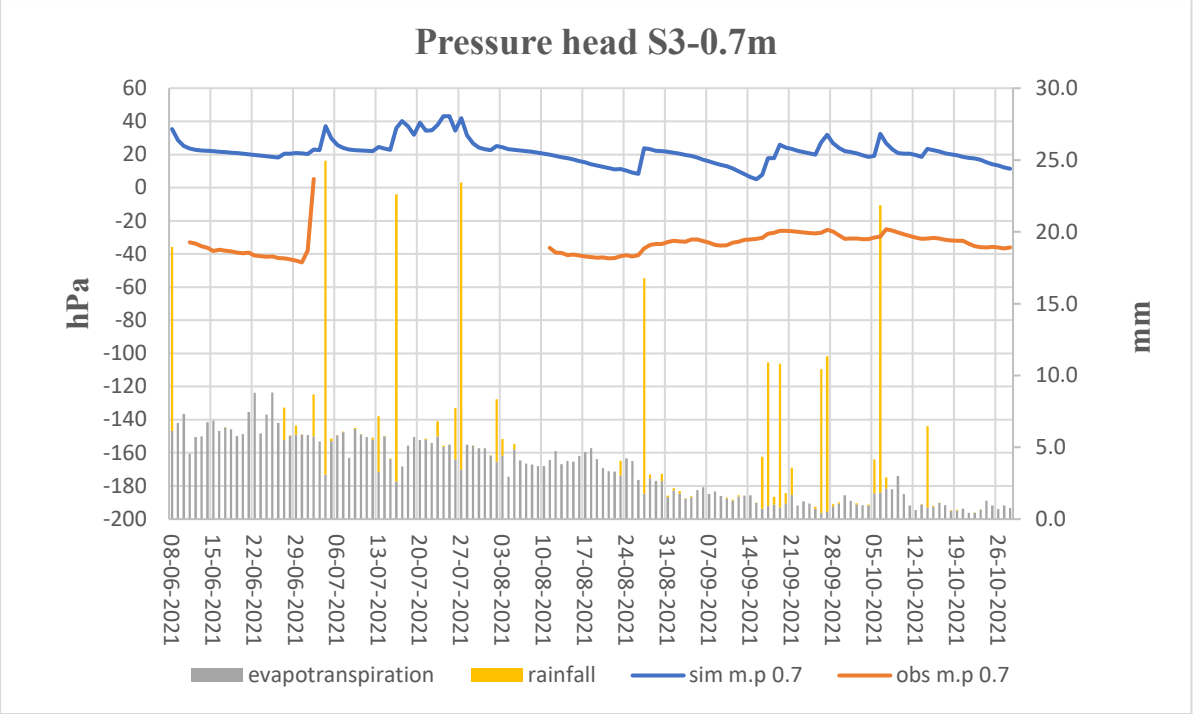

Figure 6.64: Simulated and measured pressure head *for station* S3 *at a depth of 0.7 m.*

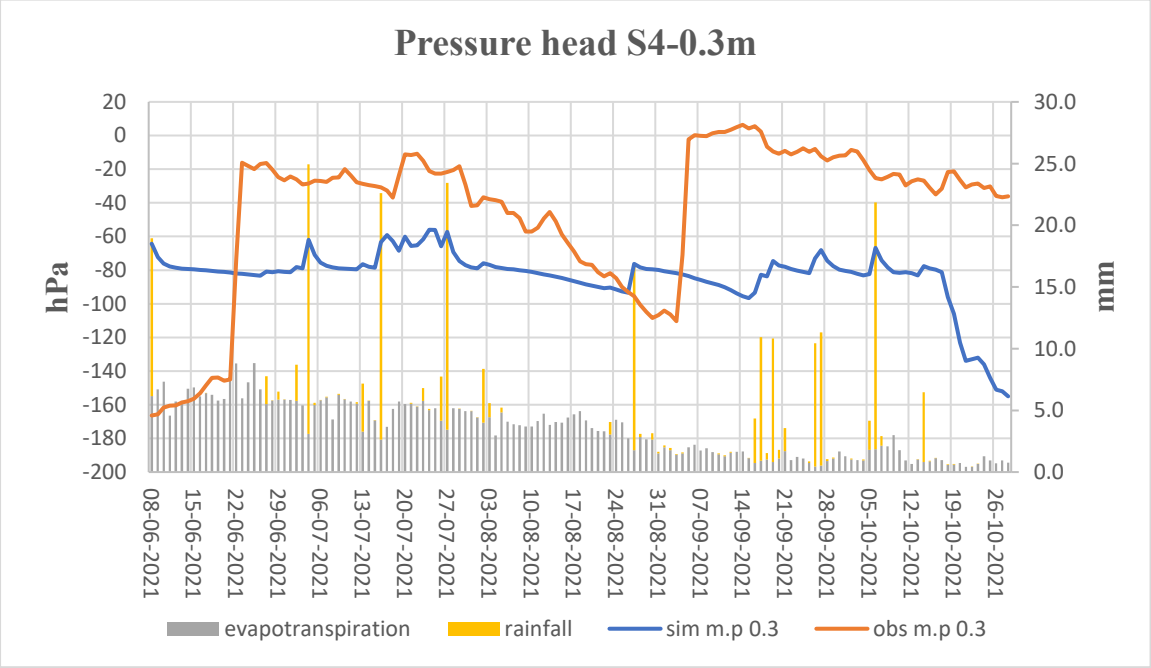

Figure 6.65: Simulated and measured pressure head *for station* S4 *at a depth of 0.3 m.*

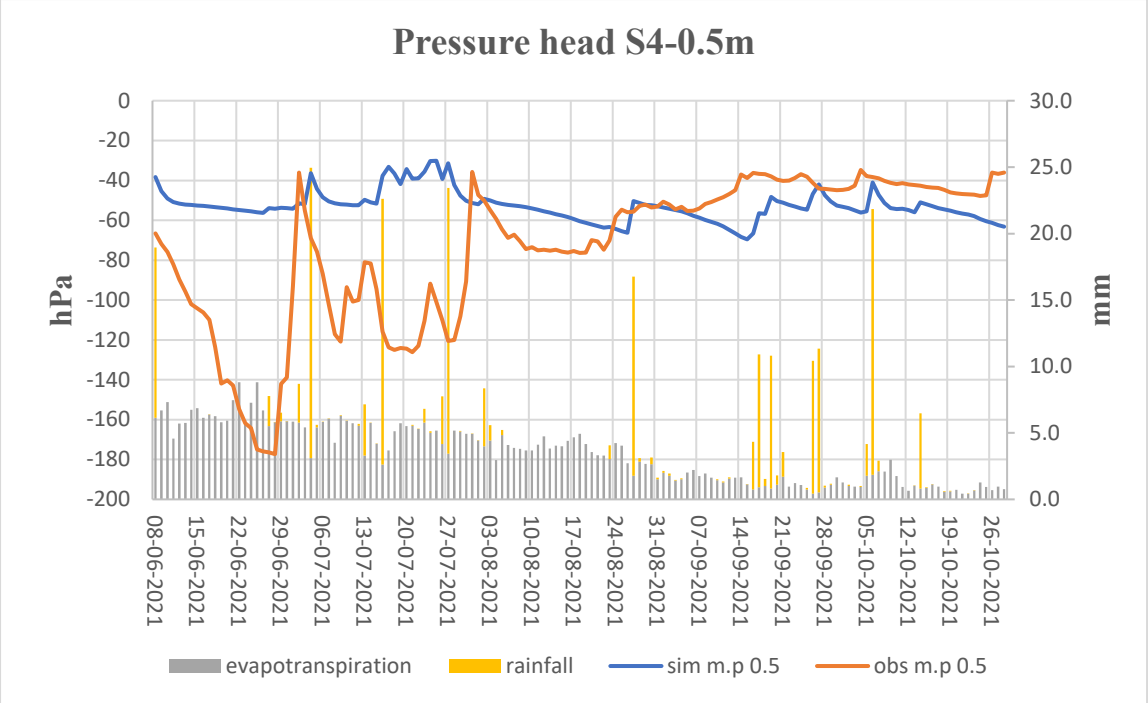

Figure 6.66: Simulated and measured pressure head *for station* S4 *at a depth of 0.5 m.*

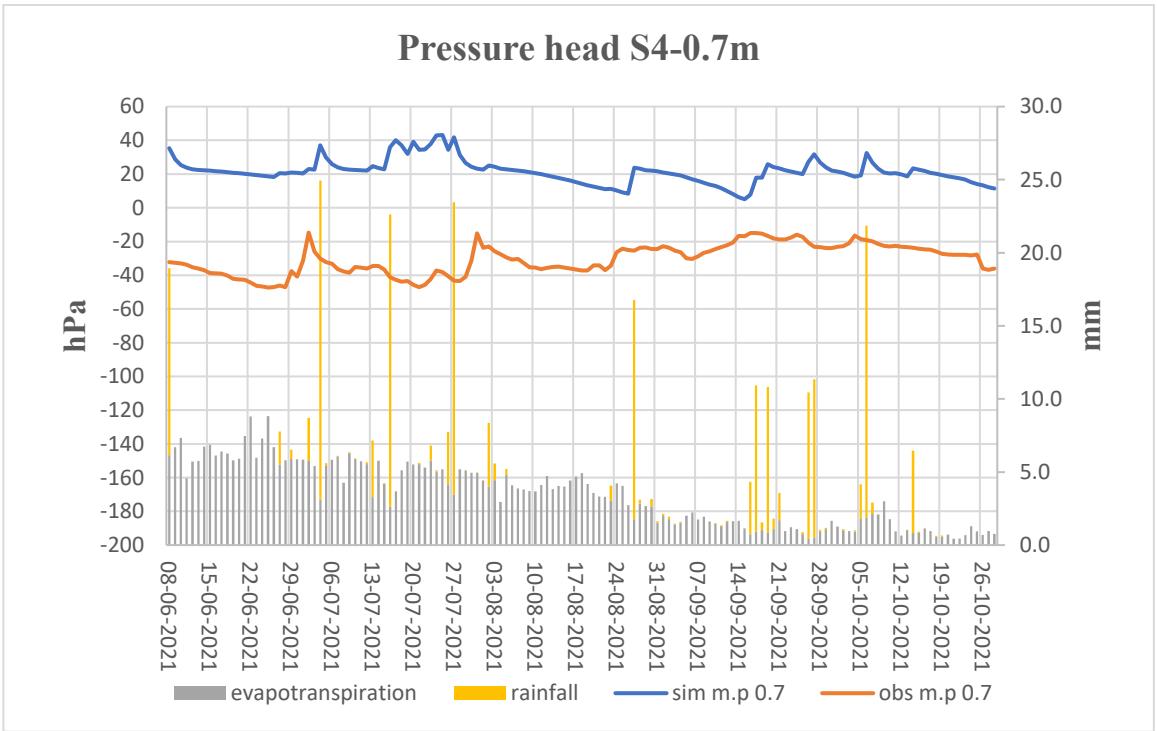

Figure 6.67: Simulated and measured pressure head *for station* S4 *at a depth of 0.7 m.*

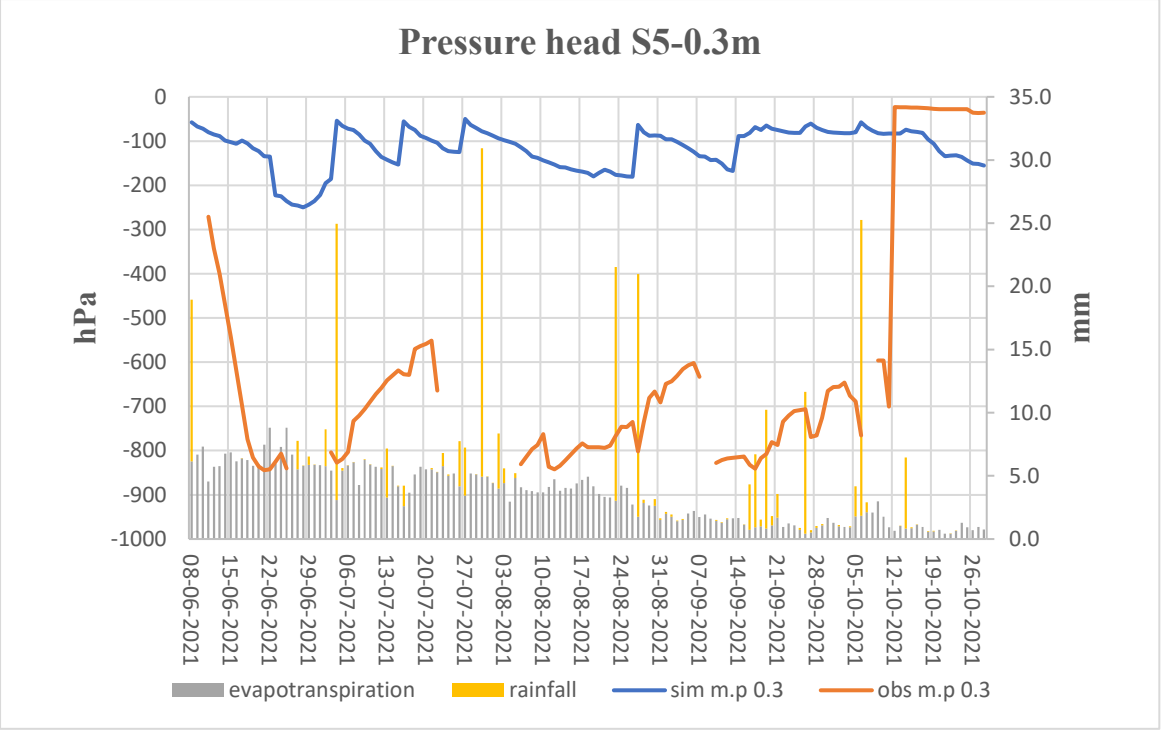

Figure 6.68: Simulated and measured pressure head *for station* S5 *at a depth of* 0.3 *m.*

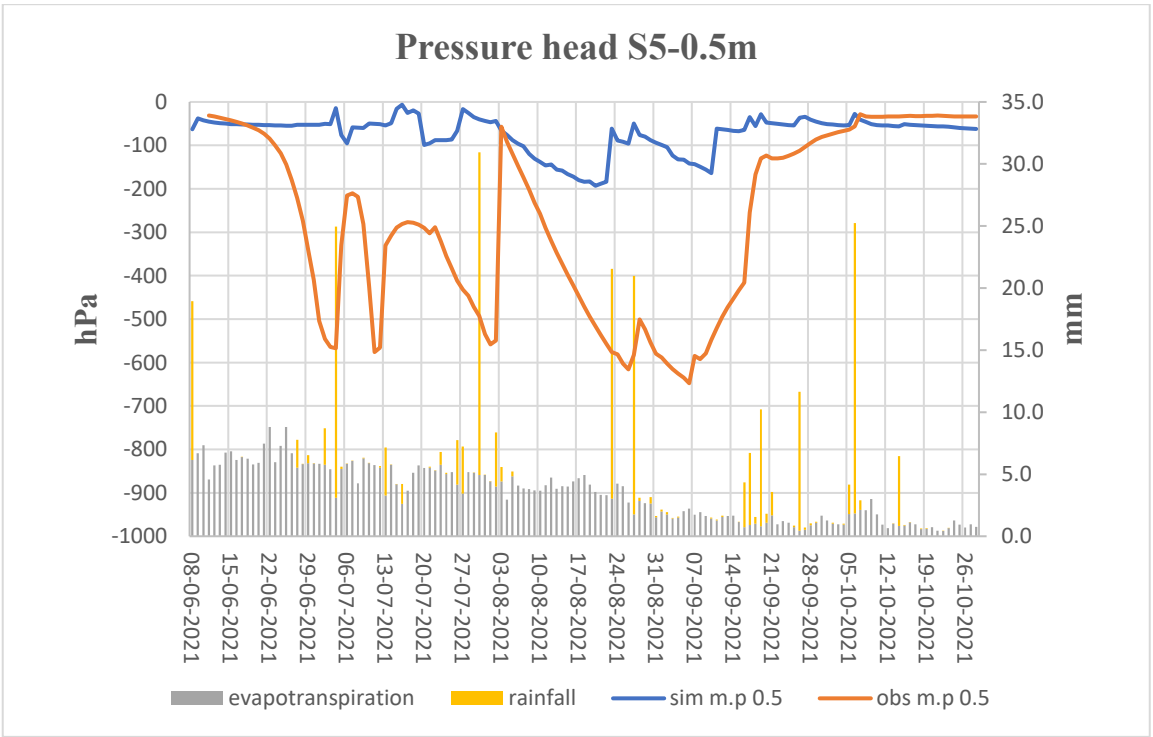

Figure 6.69: Simulated and measured pressure head *for station* S5 *at a depth of 0.5 m.*

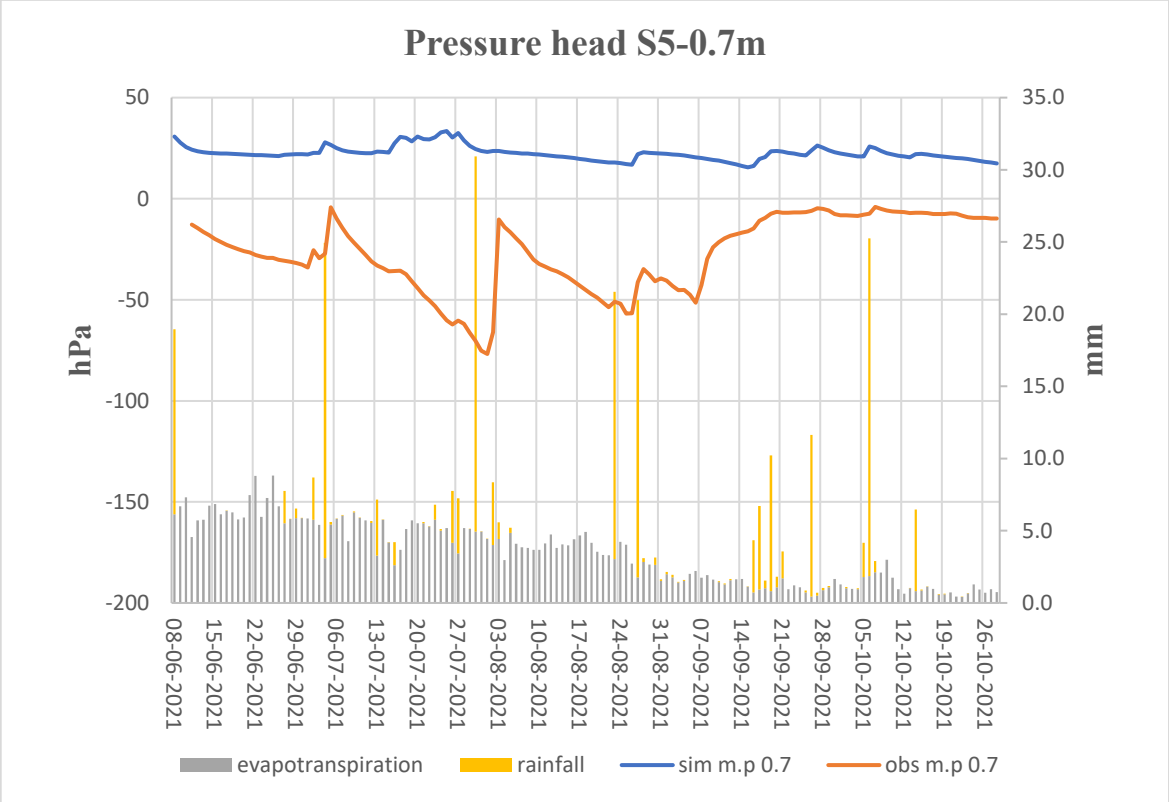

Figure 6.70: Simulated and measured pressure head *for station* S5 *at a depth of 0.7 m.*

7. CONCLUSION

The primary objective of this thesis was to explore the practical application of HYDRUS-3D to analyze moisture content and capillary pressure within the typical agricultural setting of Venice farmland, the experimental site, is located at the southern boundary of the Venice Lagoon. Through an extensive investigation, a magnitude of significant findings and valuable insights were obtained, providing a deeper understanding of the dynamics of soil moisture and its correlation with capillary pressure in this specific context. There are some agreement where the simulated values are able to trace the observation values in the case of analyzing moisture content for example (station S1 and S2 0.5 m deep, station S4 at a depth of 0.1m) where the simulated curve closely matches the trend and variability of the observed data points, but there are also some discrepancies because of noticeable inconsistencies in case of analyzing pressure head for example (Figure 6.59, 6.62 and 6.68)

The numerical simulations were performed using HYDRUS-3D software, which solve density-dependent flow and transport model by three-dimensional finite-elements. HYDRUS-3D possesses advanced capabilities such as storing a huge amount of data and allows animation of the simulated results facilitating the examination of spatial and temporal variations in moisture content and capillary pressure, effectively capturing the intricate dynamics of water movement in response to diverse hydrological and climatic conditions. The model's 3D mesh consists of large number of nodes and elements 18362 and 36720 respectively which was generated by using the operators provided in the software, which allows for an accurate representation of the site's topography, stratigraphy, and the boundary conditions.

Therefore, HYDRUS-3D has the potential in reproducing field-measured moisture content and pressure head information, utilizing soil parameters determined from textural data as the validation process verifies the model's performance with independent dataset, although site's distinct characteristics, such as soil heterogeneity, vegetation dynamics are vital when interpreting simulation results. Additionally, the software is particularly effective in sites where the soil heterogeneity is relatively moderate and can be adequately captured or preferably in the sites where the soil parameters obtained from textural information represent the soil properties accurately. As in the case for Ca'Bianca the soil data availability and

textural information were key factors for running the software effectively, sites with extreme soil heterogeneity are not suitable for the model to adequately simulate moisture content and pressure head data. The operating system was crashed multiple times while performing the simulation, this is the problem faced while using HYDRUS-3D although the system is pre-installed with modern graphic features.

8. BIBLIOGRAPHY

- [Rizzetto et al., 2., Teatini et al., 2., & Scudiero et al., 2. (2012). CHARACTERIZING THE SALTWATER EFFECT ON SOIL PRODUCTIVITY BYWORLDVIEW-2 IMAGES. THE SOUTHERN MARGIN OF THE VENICE LA. Retrieved from https://www.researchgate.net/publication/260597416_Characterizing_the_saltwater_effect_on_soil_productivity_by_WorldView-2_images_in_the_southern_margin_of_the_Venice_Lagoon_Italy
- [Teatini et al., 2. (2009). Monitoring the saltwater intrusion by time lapse electrical resistivity tomography: The Chioggia test site (Venice Lagoon, Italy). *ELSEVIER*. Retrieved from https://www.sciencedirect.com/science/article/abs/pii/S0926985109001062
- Cavallina et al., 2. (2022). Morpho-Sedimentary Constraints in the Groundwater Dynamics of Low-Lying Coastal Area.
- Cunico, I. (2019). *Development of numerical experiments to simulate lab tests and predict field activities in the Most project.*
- Elia Scudiero et al., T. P. (2014). Spatiotemporal Response of Maize Yield to Edaphic and Meteorological Conditions in a Saline Farmland. . *Agronomy Journal, Volume 1.6*. Retrieved from https://www.sciencedirect.com/science/article/abs/pii/S2352009414000285
- Mozzi et al., 2. (2003). *, M. Stratigraphy, palaeopedology and palynology of late Pleistocene and Holocene deposits in the landward sector of the Lagoon of Venice (Italy), in relation to the Caranto level. Ital. J. Quat. Sci. 2003, 16(1bis), 193–210.*
- Rizzetto et al., 2., Gambolati et al., 2., Carbogin et al., 2., & Tosi et al., 2. (n.d.). P. Soil contamination and land.
- Robert F. Carsel, R. S. (1988). Developing joint probability distributions of soil water retention characteristics. Retrieved from https://agupubs.onlinelibrary.wiley.com/doi/abs/10.1029/WR024i005p00755
- Schaap et al., J. S. (2001). *Rosetta*. Retrieved from www.hydrus3d.com
- Schaap, M. G. (2001). a computer program for estimating soil hydraulic parameters with hierarchical pedotransfer functions. ELSEVIER. Retrieved from https://www.sciencedirect.com/science/article/abs/pii/S0022169401004668
- Teatini et al., ,. E. (2022). Estimation of hydraulic parameters in a heterogeneous lowlying. *WILEY*, 17-20.
- Tosi et al., 2., & Fabbri et al., 2. (n.d.). Geomorphological setting and related hydrogeological implications of the coastal plain south of the Venice lagoon Hydrology of the Mediterranean and Semiarid Regions, E. Servat et al.

- Tossi et al. (2021). *Modelling the 2020-2021 freshwater recharge of a saline landfarm at Chioggia.* Retrieved from https://thesis.unipd.it/handle/20.500.12608/35545
- UNESCO, F. a. (n.d.). *Googlescholar*. Retrieved from Googlescholar: https://scholar.google.com/scholar?hl=en&q=+FAO%E2%80%90UNESCO.+%281989%29.+Soil+map+of+the+world%2C+revised+legend.+Food+and+Agriculture+Organization+of+the+United+Nations.
- vanGenuchten. (1980). In *A Closed-form Equation for Predicting the Hydraulic Conductivity of Unsaturated Soils1.*
- Zecchin et al., 2. (2009). Sequence stratigraphy of Holocene deposits in the offshore of Venice based on very high-resolution seismic profiles.